Electronic Theses and Dissertations, 2004-2019

2004

Inverse Boundary Element/genetic Algorithm Method For Reconstruction O

Mahmood Silieti
University of Central Florida

Showcase of Text, Archives, Research & Scholarship

INVERSE BOUNDARY ELEMENT/GENETIC ALGORITHM METHOD FOR RECONSTRUCTION OF MULTI-DIMENSIONAL HEAT FLUX DISTRIBUTIONS WITH FILM COOLING APPLICATIONS

by

MAHMOOD K. SILIETI

B.S. Jordan University of Science and Technology, 1999
M.S. Jordan University of Science and Technology, 2001

A dissertation submitted in partial fulfillment of the requirements
for the degree of Doctor of Philosophy
in the Department of Mechanical, Materials, and Aerospace Engineering
in the College of Engineering and Computer Science
at the University of Central Florida, Orlando, Florida

Fall Term
2004

Major Professor: Alain J. Kassab

ABSTRACT

A methodology is formulated for the solution of the inverse problem concerned with the reconstruction of multi-dimensional heat fluxes for film cooling applications. The motivation for this study is the characterization of complex thermal conditions in industrial applications such as those encountered in film cooled turbomachinery components. The heat conduction problem in the metal endwall/shroud is solved using the boundary element method (BEM), and the inverse problem is solved using a genetic algorithm (GA). Thermal conditions are overspecified at exposed surfaces amenable to measurement, while the temperature and surface heat flux distributions are unknown at the film cooling hole/slot walls. The latter are determined in an iterative process by developing two approaches. The first approach, developed for 2D applications, solves an inverse problem whose objective is to adjust the film cooling hole/slot wall temperatures and heat fluxes until the temperature and heat flux at the measurement surfaces are matched in an overall heat conduction solution. The second approach, developed for 2D and 3D applications, is to distribute a set of singularities (sinks) at the vicinity of the cooling slots/holes surface inside a fictitious extension of the physical domain or along cooling hole centerline with a given initial strength distribution. The inverse problem iteratively alters the strength distribution of the singularities (sinks) until the measuring surfaces heat fluxes are matched. The heat flux distributions are determined in a post-processing stage after the inverse problem is solved. The second approach provides a tremendous advantage in solving the inverse problem, particularly in 3D applications, and it is recommended as the method of choice for this class of problems. It can be noted that the GA reconstructed heat flux distributions are robust, yielding accurate results to both exact and error-laden inputs. In all cases in this study, results from experiments are simulated using a full conjugate heat transfer (CHT) finite volume models which incorporate the interactions of the external convection in the hot turbulent gas, internal convection within the cooling plena, and the heat conduction in the metal endwall/shroud region.

Extensive numerical investigations are undertaken to demonstrate the significant importance of conjugate heat transfer in film cooling applications and to identify the implications of various turbulence models in the prediction of accurate and more realistic surface temperatures and heat fluxes in the CHT simulations. These, in turn, are used to provide numerical inputs to the inverse problem. Single and multiple cooling slots, cylindrical cooling holes, and fan-shaped cooling holes are considered in this study. The turbulence closure is modeled using several two-equation approach, the $v^2 - f$ four-equation turbulence model, as well as five and seven moment Reynolds Stress Models. The predicted results, by the different turbulence models, for the cases of adiabatic and conjugate models, are compared to experimental data reported in the open literature. Results show the significant effects of conjugate heat transfer on the temperature field in the film cooling hole region, and the additional heating up of the cooling jet itself. Moreover, results from the detailed numerical studies presented in this study validate the inverse problem approaches and reveal good agreement between the BEM/GA reconstructed heat fluxes and the CHT simulated heat fluxes along the inaccessible cooling slot/hole walls.

ACKNOWLEDGEMENTS

First, all praise is due to Almighty *ALLAH* for keeping me in a good health and condition, and for attending upon the successful completion of this work. I am indebted to his supremacy and his blessings in every single step of my life.

I would like to thank Dr. Alain Kassab, my advisor, for providing support and recommendations through out this research and for his never-ending patience and care in advising me. My sincere gratitude goes to his continuous guidance throughout my graduate studies, by spurring my interests in various aspects of computational heat transfer. I appreciate his efforts in involving me in the Siemens Westinghouse Power Corporation (SWPC) funded projects: the Shroud Film Cooling (SFC) and the Evaluation of Grid Generation Packages.

I would like to thank Dr. Eduardo Divo, my co-advisor, whose wisdom and strength always touched me in a profound way, not only in academic pursuits, but in life as general. My special greetings are extended to him for his great input and insight into my research. It has been a pleasure to have had Dr. Jay Kapat, Dr. David Nicholson and Dr. S. Roy Choudhury on my supervisory committee. Steven Dick, the computer research specialist, is also recognized for providing me with the technical support.

My invaluable appreciation is owed to SWPC for funding my Ph.D. studies at the University of Central Florida as a Siemens Westinghouse Fellow. Also, I would like to extend my gratitude to all the people who I worked with throughout this journey of doctoral program, especially Edward North, Sanjay Chopra and Robert K. Scott.

Last, but definitely not least, I would like to express my deep love to my mother, my family, my friends and well-wishers for standing next to me.

TABLE OF CONTENTS

LIST OF FIGURES

LIST OF TABLES

LIST OF ABBREVIATIONS/NOMENCLATURE

BEM   Boundary Element Method

BIE   Boundary Integral Equation

CCT   Conjugate Calculation Technique

CFD   Computational Fluid Dynamics

CHT   Conjugate Heat Transfer

Conj.   Conjugate

Cp specific heat at constant pressure

D film-cooling hole diameter

FDM   Finite Diference Method

FEM   Finite Element Method

FVM   Finite Volume Method

g gravity acceleration

GA   Genetic Algorithm

GMRES   Generalized Minimal Residual method

h convective heat transfer coefficient

I   momentum ratio, $I=(\rho V)_c^2/(\rho V)_{main}^2$

k turbulent kinetic energy

k   thermal conductivity coefficient

L film-cooling hole length

M blowing ratio, $M = (\rho V)_c/(\rho V)_{main}$

N number of boundary nodes

N_m number of measuring points

N_w number of measuring points at cooling-slot surfaces

NS number of singularities (sinks)

P	pressure
Pr	Prandtl number
q_j	nodal heat fluxes
$q(x,y)$	heat flux
Q_K	strength of the Kth singularity (sink)
$\widehat{q}(x,y)$	measured heat flux
R	specific gas constant
RBF	Radial Basis Functions
Re	Reynolds number
Re_c	Reynolds number defined as, $Re_c = \rho_c V_c D / \mu_c$
RKE	Realizable k-ϵ turbulence model
RNG	ReNormalization Group k-ϵ turbulence model
RSM	Reynolds Stress Model
s	opening of the cooling slot
S	source term of turbulent quantities
SIMPLE	Semi-Implicit Pressure Linked Equations
SKE	Standard k-ϵ turbulence model
SKW	Standard k-ω turbulence model
SST	Shear Stress Transport k-ω turbulence model
T	temperature magnitude
T_j	nodal temperature
$T(x,y)$	temperature magnitude
$\widehat{T}(x,y)$	measured temperature
V	velocity magnitude
V2F	$v^2 - f$ turbulence model
x	streamwise distance measured from film-hole centerline

y	vertical distance measured from top of the film-hole
z	spanwise distance measured from film-hole centerline
x'	distance downstream from slot leading edge
x''	a dimensionless ratio defined as $x'' = \frac{x'}{Ms} Re_c^{-0.25}$
u_i', u_j'	velocity fluctuations
u_τ	friction velocity
y^+	law of the wall coordinate defined as $y^+ = \frac{\rho\, u_\tau\, y}{\mu}$
α	injection/inclination angle
β	regularization parameter
δ	Dirac delta function
ϵ	turbulent dissipation rate
γ	specific heat ratio
η or Eta	film cooling effectiveness
μ, μ_t	molecular and turbulent viscosity
ν	kinematic viscosity
ρ	density
τ_{ij}	stress tensor
σ	Prandtl-Schmidt number
ω	specific dissipation rate
ζ	local coordinate along cooling slot edge
Γ	boundary
Ω	domain
∇	gradient operator

Subscripts

AW/a	adiabatic

c	coolant
$Conj$	conjugate
i	represents the direction in tensor form
m	mainflow
n	outward normal
o	stagnation
r	recovery
t	turbulent
∞	free stream
$*$	reference

CHAPTER 1

INTRODUCTION

Given the large number of sustained operational hours required for industrial turbines, two important demands placed on such engines are component life and overall engine performance. These demands are somewhat conflicting because high temperatures are required at turbine inlet in order to achieve high performance; however, increasing turbine inlet temperature in turn causes reduced component life and high repair costs and downtime costs. One way to overcome this problem is to employ film cooling. Film cooling is the introduction of a secondary fluid (coolant or injected fluid) at one or more discrete locations along a surface exposed to a high temperature environment to protect that surface not only in the immediate region of injection but also in the downstream region [1]. This technique is widely used in protecting critical components exposed to high temperatures; for instance, combustor walls, vanes, blades, and endwalls or shrouds. It is usually accomplished by introducing film cooling holes (shaped or non-shaped) or slots to provide a designed insulating blanket of cooler air bled from the compressor, which comprises the secondary airflow in the gas turbine.

It is important to characterize the efficacy of such a cooling scheme, particularly as the compressor air employed to protect critical parts of the turbine is very expensive from an overall engine performance perspective, as much work has been expended in the compressor to achieve the pressures at which the secondary airflow is bled. The film effectiveness is a common way to report the adiabatic wall temperature that is the driving temperature for the convection at the exposed metal surfaces and to simultaneously provide a measure of the efficacy of film cooling scheme. The film effectiveness is closely related to the velocity and temperature profiles as well as velocity and thermal boundary layer thickness. The film effectiveness can be measured in carefully designed experiments. However, in determining the film coefficient distributions at the

exposed surfaces, the thermal conditions within the cooling holes/slots are unknown. As there are no correlations or experimental data available to characterize heat transfer in such cases, there exists a need to determine the film coefficient distributions in film cooling holes/slots.

For gas turbine applications, as in many other heat transfer applications, it is necessary to accompany the computation of the flow and associated heat transfer in the fluid with the heat conduction inside the adjacent solid surfaces. Such as the case for the film cooling problem under consideration in this study. The coupling of these two modes of heat transfer is termed as conjugate heat transfer (CHT). For a typical cooled turbine airfoil/shroud at operating conditions, there are three heat transfer problems linked together: external convection, internal convection, and conduction within the metal. The metal temperature distribution, and temperature gradients, which determine the component life. However, due to the complex, coupled nature of the heat transfer problem, accurate predictions of the metal temperature are difficult from a design standpoint.

Generally, the approaches to calculate the conjugate heat transfer, or the metal temperature, can be divided up into two methods: the hybrid coupling procedure method and the homogeneous method. The hybrid method is performed using CFD solvers coupled to a conventional FEM or BEM solver to predict the temperature distribution at the metal walls. The main disadvantages of this method are problems associated with handling boundaries between different calculation areas when using FEM for the conduction solution. However, no such disadvantage exists when using BEM for the conduction solution as only a surface mesh is required for the conduction solution. The homogeneous conjugate heat transfer modeling method consists of direct coupling of the fluid zone and the solid zone using the same discretization and numerical approach. This makes it possible to have an interpolation-free crossing of the heat fluxes between the neighboring cell faces; also, the wall surface temperature, as well as the temperatures in the airfoil/shroud walls are a direct result of this simulation.

The retrieval of surface heat fluxes or convective heat transfer coefficients is often accomplished using surface temperature histories provided by thermographic techniques applied in controlled experiments and in conjunction with theoretical assumptions. It is herein proposed to use the boundary element method (BEM) to resolve 2D and 3D heat transfer and determine heat flux distributions, and consequently the heat transfer coefficient distribution, by a novel inverse problem method. The BEM is ideally suited to solve this inverse problem as surface temperatures and heat fluxes appear as nodal unknowns. These are precisely the variables required in inverse analysis. The BEM is an integral equation numerical technique which offers many advantages over FDM, FVM, or FEM. One of the most striking features of the BEM is that, for many engineering problems, the boundary integral equation discretized to solve the field problem of interest involves only boundary surface(s) of the domain, thereby reducing the dimension of the problem by one. Thus, the BEM lends itself ideally not only to analysis field problems, but also lends itself to modeling coupled field problems such as those arising in conjugate heat transfer (CHT) modeling.

It is the purpose of this dissertation to develop an inverse problem methodology to reconstruct the multi-dimensional heat flux distributions or heat transfer coefficient distributions and to apply this technique to film cooling holes/slots configurations encountered in turbomachinery applications. In the course of this study, the importance and relevance of conjugate heat transfer to film-cooling will be established. An inverse problem will be formulated and a novel solution methodology will be developed based on boundary element method (BEM) and a genetic algorithm (GA). The heat conduction problem in the metal endwall or shroud is solved using the BEM, and the inverse problem is solved using a GA. Thermal conditions are overspecified at exposed surfaces amenable to measurement, while the temperature and surface heat flux are unknown at the film cooling hole/slot walls. The unknown temperature and surface heat flux distributions at surfaces that are not amenable to measurements are determined in an iterative process following two approaches. The first approach, developed

for 2D applications, solves an inverse problem whose objective is to adjust the film cooling hole/slot wall temperatures and heat fluxes until the temperature and heat flux at the measurement surfaces are matched in an overall heat conduction solution. The second approach, developed for 2D and 3D applications, is to distribute a set of singularities (sinks) at the vicinity of the cooling slots/holes surface inside a fictitious extension of the physical domain or along cooling hole centerline with a given initial strength distribution. The inverse problem iteratively alters the strength distribution of the singularities until the heat fluxes at the measurement surfaces are matched. The heat flux or heat transfer coefficient distributions are then determined in a post-processing stage after the inverse problem is solved. This approach offers significant advantages in model reduction especially in 3D applications.

In all cases, results from experiments are simulated using a full conjugate heat transfer (CHT) finite volume models which incorporate the interactions of the external convection in the hot turbulent gas, internal convection within the cooling plena, and the heat conduction in the metal endwall/shroud region. Extensive numerical investigations are undertaken to demonstrate the importance of conjugate heat transfer in film cooling applications and to identify the implications of various turbulence models in prediction of accurate surface temperature and heat flux distributions. These, in turn, are used as numerical inputs to the inverse problem approach developed in this study.

Attention is now given to the review of the literature. Subsequently, details of careful finite volume modeling of conjugate heat transfer in slots, rounded and fan-shaped cooling holes are presented. The physics of film cooling and the importance of conjugate heat transfer are discussed. The results of the CHT models will be used to provide simulated numerical inputs to the BEM/GA inverse problem methodology developed in subsequent chapters. Several numerical examples will be presented to validate the inverse approach to reconstruction of multi-dimensional heat flux and heat transfer coefficient distributions. Finally, results obtained from

this study are presented in form of correlations as a guide to the application of the inverse methodology to experiment.

The main contributions of this dissertation include the following:

- Developing an inverse problem methodology based on boundary element method (BEM) and a genetic algorithm (GA) to reconstruct the heat flux distributions with application to film cooling holes/slots.

- Introducing a new and a unique technique to solve the 2D and the 3D inverse problem, i.e. a hybrid singularity superposition/boundary element-based inverse problem method. The main advantage of this technique is to eliminate the need of meshing the cooling holes/slots. Also, the use of singularity (sinks) distributions significantly reduces the number of parameters sought in the inverse problem. Moreover, the distribution of the heat flux at the walls of the cooling hole is determined in a post-processing stage after the inverse problem is solved, which constitutes a tremendous advantage in solving the inverse problem, particularly for the applications of film cooling holes/slots.

- Developing an in-house 2D and 3D codes to solve the inverse problem through the course of this study. Those codes are written in Fortran.

- Developing a finite volume models (FVM) to simulate the experimental data and to show the significant effects of conjugate heat transfer (CHT) for film cooling applications.

- Investigating the performance of the two-equation models in addition to the $v^2 - f$ four -equation turbulence model in predicting the surface temperature and the film cooling effectiveness. The simulated results confirmed that the predictions of the realizable k-ϵ model gave the best agreement in comparison to the available experimental data.

- Introducing a new correlations for the local and average convective heat transfer coefficients along the edges/walls of cooling slots/holes reflecting dependency on position, the Prandtl and Reynolds numbers, blowing ratios, as well as coolant-to -mainflow temperature ratio.

5

CHAPTER 2

LITERATURE REVIEW

The pertinent literature on the various subjects touched upon in this study is now presented. Thus the subjects of film cooling, conjugate heat transfer, and inverse problems will be addressed each in turn.

In the past three decades there have been numerous studies on the film cooling of gas turbine components such as airfoils and endwalls. These studies can be divided into two major sections- experimental studies and computational studies. Also, each section can be divided into film cooling from 2D slots or film cooling from shaped or non-shaped holes.

There have been a few studies that have measured endwall heat transfer as a result of injection from a 2D flush slot just upstream of the vane. Hartnett et al. [2] presented a detailed study of heat transfer for air injection through a single slot into a turbulent boundary layer on a flat plate. They showed that the heat transfer coefficients on a film cooled wall agree within 10 percent with those on a solid wall for the same main stream conditions for values of the parameter x'/s larger than 30, where x' is distance downstream from slot leading edge, and s is the slot width. In the case of multiple slots, Chin et al. [3] presented an experimental results for film cooling of an adiabatic plate of one to ten slots. In this study, the adiabatic wall temperatures downstream of the last equivalent slot were measured and correlated in terms of the flow parameters, equivalent slot number and slot spacing, and distances downstream of the last equivalent slot. Blair [4] measured adiabatic effectiveness levels and heat transfer coefficients for a range of blowing ratios through a flush slot placed just upstream of the leading edges of his single passage channel. One of the key findings was that the endwall adiabatic effectiveness distributions showed extreme variations across the vane gap. Much of the coolant was swept across the endwall toward the suction side corner resulting in reduced coolant near the pressure

6

side. As the blowing ratio was increased, Blair found that the extent of the coolant coverage also increased. Measured heat transfer coefficients were similar between no slot and slot injection cases.

Roy et al. [5] compared their experimental measurements and computational predictions for a flush cooling slot that extended over only a portion of the pitch directly in front of the vane stagnation. The adiabatic effectiveness measurements indicated that the coolant migrated toward the pressure side of the vane, and reduced values of local heat transfer coefficients at the leading edge when slot cooling was present to no slot cooling. Heat transfer measurements have shown that at the endwall, next to the leading edge, the heat transfer is increased by the horseshoe vortex (Boyle and Russell [6], and York et al. [7]). One study has combined an upstream slot with film cooling holes in the downstream endwall vane passage was those of Kost and Nicklas [8] and Nicklas [9]. One of the most interesting results from this study was that they found for the slot flow alone, which was 1.3% of the passage mass flow, the horseshoe vortex became more intense. This increase in intensity resulted in the slot coolant being moved off of the endwall surface and heat transfer coefficients that were over three times that measured for no slot flow injection. They attributed the strengthening of the horseshoe vortex to the fact that for the no slot injection the boundary layer was already separated with fluid being turned away from the endwall at the injection location. Given that the slot had a normal component of velocity, injection at this location promoted the separation and enhance the vortex. Their adiabatic effectiveness measurements indicated higher values near the suction side of the vane due to the slot coolant migration. Knost et al. [10] focused on the interaction between the coolant leaving a two-dimensional slot at the combustor-turbine interface and the endwall film cooling injection. The results of there study showed that the jet trajectory is highly dependent on the local blowing ratio for the cooling holes. One of the most significant findings was a lack of the endwall film cooling along the region where two turbine vanes are mated.

O'Malley et al. [11] produced experimental data for a 90° slot for different blowing ratios. A theoretical model was proposed by Fitt et al. [12] for a normal slot geometry trying to quantify the effect on the flow within the slot due to main/secondary flow interaction. The model assumed no separation at the slot trailing edge, and viscous effects were neglected. One important aspect of this theory is the lid effect: separation from the front of the slot is tangential to the wall, and the main stream acts as a lid over the slot forcing all the injected fluid to emerge from a region close to the rear vertex. Thus the mass flow of the injectant is reduced, weakening the cooling effect as well. Sarkar et al. [13] did a comparison of different turbulence models for the prediction of the flow and temperature fields. Surprisingly, they found that the low Reynolds-number versions of the $k - \epsilon$ model performs better than the $k - \omega$ model in capturing the surface temperature distribution and, hence, the adiabatic film cooling effectiveness. Teekaram et al [14] investigated the case for the subsonic injection from a 30° slot into a flow that accelerated to supersonic conditions.

Kassimatis et al. [15] studied the effect of boundary conditions at the slot exit for a normal slot. They figured out that the pressure boundary condition is in agreement with the experimental data, whereas the velocity boundary condition produced less accurate results, and the length of the recirculation bubble seems to be linearly correlated to the blowing ratio. Jia et al. [16] carried out a numerical and experimental study for a slot film cooling with various blowing ratios and angles (16°, 30°, 40°, 60°, and 90°) using $v^2 - f$ turbulence model. The results show that a recirculation bubble downstream the jet exists for jet angles larger than 40°, but it vanishes when the angle is less than 30°. They found that a blowing ratio around one and a blowing angle of 30° provided the highest film cooling effectiveness.

With regards to 3D film cooling holes, Goldstein et al. [17-22] and Pedersen et al. [23] measured the film cooling effectiveness with injection of air through either a single hole or a row of holes, with an injection angle of 35° or 90°. The data from single hole tests were similar to that for a row of holes at low blowing ratios but significant differences were observed at higher

blowing rates. Also, they found that the introduction of discrete holes in replacement of slots causes less uniform cooling and increased mixing with the mainstream flow, resulting in reduced levels of adiabatic effectiveness and increased aerodynamic loss due to film cooling. Bergeles et al. [24] investigated a single discrete jet injected at a 30° streamwise injection angle. Andreopoulos and Rodi [25] documented an extensive study of an isolated normal jet-in-crossflow, showing the counter-rotating vortex structure within the jet as the jet interacted with the crossflow. Pietrzyk et al. [26-28] and Sinha et al. [29] made significant advances in the experimental modeling of film cooling flow fields. They studied the hydrodynamic and thermal characteristics of a row of discrete jets inclined at 35° to the cross flow with a short film cooling hole length-to-diameter (L/D) ratio. Detailed mean flow and turbulence quantities were presented throughout the flow field, as well as measurements of adiabatic film effectiveness. Jubran [30] reported a correlation and prediction of film cooling effectiveness and the velocity field from two rows of holes inclined in the streamwise and spanwise directions.

Recent studies have shown that expanding the exit of the cooling hole improves film cooling performance relative to cylindrical hole. Overall improvements in adiabatic effectiveness were found for laterally expanded holes (Goldstein et al. [22]) as well as for forward expended holes (Makki and Jakubowski [31]). Wittig et al. [32], Thole et al. [33] and Gritsch et al. [34] provided measurements for the flowfield and the film cooling effectiveness downstream of a cylindrical, a laterally expanded, and a laterally forward expanded film cooling hole. The flow conditions were the crossflow Mach number at the hole entrance side (up to 0.6), the crossflow Mach number at the hole exit side (up to 1.2), and the blowing ratio (up to 2). The coolant-to-mainflow temperature ratio was kept constant at 0.54. Bell et al. [35] and Yu et al. [36] measured the adiabatic film cooling effectiveness for cylindrical and shaped holes. Yuen and Martinez-Botas [37] studied experimentally the film cooling effectiveness on a cylindrical hole with a streamwise angle of 30°, 60° and 90°. The hole-length $(L/D = 4)$ and the blowing ratio ranges from 0.33 to 2.

Friedrichs et al. conducted a detailed endwall film cooling [38-40], the results of their first study [38], which were all surface measurements or visualization, indicated a strong influence of the secondary flows. Quite counter-intuitive to most, their data showed that the angle at which the coolant leaves the hole did not dictate the coolant trajectory except near the hole exit. Furthermore, the endwall cross-flow was altered so that the cross-flow was turned toward the invicid stream lines, which was due to the film cooling injection. A study by Farmer et al. [41] showed the film cooling performance improved by shaping the cooling holes. Sargison et al. [42] investigated a new film cooling hole, a converging slot-hole, on the prediction of film cooling performance. It turns out that this film cooling hole improves both the heat transfer and aerodynamic performance of turbine vane and rotor blade cooling systems. Detailed numerical analysis of the film cooling physics in the case of a flat plate with one row of cooling holes have been presented by Walters and Leylek [43] for cylindrical holes and by Hyams and Leylek [44] for shaped holes. Other numerical studies on the leading edge film cooling physics by York and Leylek [45,46] focused on the determination of the adiabatic film cooling effectiveness and heat transfer coefficients.

Concerning the CFD research on this subject, a bibliography (1971-1996) of the most important publications can be found in a study by Kercher [47]. Most of the published work on predictions of film cooling is based on either a parabolic or semielliptic procedure. Bergeles et al. [48] used the semi-elliptic treatment to simulate film cooling from a row of holes. As the calculation procedure based on the semi-elliptic method cannot efficiently handle regions with a reverse flow, their prediction was restricted to injection at very low blowing ratios. Demoran [49] performed a series of simulations for a row of discrete jets issuing normally into a cross flow, concentrating on the effects of grid refinement and discretization scheme on the overall solution. Detailed computational studies on film cooling from a row of holes have been presented by Demuren et al. [50]. They used the locally elliptic procedure, which allows the fully elliptic treatment to a small region containing a reverse flow; however, in the far field the model

reverts to the parabolic scheme. Amer et al. [51] predicted the film cooling effectiveness from two rows of inclined holes incorporating different turbulence models such as the standard and modified k-ω models and the k-ϵ model, together with its nonisotropic version in the PHOENICS package. Leylek and Zerkle [52] performed a jet-in-crossflow simulation using a geometry typical of that found in film cooling applications. The computational domain included the crossflow, the film hole, and the supply plenum. Walters and Leylek [53,54], McGovern and Laylek [55], Hyams and Laylek [56], as well as Brittingham and Leylek [57] applied a systematic computational methodology to a 3D jet-in-crossflow with unstructured grid for both cylindrical and shaped cooling holes at streamwise and compound injection angles. In the above studies, turbulence closure was obtained using standard k-ϵ model. Heidmann and Hunter [58] performed detailed calculations for a flat plate with a row of 35° round holes for various blowing and density ratios using k-ω turbulence model. More studies considered the effect of shaping the cooling hole on film cooling performance with both streamwise and compound injection angles; for more details see [59-65].

Considering the conjugate heat transfer (CHT) modeling, there have been several studies based on both the hybrid coupling procedure method and the homogeneous method. Kelkar et al. [66] carried out conjugate heat transfer computations in boundary-fitted coordinates by using an effective conductance to define the interface conductivity between the solid and the fluid regions. The cooling of turbine blades was also the subject of the work of Heselhaus and Vogel [67]. They presented a coupled scheme between finite volume-based Navier-Stokes solver and a finite element-based program for heat conduction and used it to compute the flow over a turbine stator blade with internal cooling. The numerical procedure was based on an iterative procedure, whereby at each step heat fluxes arising from the computation of the flow and convective heat transfer were used as boundary conditions for the computation of heat conduction inside the blade walls. Papanicolaou et al. [68] developed a numerical procedure for simulation of conjugate heat transfer in generalized coordinates and used in effusion-cooled combustor liner.

Discretized equations for nodes located exactly on the solid-fluid interface were derived using energy conservation principles, yielding the corresponding temperatures directly, without the need for inter- or extrapolation from adjacent nodes. They used a finite volume-based computer code along with the SIMPLE algorithm and $k - \epsilon$ turbulence model.

A conjugate calculation technique (CCT) has been presented by Bohn et al. [69-71]. Li and Kassab [72,73], Heidmann et al. [74], and Kassab et al. [75] pursued a different method of coupling the fluid and solid thermal problems with applications to trubomachinery and flow within channels. The basis of their technique is the coupling of the boundary blement method (BEM) for the solution of solid conduction problem and the finite volume method for the fluid flow region. Since the thermal conduction in a solid is governed by Laplace equation for temperature in the linear case and the Laplace equation for the Kirchhoff temperature in the non-linear case, it may be solved using only boundary discretization. BEM takes advantage of this fact and does not require meshing of the solid volume. This method has been successfully applied to intricate 3D film cooled blades [74-75], with a parallel iterative domain decomposition technique particularly tailored to solving the associated large-scale conjugate problem. In another study carried out by York et al. [76], a finite volume-based code (Fluent version 5) was used to predict the metal temperature of a 3D internally cooled gas turbine vane. In this code, the solid and fluid zones are coupled by energy conservation at the interfaces.

Bohn et al. [77] carried out a conjugate heat transfer analysis for different configurations of film cooling holes. The numerical scheme for the simulation of the fluid flow and heat transfer works on the basis of an implicit finite volume method with a multi-block technique, and the Fourier equation is solved in the solid body blocks. Coupling of fluid blocks and solid body blocks is achieved via a common wall temperature resulting from the equality of the local heat fluxes passing through the contacting cell faces. This method of calculating the heat fluxes requires a very high grid resolution at the contacting block faces. They showed that the application of the conjugate calculation method comprises the influence of heat transfer on the

velocity field within the cooling film. In particular, the secondary flow velocities are affected by local heat transfer, which varies significantly depending on the local position. Rigby and Lepicovsky [78] presented experimental and numerical heat transfer coefficients, as well as solid temperature contours/profiles, as a result of several conjugate simulations/measurements of the flow over an internally cooled flat plate. Reasonable agreement between numerical calculations and both experimental data and correlations was observed. Discrepancies were mainly attributed to the adopted turbulence (k-ω, Low Reynolds form (LR)) model inability to predict the location of external flow boundary layer transition.

Recently, Silieti et al. [79-81] investigated the numerical prediction of film cooling effectiveness in 2D and 3D gas turbine endwalls/shrouds for the cases of conjugate and adiabatic heat transfer models. They considered different cooling hole geometries; i.e. cooling slots, cylindrical and fan-shaped cooling holes at different blowing ratios. They incorporated the effects of different turbulence models in predicting the surface temperature and hence the film effectiveness. The turbulence closure was investigated using seven different turbulence models: the standard k-ϵ model, the RNG k-ϵ model, the realizable k-ϵ model, the standard k-ω model, the SST k-ω model, the $v^2 - f$ turbulence model, in addition to the Reynolds Stress Model. The simulations were processed using the finite volume-based code; i.e. Fluent version 6.1.22 software from Fluent, Inc. The discretization was a second-order with double precision accuracy. In the fluid zones, the steady times-averaged Navier-Stokes equations were solved, and pressure-velocity coupling was achieved with a pressure correction algorithm. In the solid zone, only the Fourier equation for heat diffusion was solved. At the fluid-solid interfaces, an energy balance was satisfied at each iteration such that the heat flux at the wall on the fluid side was equal in magnitude and opposite in sign to the heat flux on the solid side. The temperature of the boundary itself was adjusted during each iteration to meet this condition. They found that k-ϵ models, especially realizable k-ϵ model, performed better than the k-ω models in predicting the surface temperature distribution and hence the film cooling effectiveness. The results confirm

that the conjugate heat transfer model shows a significant difference in the temperature predictions in comparison with the adiabatic models. Also, results show the effect of the conjugate heat transfer on the temperature field in the film cooling hole region, and the additional heating up of the cooling jet itself.

Theoretical concerns regarding inverse problems can be found in Thikonov and Arsenin [82]. Reviews of certain inverse heat transfer problems can be found in Beck et al. [83], Kurpisz and Nowak [84], and in Alifanov [85]. Bui [86] provides an introduction to inverse problems in mechanics of materials. Applications of inverse problems in engineering analysis include acoustics, solid mechanics, heat transfer, among others. Inverse problems have been instrumental in solving many important engineering heat transfer problems. For example, inverse problems have been formulated to resolve unknown thermophysical properties such as thermal conductivities [87,88] and convective heat transfer coefficients and heat flux reconstruction [89-91]. Inverse problems have also been formulated to determine the unknown source term in the heat conduction equation [92,93]. There is a large body of literature devoted to inverse problems formulated for the recovery of unknown boundary conditions. Comprehensive reviews of such work can be found in Meric and Kul [94]. Inverse problems also find applications in design and shape optimization of thermal systems. The latter application is closely related to the inverse geometric problem by Kassab et al. [97-100] which is solved in the non-destructive approach to the detection of subsurface flaws and cavities Kassab et al. [101-104].

Surface heat fluxes have been retrieved using BEM-based inverse algorithms and internal temperature measurements as in Kurpisz and Nowak [84]. In a numerical study, Maillet et al. [105] formulated an inverse BEM-based approach to retrieve angular distributions of convective heat transfer coefficients from a cylinder using second order regularization to stabilize results. Hsieh and Farid [106] used an inverse BEM approach to retrieve angular variation of convective heat transfer coefficients over a rough heated horizontal cylinder in an experiment where steady state surface temperatures are measured non-intrusively by infrared scanning. Martin and

Dulikravich [107] used a steady state BEM-based approach in a numerical study to retrieve convective heat transfer coefficients and Singular Value Decomposition to stabilize results. Kassab et al. [108] and Divo et al. [109] developed a BEM-based inverse algorithm to retrieve multi-dimensional varying convective heat transfer coefficients from transient surface temperature measurements. At each time level, a regularized functional is minimized to retrieve current heat fluxes and simultaneously smooth out the effect of measurement errors. Kassab et al. [110] and Bialecki et al. [111,112] developed an inverse algorithm to reconstruct multi-dimensional surface heat flux, and minimized the functional using the Levenberg-Marquardt method and a genetic algorithm (GA). They showed that GA can be used successfully to retrieve surface heat flux distributions. Silieti et al. [113,114] developed an inverse methodology as a means of determining heat transfer coefficient distributions in film cooling holes/slots. Thermal conditions were overspecified at exposed surfaces amenable to measurement, while the temperature and surface heat flux distributions are unknown at the film cooling hole/slot walls. The unknown temperature and surface heat flux distributions are determined in an iterative manner by solving an inverse problem whose objective is to adjust the film-cooling hole/slot wall temperatures and heat fluxes distributions until the temperature and heat fluxes at the measurement surfaces are matched in an overall heat conduction solution. The heat conduction problem is solved using boundary element methods, and the inverse problem is solved using a genetic algorithm. They concluded that the GA reconstructed heat flux is robust yielding accurate results to both cases- exact input data and error-laden inputs.

Recently, Divo et al. [115,116] developed a method relying on a superposition of clusters of sources/sinks with a boundary element solution of the forward problem to solve the inverse geometric problem of detection of subsurface cavities and flaws using thermographic techniques. Their method does not require remeshing of the interior geometry as the inverse problem is solved iteratively and thus has a tremendous potential to reduce the computational burden especially for 3D applications. In the same group, Silieti et al. [117,118] introduced a hybrid

singularity superposition boundary element-based inverse problem method for the reconstruction of multi-dimensional heat flux distributions with application to film cooling holes/slots. The purpose of the inverse analysis is to determine the heat flux distribution along cooling slot/hole surfaces, which was accomplished in an iterative process by distributing a set of singularities at the vicinity of the cooling slot/hole surface inside a fictitious extension of the physical domain or along cooling hole centerline with a given initial strength distribution. A forward steady state heat conduction problem is solved using the boundary element method (BEM). A genetic algorithm (GA) iteratively alters the strength distribution of the singularities (sinks) until the measuring surfaces heat fluxes are matched, thus satisfying Cauchy conditions. Subsequent to the solution of the inverse problem, the heat flux at the inaccessible surface is computed using the BEM. The hybrid singularity superposition BEM approach thus eliminates the need to mesh the surface of the film cooling slot/hole and the need to parametrize the heat flux over that surface. Rather, the heat flux is determined in a post-processing stage after the inverse problem is solved. The results validate the approach and reveal good agreement between the BEM/GA reconstructed heat fluxes and the CHT simulated ones along the inaccessible cooling slot/hole walls.

To date, as there are no correlations or experimental data available to characterize heat transfer inside the shaped or non-shaped cooling holes/slots, and there exists a need to determine the film coefficient distributions along the walls/edges of the film cooling holes/slots. It is very important to consider the effect of heat conduction within the metal on the predictions of an accurate surface temperature and hence film cooling effectiveness in a full conjugate heat transfer finite volume models. Both the full conjugate heat transfer models as well as the inverse methodology approaches developed in this work fill the practical need of the solution of such problems.

CHAPTER 3

CONJUGATE HEAT TRANSFER SIMULATION OF FILM COOLING SLOTS

3.1 Introduction

There is a great interest in the application of film cooling to protect the engine components from high temperature gas streams. The coolant gas may be injected through holes or slots which are continuous across the span of the wall to be protected. Moreover, the injection of the coolant gas through slots can be considered a 2D problem. A main quantity of interest is the wall temperature downstream of the point of injection which is usually presented in dimensionless form as the film cooling effectiveness. Here, the effect of conjugate heat transfer on the film cooling process will be considered. Two models will applied- the adiabatic and the conjugate heat transfer models. The prediction of film cooling effectiveness from one and two cooling slots at different injection angles using different turbulence models and a blowing ratio of one will be investigated. In this study, the conjugate heat transfer model is solved by adopting the homogeneous method, in which the fluid zones (coolant and hot gas) and the solid zone (metal or endwall) are direct coupled by using same discretization and numerical approach. The turbulence models considered here include: the renormalization group k-ϵ model (RNG), the realizable k-ϵ model (RKE), the standard k-ω model (SKW), and the shear stress transfer k-ω model (SST). Since it is a 2-D problem, the predictions of two-equation model will be compared to the predictions of the Reynolds Stress Model (RSM). It also includes the velocity and temperature fields for a blowing ratio (M) closer to one. Finally, the predicted film cooling effectiveness has been compared to the analytical models as reported by Goldstein [1]. The

conjugate heat transfer solution is obtained using the finite volume-based commercial CFD code (Fluent version 6.1).

3.2 Computational Methods and Governing Equations

The time-dependent, time-averaged, compressible Navier-Stokes equations are:

$$\rho\left(\frac{\partial U_i}{\partial t} + U_j\frac{\partial U_i}{\partial x_j}\right) = -\frac{\partial p}{\partial x_i} + \frac{\partial}{\partial x_j}\left(\mu\frac{\partial U_i}{\partial x_j}\right) + \frac{\partial R_{ij}}{\partial x_j} \tag{3.1}$$

where $R_{ij} = -\overline{u_i' u_j'}$, the Reynolds (or apparent turbulent) stress tensor. The Fluent commercial CFD package has been used to solve the above equations and the energy equation in the fluid and solid regions in order to predict film cooling effectiveness, velocity, and temperature fields for conjugate film cooling from one and two slots at different injection angles. Solutions are obtained by employing a conjugate numerical methodology. This approach allows the simultaneous solution of external flow, internal convection, and conduction within the endwall, eliminating the need for decoupled solutions. Boundary conditions were specified only at the inlets of the hot and cold gases and at the exit of the mixed gases. The solution procedure used is the embodied SIMPLE (semi-implicit pressure linked equations) procedure.

3.3 Turbulence Models

The closure problem arising in turbulence deals with the necessary modeling of the Reynolds stress tensor; i.e. (R_{ij}). Here, five different turbulence models have been considered, namely, the RNG k-ϵ model (RNG), the realizable k-ϵ model (RKE), the standard k-ω model (SKW), the SST k-ω model (SST), as well as the RSM model. No claim is made with regards to contribution to the development of turbulence models, rather well-established models are used in detailed studies to compare and assess their predictions in a the setting of film cooling.

18

3.3.1 The RNG k-ε Model

The RNG k-ϵ turbulence model is derived from the instantaneous Navier-Stokes equations, using a mathematical technique called Re-Normalization Group (RNG) methods, borrowed from quantum mechanics. The analytical derivation results in a model with constants different from those in the standard k-ϵ model, and it results in additional terms and functions in the transport equations for the turbulent kinetic energy (k) and for dissipation rate (ϵ). A more comprehensive description of RNG theory and its application to turbulence can be found in [119,120]. The governing equations for this model are:

k equation:

$$\rho\frac{Dk}{Dt} = \frac{\partial}{\partial x_j}[(\mu + \frac{\mu_t}{\sigma_k})\frac{\partial k}{\partial x_j}] + \mu_t S^2 - \rho\epsilon - g_i\frac{\mu_t}{\rho Pr_i}\frac{\partial \rho}{\partial x_i} - 2\rho\epsilon\frac{k}{\gamma RT} \qquad (3.2)$$

ϵ equation:

$$\rho\frac{D\epsilon}{Dt} = \frac{\partial}{\partial x_j}[(\alpha_\tau \mu_{eff})\frac{\partial \epsilon}{\partial x_j}] + \frac{\epsilon}{k}(C_{1\tau}\mu_\tau S^2 - \rho\epsilon C_{2\tau}^*) \qquad (3.3)$$

here, D/Dt is the convective (or substantial time) derivative:

$$\frac{D}{Dt} = \frac{\partial}{\partial t} + \vec{V}\cdot\nabla \qquad (3.4)$$

and S is related to the mean strain tensor, $S_{ij} = \frac{1}{2}(\frac{\partial u_i}{\partial x_j} + \frac{\partial u_j}{\partial x_i})$, as $S = \sqrt{2S_{ij}S_{ji}}$, $C_{1\tau} = 1.42$, $C_{2\tau} = 1.68$, $C_\mu = 0.0845$, $\eta = S\frac{k}{\epsilon}$, $\mu_t = \rho C_\mu \frac{k^2}{\epsilon}$, $C_{2\tau}^* = C_{2\tau} + \frac{C_\mu \rho \eta^3 (1-\frac{\eta 1}{\eta_o})}{1+\beta\eta^3}$.

3.3.2 The realizable k-ε Model

The term realizable means that the model satisfies certain mathematical constraints on the normal stresses consistent with the physics of turbulent flows. In this model, the k equation is the same as in RNG model, but C_μ is not a constant and varies as a function of mean velocity

field and turbulence (0.09 in log-layer $S\frac{k}{\epsilon} = 3.3$, 0.05 in shear layer of $S\frac{k}{\epsilon} = 6$). The ϵ equation is based on a transport equation for the mean-square vorticity fluctuation [121] as:

$$\rho\frac{D\epsilon}{Dt} = \frac{\partial}{\partial x_j}[\left(\mu + \frac{\mu_t}{\sigma}\right)\frac{\partial\epsilon}{\partial x_j}] + C_1 S\rho\epsilon - C_2\frac{\rho\epsilon^2}{k + \sqrt{\nu\epsilon}} \tag{3.5}$$

where $C_1 = max[0.43, \frac{\eta}{\eta+5}]$, and $C_2 = 1.0$. This model is designed to avoid unphysical solutions in the flowfield.

3.3.3 The standard k-ω Model

The standard k-ω model is an empirical model based on model transport equations for the turbulence kinetic energy (k) and the specific dissipation rate (ω), which can also be thought of as the ratio of ϵ to k. As the k-ω model has been modified over the years, production terms have been added to both the k and ω equations, which have improved the accuracy of the model for predicting free shear flows. The eddy viscosity is given by $\mu=\alpha^*\rho k/\omega$, and the two equations for the turbulent kinetic energy (k) and the specific dissipation rate (ϵ) are:

k equation:

$$\rho\frac{Dk}{Dt} = \tau_{ij}\frac{\partial U_i}{\partial x_j} - \rho\beta^* k\omega + \frac{\partial}{\partial x_j}[(\mu + \frac{\mu_t}{\sigma_k})\frac{\partial k}{\partial x_j}] \tag{3.6}$$

ω equation:

$$\rho\frac{D\omega}{Dt} = \alpha\frac{\omega}{k}\tau_{ij}\frac{\partial U_i}{\partial x_j} - \rho\beta\omega^2 + \frac{\partial}{\partial x_j}[(\mu + \frac{\mu_t}{\sigma_\omega})\frac{\partial\omega}{\partial x_j}] \tag{3.7}$$

where the closure coefficients and auxiliary relations are stated in Wilcox [122].

3.3.4 The SST k-ω Model

There are two major ways in which the SST model differs from the standard model. First is the gradual change from the standard k-ω model in the inner region of the boundary layer to a high Reynolds-number version of the k-ϵ model in the outer part of the boundary layer. Second is the modified turbulent viscosity formulation to account for the transport effects of the principal turbulent shear stress. The SST, shear stress transport, model consists of the zonal (blended) k-ω/k-ϵ equations and clips of turbulent viscosity so that turbulent stress stay within what is dictated by structural similarity constant. The k equation is the same as the standard k-ω model where as the resulting blended equation for ω [123] is:

$$\rho\frac{D\omega}{Dt} = \frac{\gamma}{\nu_t}\tau_{ij}\frac{\partial U_i}{\partial x_j} - \rho\beta\omega^2 + \frac{\partial}{\partial x_j}[(\mu+\frac{\mu_t}{\sigma_\omega})\frac{\partial\omega}{\partial x_j}] + 2\rho(1-F_1)\sigma_{\omega2}\frac{1}{\omega}\frac{\partial k}{\partial x_j}\frac{\partial\omega}{\partial x_j} \qquad (3.8)$$

where $F_1 = 1$ in the inner layer and $F_1 \rightarrow 0$ in the outer layer, and $\sigma_{\omega2} = 1.168$.

3.3.5 The RSM Model

The Reynolds stress model (RSM) involves calculation of the individual Reynolds stresses, $\overline{u_i' u_j'}$, using differential transport equations. The individual Reynolds stresses are then used to obtain closure of the Reynolds-averaged momentum equation. The starting point is the exact transport equations for the transport of Reynolds stresses, R_{ij}. The governing equations are obtained by Reynolds-averaging the product of the exact momentum equations and a fluctuating velocity, which results in seven transport equations in 3D and five transport equations in 2D. The resulting equations contain several terms that must be modeled. For more details see [124,125,126].

3. 4 Film Cooling Effectiveness

To define the film cooling effectiveness, the surface temperature downstream of the cooling slot has to be measured or calculated. An expression is often used for compressible flow film cooling [1] is:

$$\eta = \frac{T - T_r}{T_{oc} - T_r} \tag{3.9}$$

Here, T_{oc} is the stagnation temperature of the cooling fluid at the point of injection, and T_r is the recovery temperature of the hot gas flow, is given by:

$$T_r = T_\infty + (Pr)^{1/3} \frac{V_\infty^2}{2Cp} \tag{3.10}$$

Film cooling in a 2D high speed flow has been analyzed in [127], where the reference temperature (enthalpy) method was combined with some of the incompressible flow analyses to obtain the film cooling effectiveness. The reference temperature T_* used is:

$$T_* = T_\infty + 0.72(T_r - T_\infty) \tag{3.11}$$

and all properties in the boundary layer are evaluated at this temperature. When the injected fluid is the same as the mainstream fluid the derived effectiveness correlations for high speed flows [1] are:

Kutateladze and Leont'ev model:

$$\eta = (1 + 0.25\xi_*)^{-0.8} \tag{3.12}$$

Librizzi and Cresci model:

$$\eta = (1 + 0.33\xi_*^{0.8})^{-1} \tag{3.13}$$

and Goldstein and Haji-Sheikh model:

$$\eta = 1.9Pr^{2/3}(1 + 0.33\xi_*^{0.8}\beta)^{-1} \tag{3.14}$$

where:

$$\xi_* = (x'/Ms)(Re_c\mu_c/\mu_*)^{-0.25}(\rho_*/\rho_\infty) \qquad (3.15)$$

$$\beta = 1 + 1.5 \times 10^{-4} Re_c(\mu_c/\mu_*)sin\alpha \qquad (3.16)$$

3.5 Computational Model, Grid and Boundary Conditions

Although it is a 2D problem, the computational model was chosen to simulate conditions typical of transonic film cooling experiments to be undertaken at UCF/SWPC Film Cooling Test Facility. The domain of the main flow was $30cm \times 16.5cm$, the coolant plenum supply was $15cm \times 8cm$ with an inlet of $3cm$, and the endwall was $15\,mm$ thick. There were three simulated models: first model has one cooling slot at an injection angle of 45°, second model also has one cooling slot but at an injection angle of 30°, and the third model has two cooling slots at injection angles of 45° and 30°, respectively. The cooling slot opening was $5mm$, and the outlet was located approximately fourty slot openings downstream from the cooling slot. A view of the computational domain is shown in Figure 3.1.

(a)	(b)
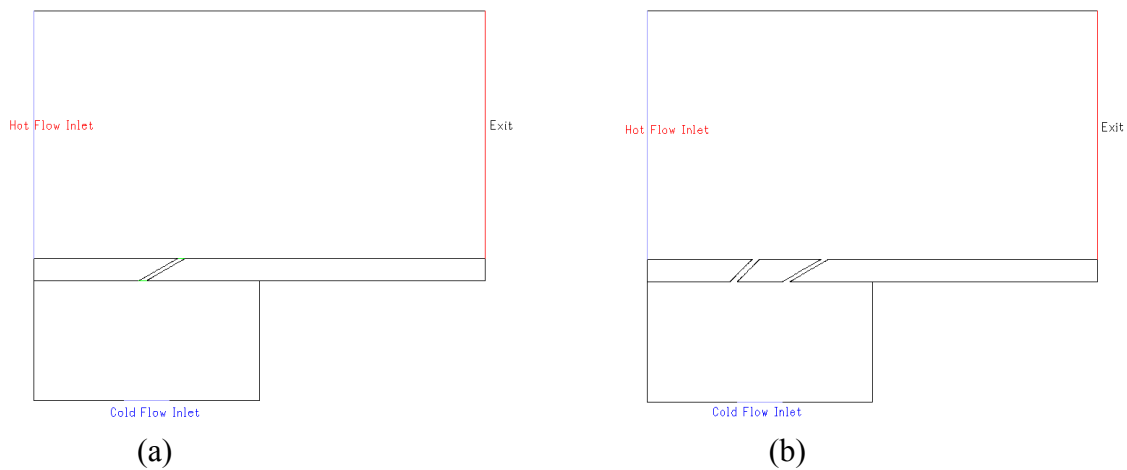
Figure 3.1. Computational domain, (a) one cooling slot, and (b) two cooling slots.

A multi-block numerical grid was used in this problem to create a structured mesh in the fluid domain and part of the solid domain. The grid was created in Gambit from Fluent, Inc. The cells in the near-wall layers were stretched away from the surfaces, and the first mesh point above the endwall was chosen such that the average y^+ is of the order of unity. A view of the computation grid for the case with two cooling slots is shown in Figure 3.2. A mesh consisting of approximately $38,000$ cells for the one cooling slot and of $55,000$ cells for the two cooling slots was used. The boundary conditions were chosen to closely model the experimental conditions. The fluid, air, was modeled as a compressible fluid using the ideal gas law, the properties of air are summarized in Table 3.1, the solid/endwall was modeled as stainless steel with properties given in Table 3.1.

(a)   (b)
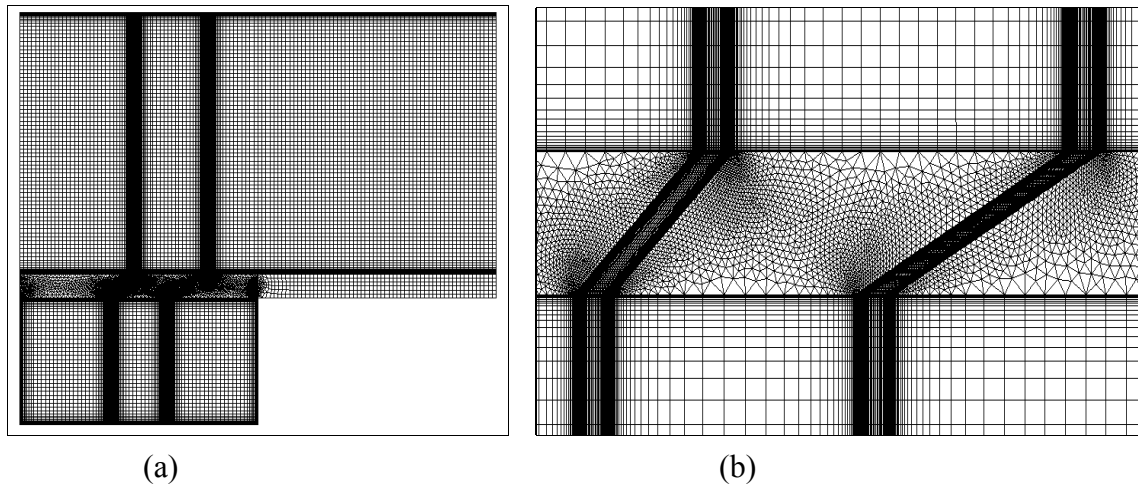
Figure 3.2. Computational grid, (a) whole domain, and (b) close up of the cooling slots.

Table 3.1. Physical properties for air and steel.

Air	T=300ºK	T= 350ºK		Steel	T=300ºK	T=350ºK
$C_P \left(\frac{J}{kg.K}\right)$	1005.7	1009		$C_P \left(\frac{J}{kg.K}\right)$	480	496
$k \left(\frac{W}{m.K}\right)$	0.02624	0.03003		$k \left(\frac{W}{m.K}\right)$	15.1	16.2
$\mu \left(\frac{kg}{m.s}\right)$	*Sutherland*	*Sutherland*		$\rho \left(\frac{kg}{m^3}\right)$	8030	8030

A profile for total pressure at the hot flow inlet was specified based on the Blasius $1/7^{th}$ power law turbulent velocity profile, as shown in Figure 3.3. The hot flow enters at a temperature of 350^oK, and a free stream turbulence intensity of 3%. The cold flow (coolant) enters at a temperature of 300^oK, and a total pressure of $105.8\,kPa$ for the one cooling slot models and $101.3\,kPa$ for the two cooling slot model. The above conditions resulted in a blowing ratios closer to one which gives the highest film cooling effectiveness.
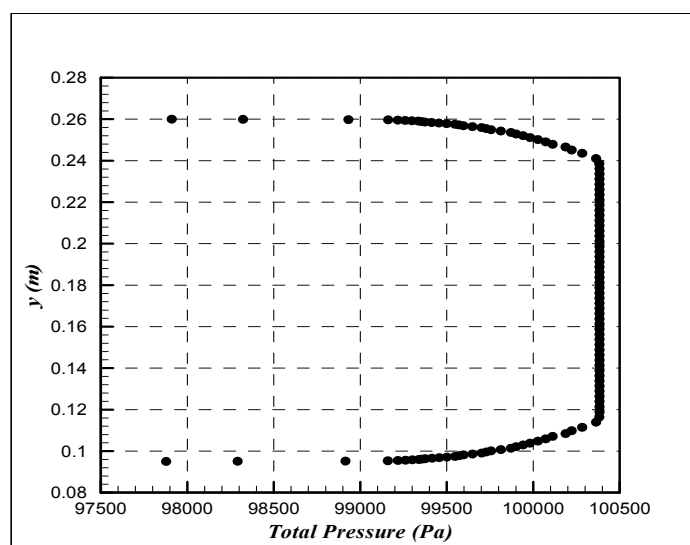
Figure 3.3. Plot of the total pressure profile (Pa) at the hot flow inlet.

3.6 Results and Discussion

The problem has been solved for the two cases; i.e. conjugate and adiabatic, with one and two cooling slots to show this effect on film cooling effectiveness. The results are converged to at least 10^{-5} for all residuals (mass, x and y velocities, energy, k and ϵ or ω....). The under-relaxation factors are for: pressure $= 0.3$, density $= 1.0$, momentum $= 0.7$, turbulent kinetic energy $= 0.8$, turbulent dissipation rate $= 0.8$, turbulent viscosity $= 1.0$, and energy $= 1.0$. These were held constant in all computations reported herein.

3.6.1 Velocity Field

The velocity field of the two cooling slot model at an injection angles of $45°$ and $30°$, respectively for $M \approx 1.0$ is shown in Figure 3.4, where the turbulence simulated using the five different turbulence models. It can be seen that all models indicate a recirculation region inside the cooling slots. The reattachment point for all models inside the cooling slots are shown in Table 3.2, whereas the reattachment point along the endwall after the first cooling slot is shown in Table 3.3. It can be seen that there is no reattachment point after the second cooling slot where the injection angle is $30°$. The predicted velocity profiles at the exit of the cooling slots are shown in Figure 3.5. Clearly there is a wide range of predictions depending on the turbulence model applied. For instance, the reattachment point after the bend in the $45°$ inclined slot varies from 0.28 for the standard k-ω model to 2.05 for the standard and RNG k-ϵ models, with the RSM model close to the k-ϵ predictions. The predicted values are somewhat closer for all models for the $30°$ inclined slot. On the other hand, the k-ω models overpredict the value of the location of the reattachment point past the exit of the jet as compared to the k-ϵ models. Consistently, the RSM model predicts values of the reattachment point location between the ones predicted by k-ϵ models and the k-ω models. The k-ϵ and RSM models predicted a variation in the jet exit velocity profile with a peak at approximately the jet centerline for the $45°$ angle slot while the k-ω models predict much flatter profiles. All models more or less are in a good agreement for the $30°$ angle slot.

(a) RNG

(b) RKE

(c) SKW

(d) SST

(e) RSM
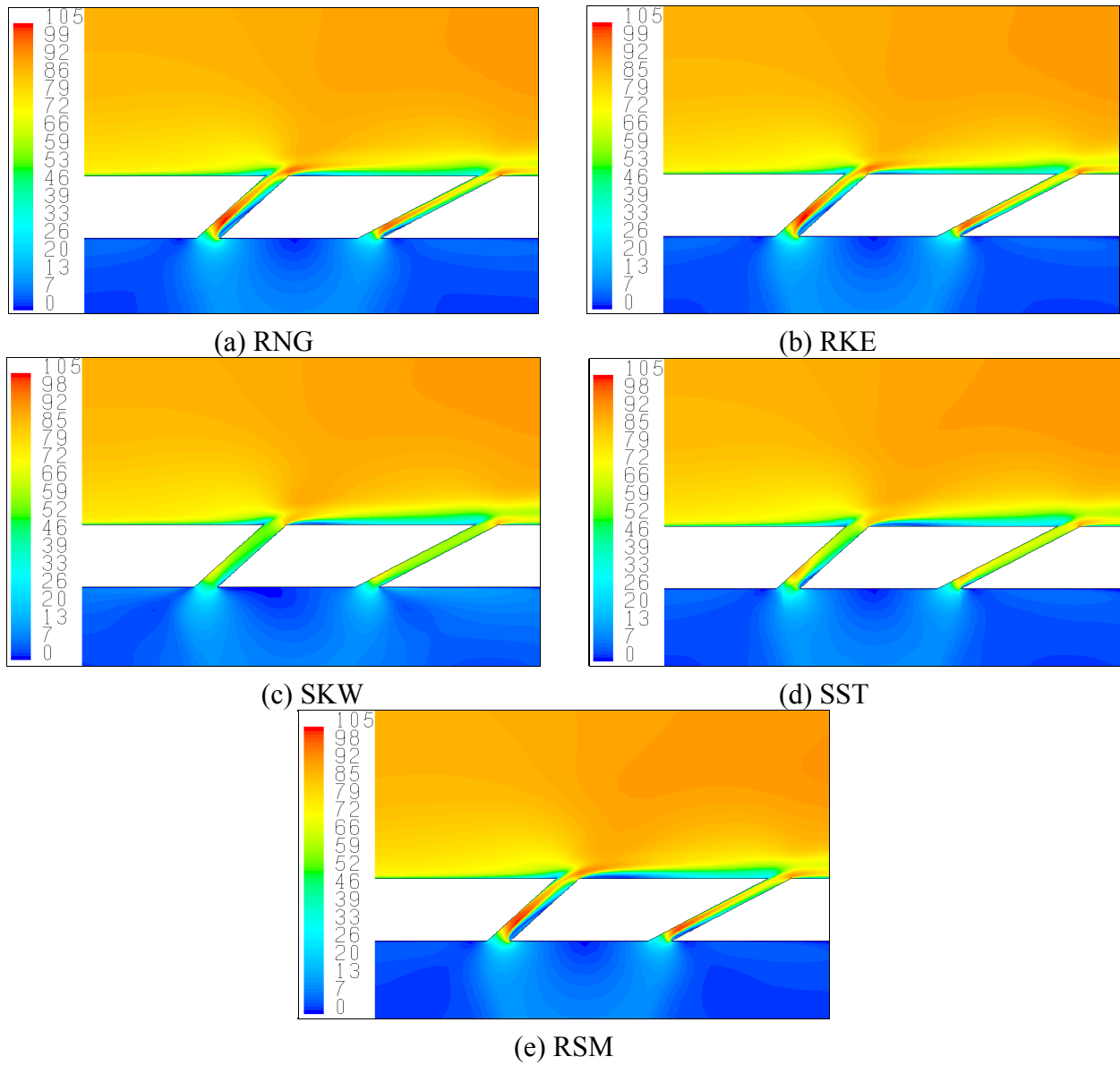
Figure 3.4. Velocity contours (m/sec) predicted by various turbulence models.

Table 3.2. Reattachment point inside the cooling slots.

Turbulence Model	45° Cooling Slot, $\left(\frac{\varsigma}{s}\right)$	30° Cooling Slot, $\left(\frac{\varsigma}{s}\right)$
RNG k-ϵ	2.0556	2.1437
Realizable k-ϵ	2.0556	2.0456
Standard k-ω	0.2824	1.1490
SST k-ω	1.0981	1.4856
RSM	1.9273	1.8640

Table 3.3. Reattachment point along endwall after first cooling slot ($\alpha = 45^{\circ}$).

Turbulence Model	$\left(\frac{x'}{s}\right)$
RNG k-ϵ	0.98374
Realizable k-ϵ	0.98374
Standard k-ω	1.98236
SST k-ω	2.91786
RSM	1.57310

(a)　　$\alpha = 45°$　　　　　　　　　　(b) $\alpha = 30°$
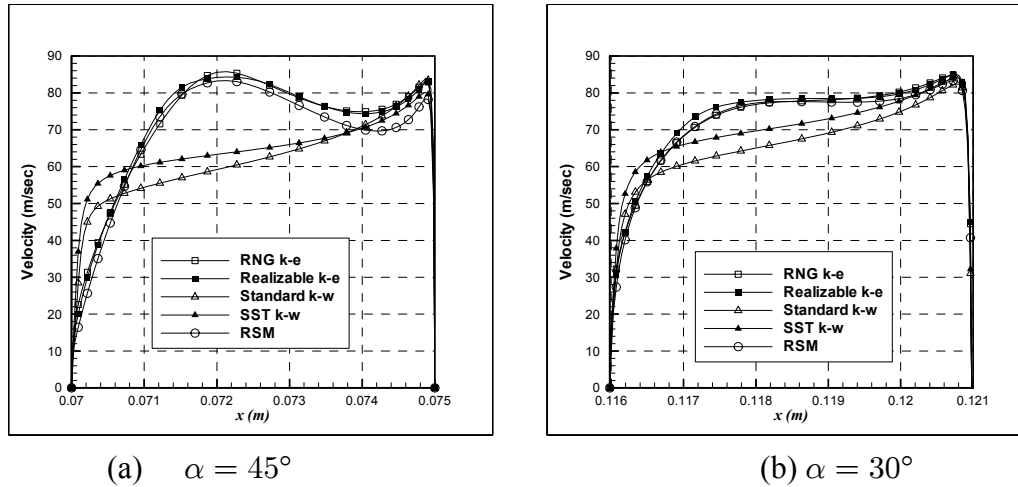
Figure 3.5. The predicted velocity (m/sec) at the exit of the cooling slots using different turbulence models.

3.6.2 Temperature Field

Figure 3.6 shows the temperature contours predicted by five turbulence models at a blowing ratio of $M \approx 1.0$ and an injection angles of $\alpha = 45°$ and 30°, respectively. The calculated temperatures at the endwall are presented in Figure 3.7. Figure 3.7(a) shows the calculated temperature at the endwall after the first cooling slot, there is a difference of almost one degree between the predictions of k-ϵ and RSM models and the predictions of the k-ω models. Whereas the calculated temperatures after the second cooling slot are within approximately one half degree difference for all turbulence models as shown in Figure 3.7(b). The difference in predicted wall temperatures in the vicinity of the cooling slot exit is attributed to the variation in

predicting the separation region appearing after the 45° slot as predicted by all turbulence models. Whereas, the agreement of all five turbulence models in the predicted temperatures in the vicinity of the cooling slot occurs for the 30° where there is no separation present. Moreover, after around 20 slot openings past the 30° cooling slot exit, all turbulence models continue to predict similar wall temperatures, while the realizable k-ϵ model underpredicts the temperature by up to 30%.

(a) RNG

(b) RKE

(c) SKW

(d) SST

(e) Conjugate with RSM

(f) Adiabatic with RSM
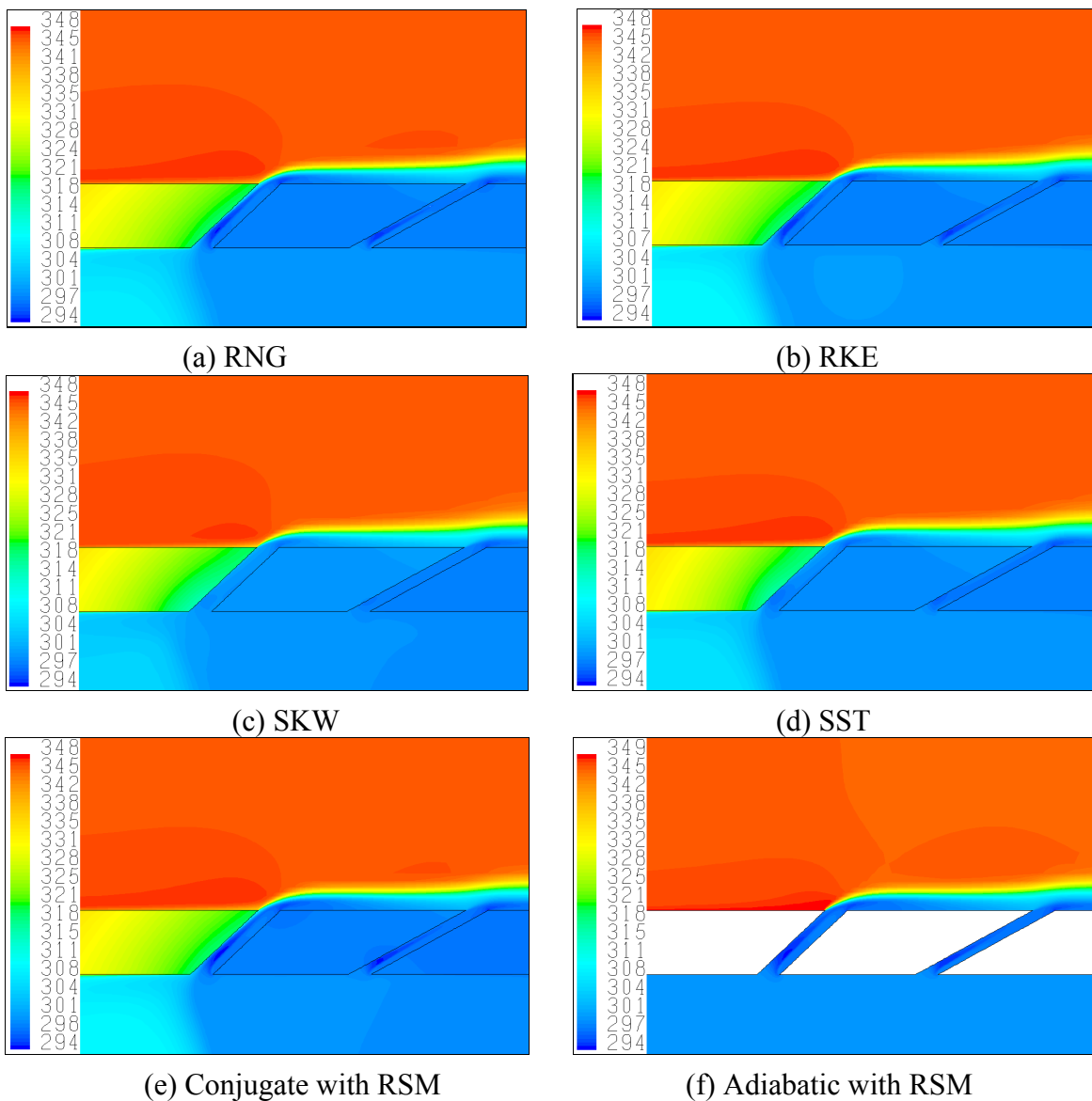
Figure 3.6. Predicted temperature ($Kelvin$) contours using different turbulence models.

(a) after 45° cooling slot	(a) after 30° cooling slot
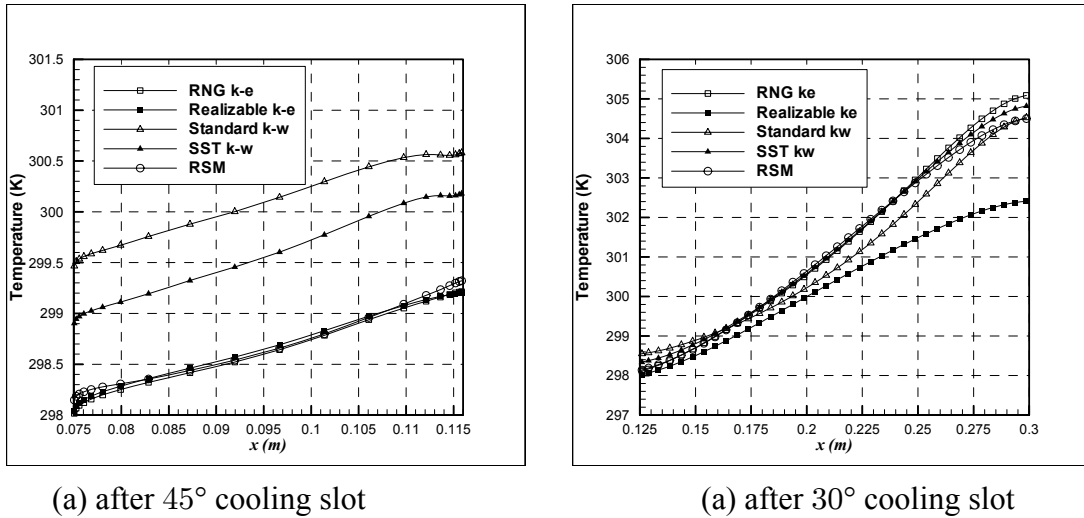
Figure 3.7. Predicted temperature ($Kelvin$) along the endwall using different turbulence models.

3.6.3 Film Cooling Effectiveness

The predictions of the film cooling effectiveness are shown in Figure 3.8. Here, results are predicted for one cooling slot using the RNG k-ϵ turbulence model at a blowing ratio of 1.4. Figure 3.8(a) shows the calculated conjugate and adiabatic film effectiveness at an injection angle of $\alpha = 30°$ compared to the analytical models: Kutateladze, Librizzi, and Goldstein models. Figure 3.8(b) shows the results for the case of the injection angle of 45°. It can be seen that the calculated and the predicted ones are in a better agreement for the injection angle of 30° than the injection angle of 45°.

In Figure 3.9, the film cooling effectiveness is shown for the case with two cooling slots at different injection angles and a blowing ratio of approximately one. Here the Reynolds number was defined as $Re_c = \rho_c V_c s / \mu_c$, where the subscript c denotes the coolant and s is the slot opening. Figure 3.9(a) shows the predicted ones using the five turbulence models, and Figure 3.9(b) shows a comparison between the predicted ones and the analytical models. It can be seen that there is an approximately 10 % difference between the adiabatic and the conjugate

film effectiveness, and a large difference between the predicted film effectiveness values and calculated ones based on the analytical models.
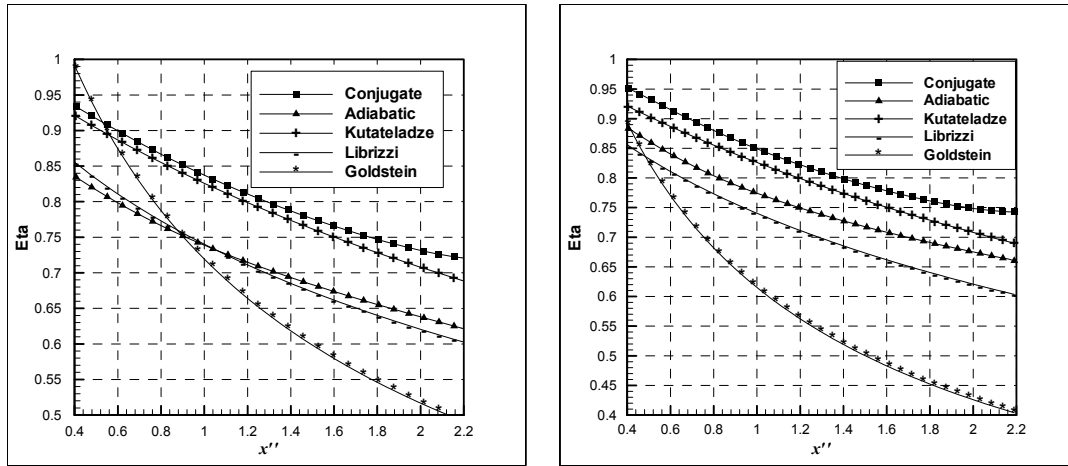
(a) results for slot injection angle $\alpha = 30°$ (b) results for slot injection angle $\alpha = 45°$

Figure 3.8. Film cooling effectiveness with one cooling slot at different injection angles using RNG k-ϵ turbulence model.
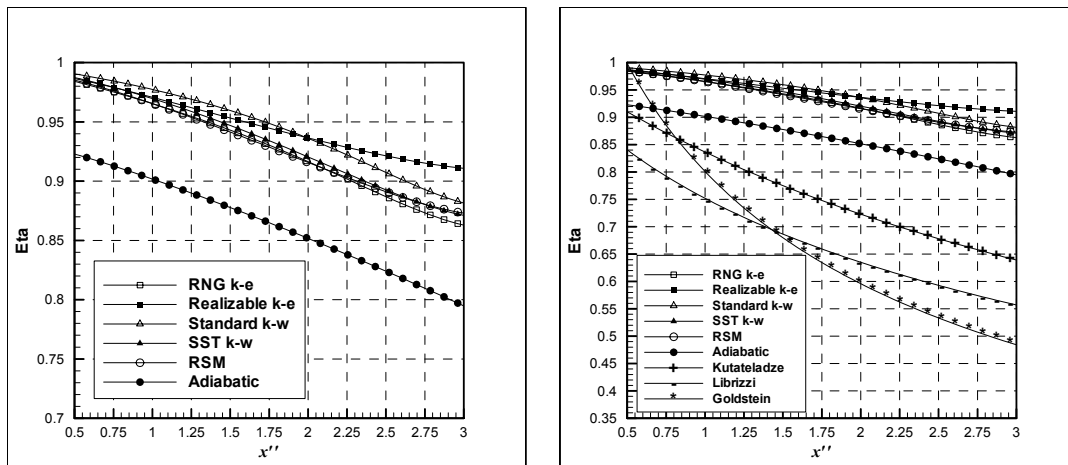
Figure 3.9. Film cooling effectiveness with two cooling slots at $45°$ and $30°$, respectively: comparison of predicted effectiveness with computed effectiveness using analytical models.

The predicted results show that the conjugate heat transfer model has a strong influence on the predicted film cooling effectiveness compared to the adiabatic and the analytical models,

especially for the cases of two cooling slots. We found that both versions of k-ϵ and RSM models yielded essentially the same results with slight deviations. In contrast, the two versions of k-ω model underpredict the flow field in comparison with the other three models, and overpredict the temperature field. The predicted film cooling effectiveness is in better agreement with the analytical models for the cases of one cooling slot. In terms of film cooling effectiveness, the conjugate heat transfer model produces significant differences in comparison with the adiabatic and analytical models. Based on these results, the above effects will be introduced into 3D models for the cases of cylindrical and fan-shaped cooling holes, which will be the subject of the next two chapters.

CHAPTER 4

CONJUGATE HEAT TRANSFER SIMULATION OF CYLINDRICAL FILM COOLING HOLES

4.1 Introduction

As mentioned above, the secondary gas or the coolant usually introduced through slots or holes, here, the film cooling effectiveness, will be simulated for the adiabatic and conjugate heat transfer models for 3D cylindrical film cooling holes. Moreover, the predictions from those simulations will be compared to experimental data available in the open literature. We will extend the 2D simulations into 3D simulations to investigate the predictions of film cooling effectiveness from single, scaled-up cylindrical film cooling hole geometry at an injection angle of 30°. The flow conditions considered are a blowing ratio of 2.0, and the coolant-to-mainflow temperature ratio of 0.54. Turbulence closure was obtained using five different turbulence models; the standard k-ϵ model (SKE), the RNG k-ϵ model (RNG), the realizable k-ϵ model (RKE), the standard k-ω model (SKW), as well as the SST k-ω model (SST). Also, the velocity and temperature fields, in addition to centerline and two-dimensional film cooling effectiveness, will be presented. Finally, the predicted centerline film cooling effectiveness will be compared to those reported in the open literature by Gritsch et al. [34].

4.2 Validation Test Case: Cylindrical Cooling Hole

To verify the numerical approach, we used the data reported in the open literature by Gritsch et al. [34]. A complete description of their experimental facility, including the test section, and instrumentation used, is given in [32,34]. The facility was used to conduct detailed

measurements of adiabatic film cooling effectiveness for injection from single scaled-up film cooling hole geometries at the University of Karlsruhe. The geometries investigated included a cylindrical hole and two holes with a diffuser-shaped exit portion.

The film cooling test rig consisted of a primary loop representing the external (crossflow) flow and a secondary loop representing the internal (plenum) flow, see Figure 4.1. In the primary loop, the test section is 90 mm in width and 41 mm in height. In contrast, the secondary channel has a cross-sectional area at the film cooling hole of 60 mm in width and 20 mm in height. The injection (inclination) angle of the film cooling hole is ($\alpha = 30°$) with a diameter of 10 mm, and length-to-diameter ratio of ($L/D = 6$).

The flow parameters investigated were typical for real film cooling applications. Each hole geometry was tested for a matrix of three internal (plenum) Mach numbers ($Ma_c = 0.0, 0.3, 0.6$) and three external (crossflow) Mach numbers ($Ma_c = 0.3, 0.6, 1.2$). The coolant supply passage internal Mach number of ($Ma_c = 0.0$) corresponds to the plenum condition. The coolant-to-mainflow temperature ratio was 0.54, and a blowing ratio up to 2.0.

(a)

(b)
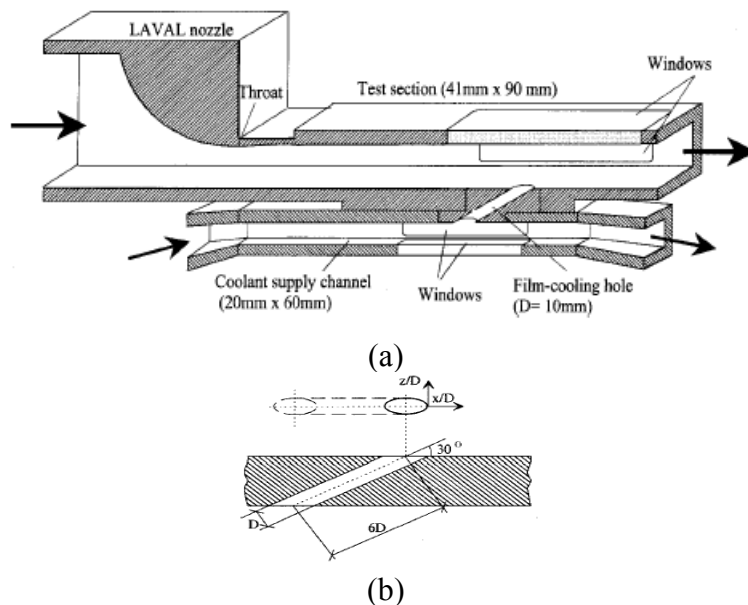
Figure 4.1. Geometry of the experimental test case used in this study: (a) overall setup; (b) film cooling hole details from Gritsch et al. [34].

4.3 Numerical Method

In this study a systematic computational methodology is adopted, this methodology stresses accurate computational models of the physical problem, including simultaneous, fully elliptic solution of the mainstream, cooling hole, and plenum regions; high quality 3D grid generation techniques; the use of a high-order discretization scheme to reduce numerical errors significantly; and effective turbulence modeling [53].

4.3.1 Geometry

The computational domain for the adiabatic cases matched the experimental test case. The solid models of the whole assembly are shown in Figure 4.2. For the adiabatic cases, the computational domain included the coolant supply channel (plenum), the film cooling hole, and the main channel (cross hot flow), see Figure 4.2a, the crossflow test section was 90 mm in width and 41 mm in height, and plenum cross-section was 60 mm in width and 20 mm in height. The diameter of the film hole was 10 mm with an injection angle of 30°. The exit plane for the crossflow was located far downstream of the cooling hole; i.e. $x/D = 30$, as shown in see Figure 4.2c. The conjugate model was the same as the adiabatic model, see Figure 4.2b, but it had an endwall with a cross-sectional area of 90 mm in width and 30 mm in height. Moreover, the width of the plenum had been adjusted from 60 mm to 90 mm. The geometry was generated using Gambit 2.1.2 from Fluent, Inc.
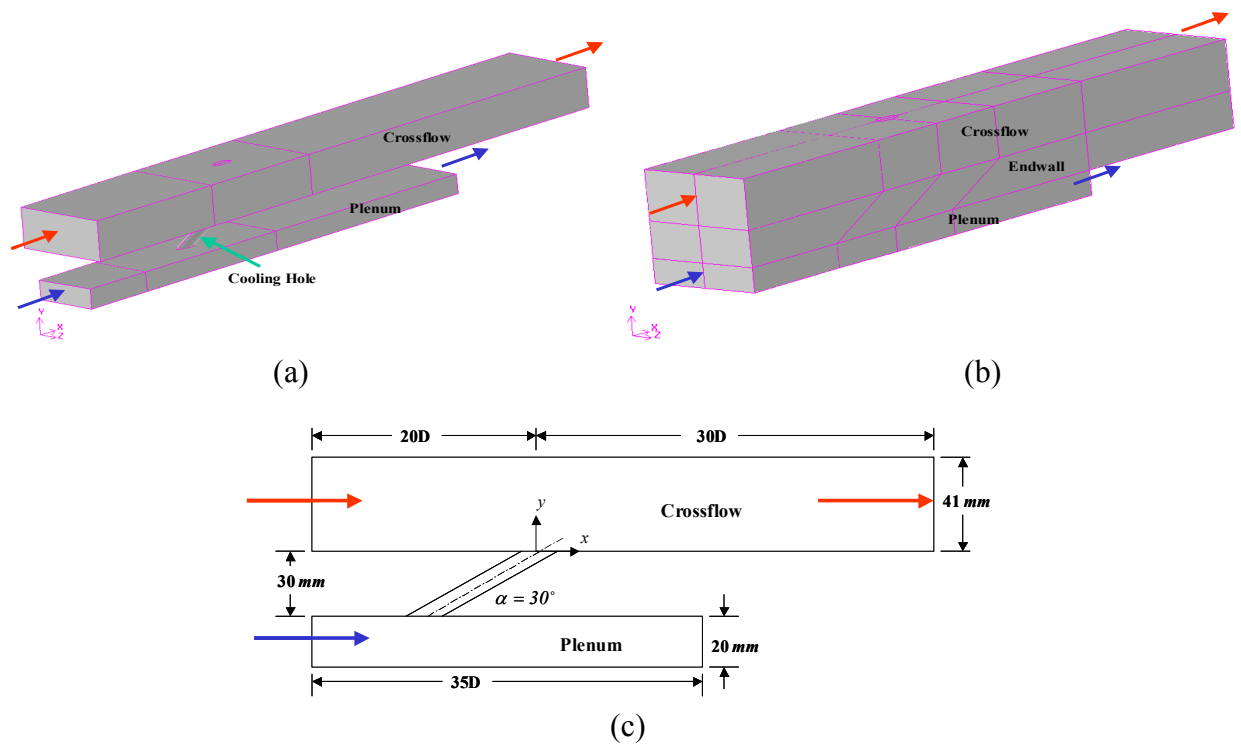
Figure 4.2. Computational domain; (a) solid model of the adiabatic cases, (b) solid model of the conjugate case, and (c) schematic diagram.

4.3.2 Grid

A multi-block numerical grid was used in the present work to allow the highest quality in all regions with the fewest number of cells. Multi-blocking refers to a technique in which the domain is partitioned into several different subsections in order to achieve the maximum control over the grid quality and density. Each section was then meshed using an appropriate topology. For the above reason, the model was partitioned into 24 blocks for the adiabatic cases and 34 blocks for the conjugate case, this allowed the use of a hexahedral mesh in all blocks to achieve a high aspect ratio especially near the walls. The total number of computational cells was 950,690 for the adiabatic cases, and 1,266,992 for the conjugate case. The grid was created in Gambit from Fluent, Inc. The cells in the near-wall layers were stretched away from the surfaces, and the first mesh point above the end wall is chosen such that the average y^+ is of the order of

unity or less. A view of the computational grid for the adiabatic and conjugate cases is shown in Figures 4.3 and 4.4, respectively. To achieve grid independent solutions, three different grids were tested, $Grid_1$ with 378,864 cells, $Grid_2$ with 680,768 cells, and $Grid_3$ or final grid with 950,690 cells. The last grid resulted in a negligible change of the computed film cooling effectiveness downstream the film cooling hole as shown in Figure 4.5. It can be seen that the results of $Grid_3$ can be judged to be grid independent solutions. The results from the $Grid_3$ are presented here.

(a)   (b)   (c)
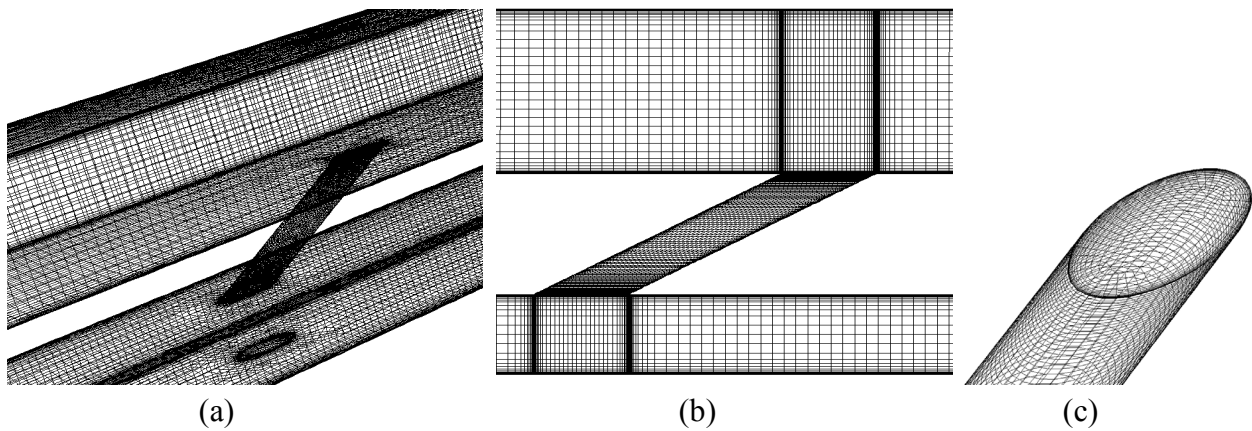
Figure 4.3. Details of the grid used in the adiabatic case: (a) whole domain; (b) $z = 0$ symmetry plane; (c) surface mesh for the film cooling hole.

(a)   (b)
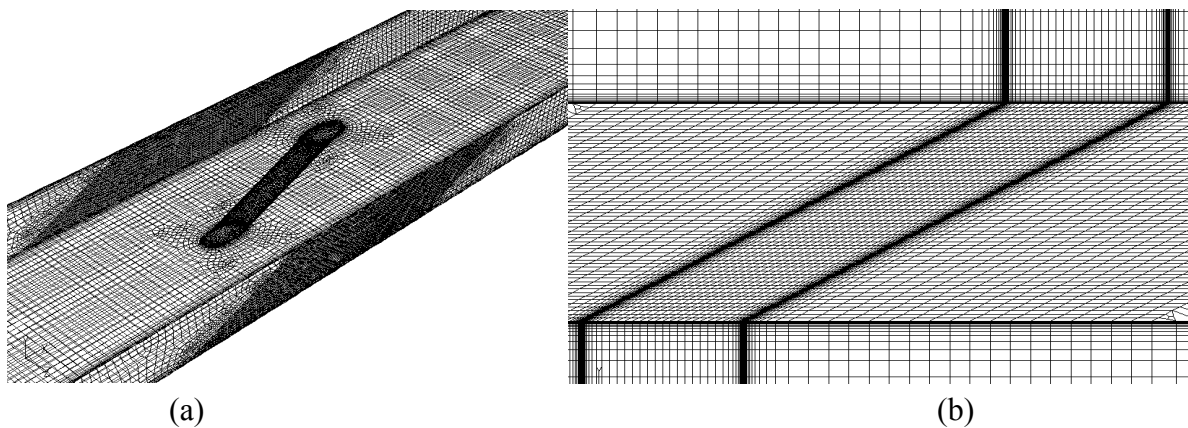
Figure 4.4. Details of the grid used in the conjugate case: (a) surface mesh for the endwall with film-cooling hole; (b) $z = 0$ symmetry plane.
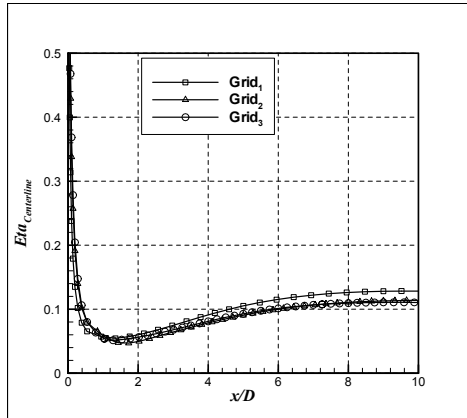
Figure 4.5. Centerline local effectiveness (η) for grid independent solutions.

4.3.3 Boundary Conditions

The boundary conditions were chosen to match the experimental test case as closely as possible. The total pressure and total temperature were imposed at the channels inlets, and static pressure at the outlets. The total temperature at the primary (crossflow) channel inlet was $540K$, and $290K$ in the secondary (plenum) channel inlet, thus the coolant-to-mainflow temperature ratio was 0.54, which can be assumed to be more representative for typical gas turbine applications. To achieve a blowing ratio of 2.0, the total pressure in the plenum was set to $109750Pa$, whereas, the total pressure at the mainflow inlet was $100400Pa$, and the static pressure at the outlet was $96950Pa$. This resulted in a momentum ratio of 2.5 and a Reynolds number of ($Re_c = 6.8 \times 10^4$). Inlet turbulence levels were set to 1.5% and 1% in the primary and secondary channels, respectively. The fluid, air, was modeled as a compressible flow using ideal gas law, whereas the other properties; i.e. specific heat ratio, thermal conductivity, and dynamic viscosity are piecewise-linear functions of temperature. For the conjugate case, the endwall material was AISI 347 stainless steel, with a density of ($7978kg/m^3$), the other

properties, i.e. specific heat ratio, and thermal conductivity are piecewise-linear functions of temperature.

4.3.4 Turbulence Modeling

To investigate the effect of turbulence modeling on film cooling effectiveness, turbulence closure was obtained using five different turbulence models: the standard k-ϵ model (SKE) of Launder and Spalding [128], the RNG k-ϵ model (RNG) of Yakhot and Orszag [119], the realizable k-ϵ (RKE) model of Shih [121], the standard k-ω model (SKW) of Wilcox [122], and the SST k-ω (SST) model of Menter [123]. The two-equation approach to turbulence modeling for film cooling problems is considered a "standard" due to ease of implementation and computational economy. The impact of each of the five turbulence models on the prediction of film cooling effectiveness was compared to experimental data [34] in the results section below.

4.3.5 Film Cooling Effectiveness

To define film cooling effectiveness, the surface temperature downstream of the cooling hole has to be measured. To be consistent with the experimental data reported by Gritsch et al. [34], the definition of the local film cooling effectiveness (η) was based on the mainflow recovery temperature as a reference temperature:

$$\eta(x/D, z/D) = \frac{T(x/D, z/D) - T_{r,m}}{T_{tc} - T_{r,m}} \tag{4.1}$$

here, $T(x/D, z/D)$ is the local temperature, and it is the adiabatic temperature for the adiabatic cases $T_{AW}(x/D, z/D)$, or the conjugate temperature for the conjugate case, $T_{Conj}(x/D, z/D)$. T_{tc} is the mass-weighted average temperature of the coolant at the exit of the cooling hole, and $T_{r,m}$, the recovery temperature of the mainflow, is given by:

$$T_r = T_\infty + (Pr)^{1/3} V_\infty^2 / 2Cp \qquad (4.2)$$

In the experiment [34], the mainflow recovery temperature was measured on the test plate at a location not affected by the coolant ejection, for this reason; the recovery temperature was calculated at a location of $(x/D = -5)$.

4.3.6 Solver

The simulations were processed using Fluent version 6.1.22 software from Fluent, Inc. The discretization was a second-order with double precision accuracy. In the fluid zones, the steady, times-averaged Navier-Stokes equations were solved, and pressure-velocity coupling was achieved with a pressure correction algorithm. In the solid zone, only the Fourier equation for heat diffusion was solved. At the fluid-solid interfaces, an energy balance was satisfied at each iteration, such that the heat flux at the wall on the fluid side was equal in magnitude and opposite in sign to the heat flux on the solid side. The temperature of the boundary itself was adjusted during each iteration to meet this condition.

Convergence was determined with the following strict criteria: 1) reduction of all residuals of at least four orders of magnitude, and were no longer changing; 2) global mass and energy imbalances dropped below 0.001%; and 3) the flow field was unchanging, and the endwall surface temperature did not vary with additional iterations, and thus a "steady state" had been achieved.

4.4 Results and Discussion

The present cases were primarily concerned with the computational prediction of adiabatic and conjugate effectiveness downstream of a 3D cylindrical film cooling hole. The

results were obtained for $L/D = 6.0$, blowing ratio of 2.0, and coolant-to-mainflow temperature ratio of 0.54. First, the results will present the adiabatic model cases with five different turbulence models, then, the conjugate model cases predicted by the RKE turbulence model.

4.4.1 Velocity Field Results

Since the thermal field of a jet-in-crossflow interaction is dictated by the hydrodynamics, the flow field results were predicted by five turbulence models. The computed near-field velocity contours (m/sec) along the centerline plane $(z = 0)$ are shown in Figure 4.6, where the turbulence closure was simulated using the five different turbulence models. As it can be seen that all models predicted the low momentum region along the downstream edge and the corresponding high momentum or jetting region along the upstream edge within the film cooling hole. Figures 4.7 and 4.8 show the velocity contours and profiles at the cooling hole exit plane. The SKE, the RKE, and the SST predictions are very close to each other with a skewed upstream velocity profiles, whereas, the SKW predicted a flat profile, and on the other hand, the RNG predicted an upstream and downstream skewed velocity profile. Those profiles are function of the separation bubble and reattachment region within the film hole. The predicted reattachment region by SKE, RNG, RKE, and SST is approximately at the inlet of the cooling hole, whereas, SKW predicts a larger separation bubble and the flow separates almost at $(L/D = 2)$.

(a) SKE   (b) RNG

(c) RKE   (d) SKW
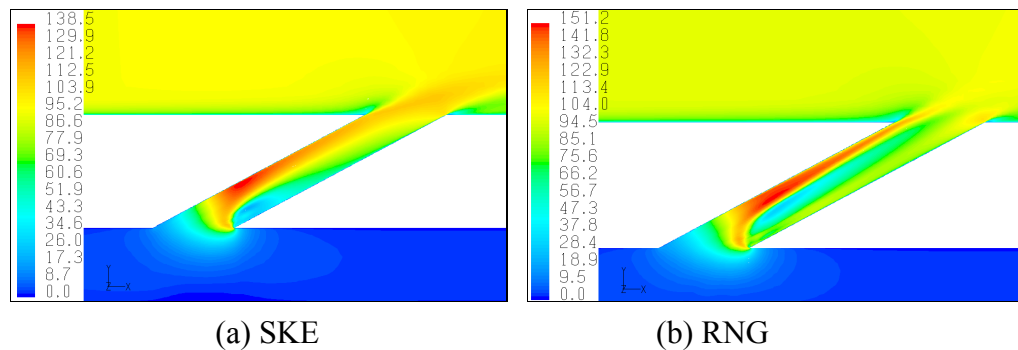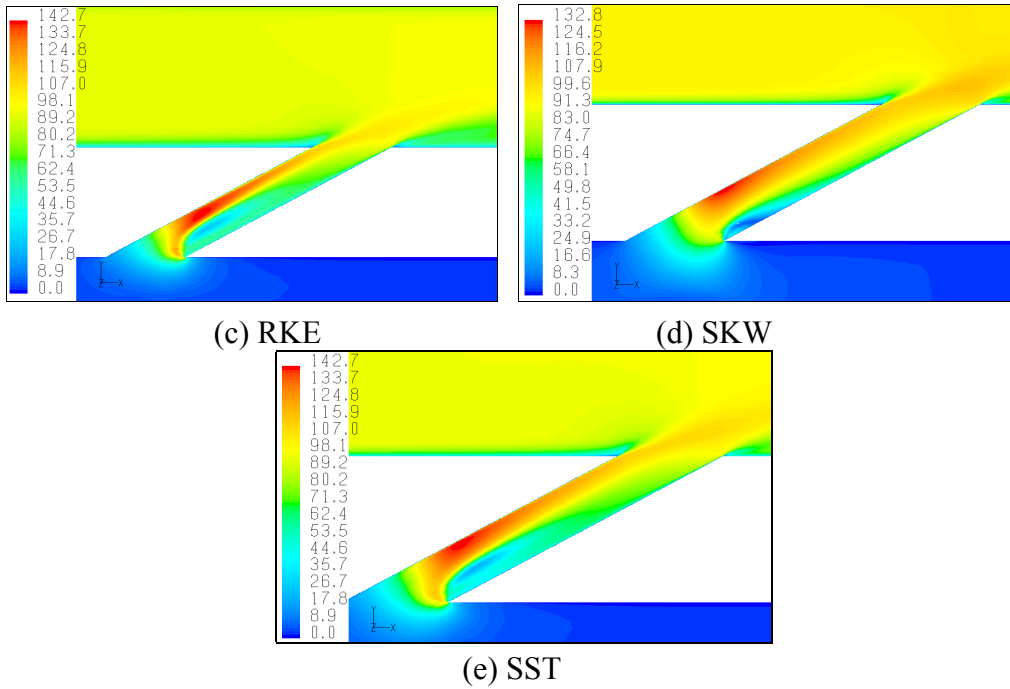
(e) SST

Figure 4.6. Velocity magnitude contours (m/sec) predicted by five different turbulence models along centerline plane in the film cooling hole region.

(a) SKE   (b) RNG

(c) RKE   (d) SKW
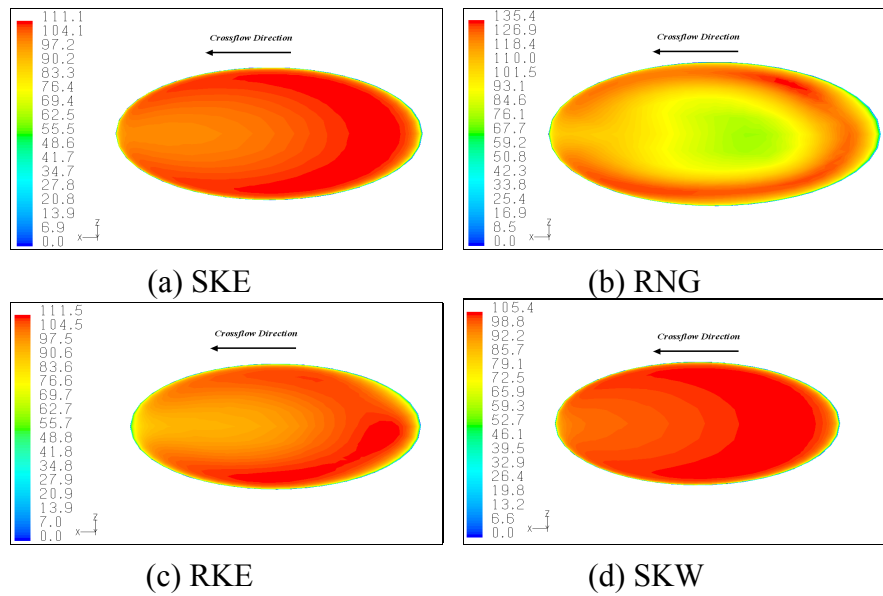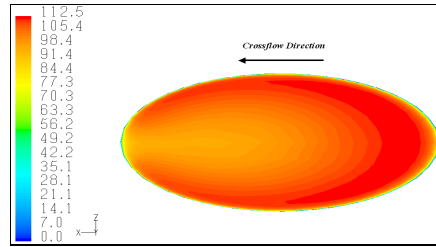
(e) SST

Figure 4.7. Velocity magnitude contours (m/sec) in the film hole exit plane predicted by the five turbulence models.
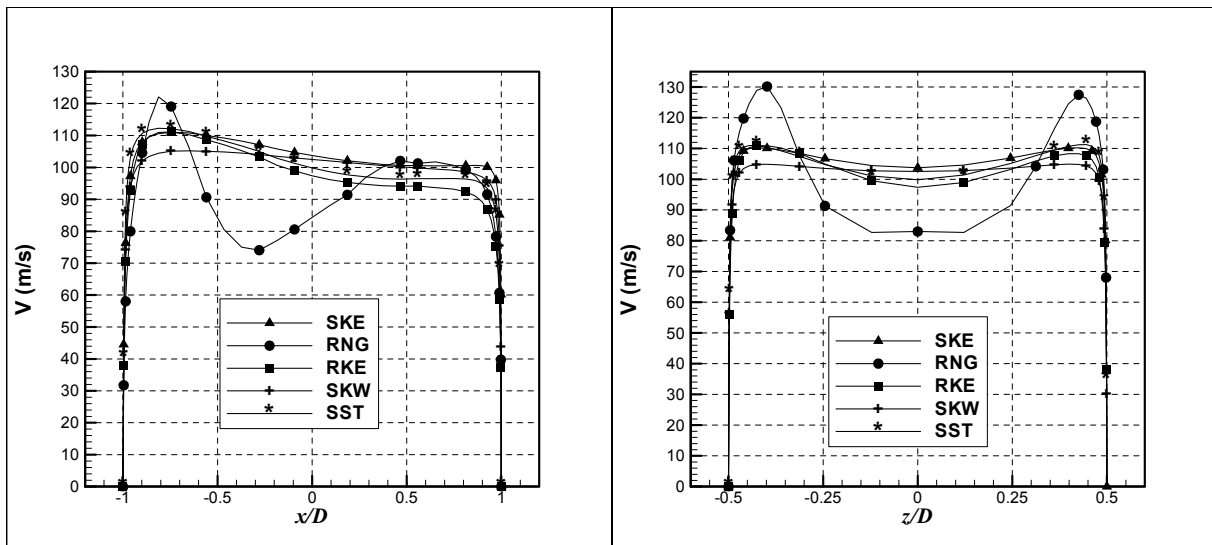
Figure 4.8. Exit plane velocity profiles (m/sec) predicted by five different turbulence models.

4.4.2 Film Cooling Effectiveness Results

In this section, the local centerline and two-dimensional distribution of the film cooling effectiveness for the adiabatic and conjugate cases are reported. Note that the streamwise distances are measured from the trailing edge $(x/D = 0)$ of the film hole at the exit plane. Figure 4.9 shows comparisons of computed centerline effectiveness with the data of Gritsch et al. [34] for five different turbulence models.

43
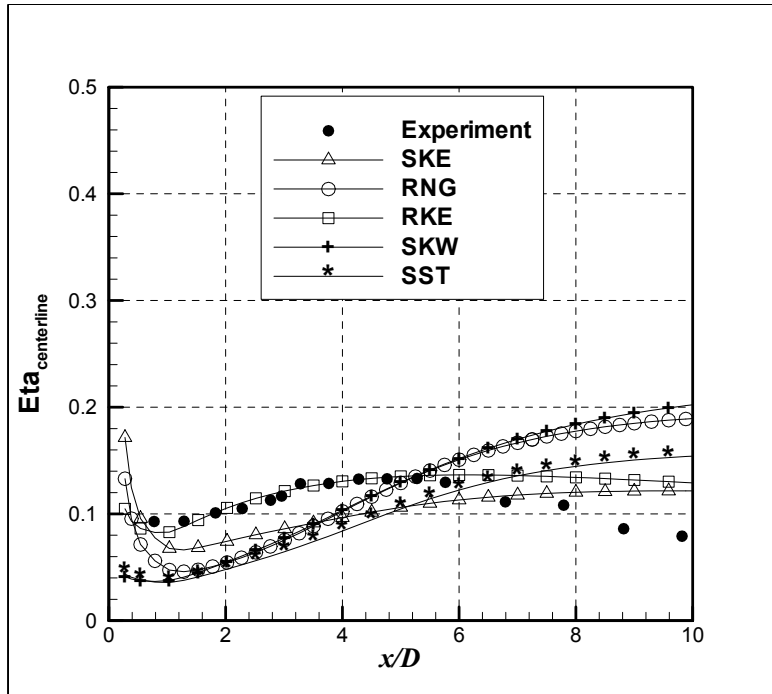
Figure 4.9. Comparison of computed centerline adiabatic effectiveness (η) with data of Gritsch et.al [34].

For clarity, the axial range can be classified into two regimes: immediate region for ($x/D \leq 6$), and intermediate region ($x/D > 6$). All turbulence models predicted the jet lift-off. In the region ($x/D \leq 6$), the RKE model gave the best results compared to the experimental data, whereas, the other four models tend to underpredict the experimental results, and the effectiveness computed by RNG and SKW are almost identical. In the intermediate region ($x/D > 6$), all turbulence models overpredicted the experimental results. The SKE model gave the closest results compared to the experimental data and SKW model gives the farthest results from the experimental data. Overall, the k-ϵ models, especially RKE, gave better results compared to k-ω models. For this reason, the RKE model had been used for the conjugate case.

Figure 4.10 shows the two-dimensional distribution of the local film cooling effectiveness for the five adiabatic cases, as well as, the conjugate case predicted by the RKE turbulence model. Qualitatively, all turbulence models tend to agreed with the experiment [34],

whereas, the distribution of the film cooling effectiveness for the conjugate case was significantly different. The centerline effectiveness for the adiabatic and conjugate cases compared to the experiment is shown in Figure 4.11. It can be seen a significant improvement in the conjugate effectiveness by up to three-times in the immediate region $(x/D \leq 6)$ in comparison to the adiabatic and experimental cases.

(a) SKE   (b) RNG

(c) RKE   (d) SKW

(e) SST   (f) Conj.
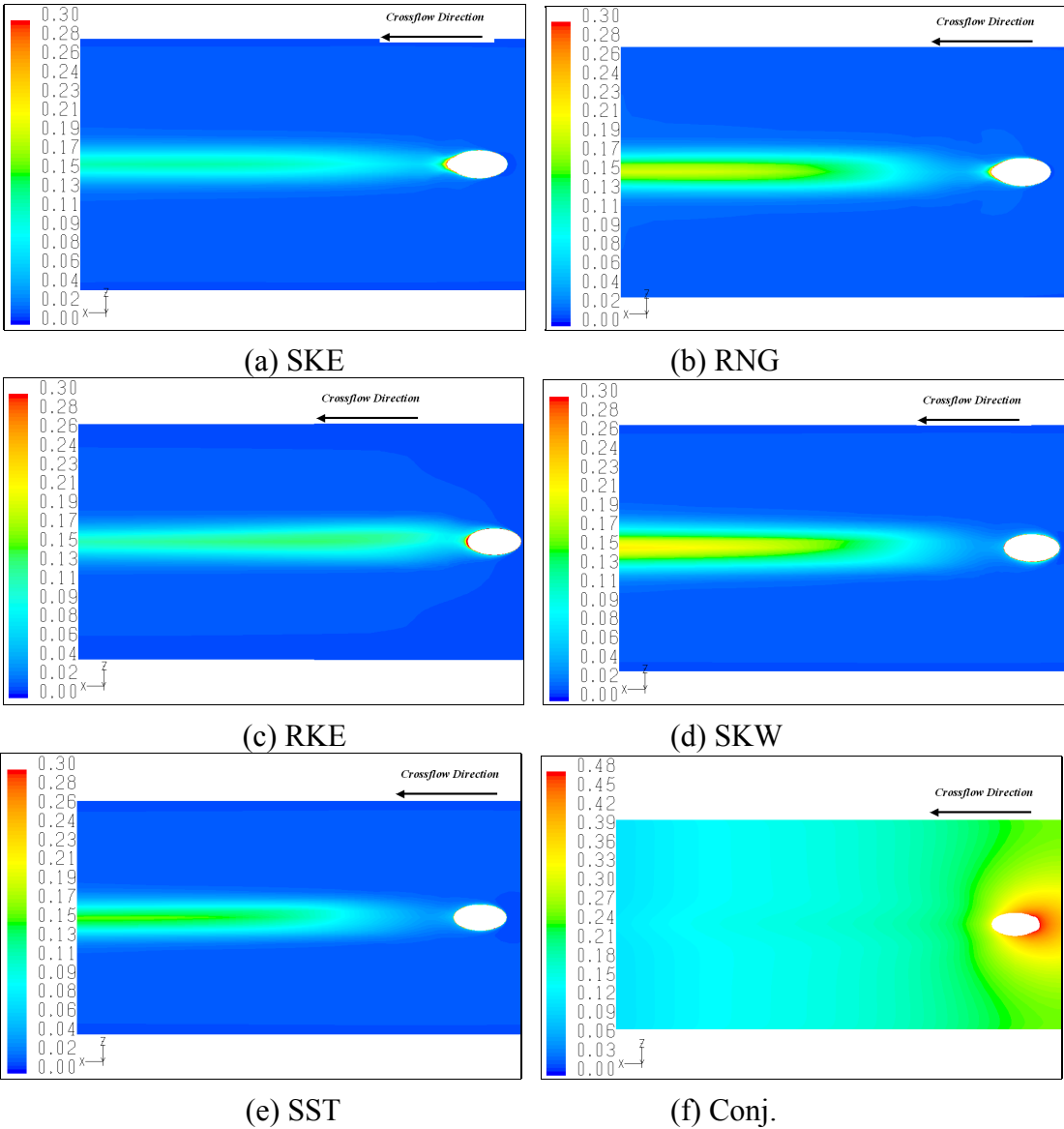
Figure 4.10. Local adiabatic and conjugate effectiveness (η) predicted by five different turbulence levels.
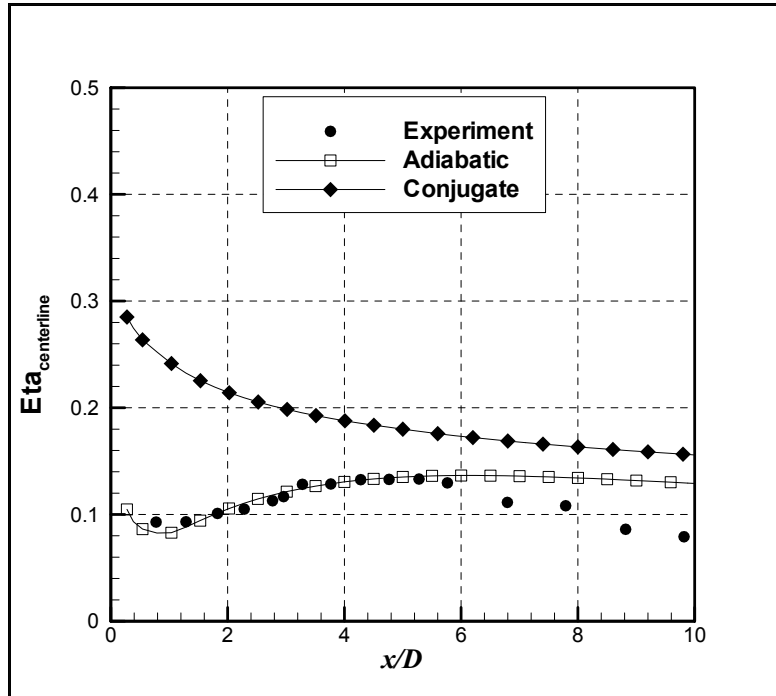
Figure 4.11. Comparison of centerline adiabatic and conjugate effectiveness (η) with the data of Gritsch et.al [34].

4.4.3 Temperature Field Results

This section presents the temperature distribution in Kelvin for the cases of adiabatic and conjugate heat transfer models. Since the RKE turbulence model gave the best agreement with experimental data as shown in the film cooling effectiveness section, it had been used to predict the adiabatic and conjugate cases results. Figure 4.12 shows the computed near hole centerline temperature contours for the adiabatic and conjugate cases, respectively. Whereas, the temperature contours for both cases at downstream location of $(x/D = 5)$ is shown in Figure 4.13. For the conjugate case, heat fluxes from the hot mainflow into the wall lead to heating up of the solid body. At the film cooling hole, an additional temperature increase of the cooling jet in comparison to the adiabatic case occurs because of the heat transfer from the hot wall into the

cooling jet, see Figure 4.14. An isometric view of temperature contours on the endwall and close to the cooling hole region is presented in Figure 4.15 for adiabatic and two conjugate cases, respectively. The conjugate cases were one with very low thermal conductivity $(0.2\,W/m.K)$, which corresponds to a TECAPEK endwall material, and the other conjugate case was for a stainless steel endwall material. These figures show clearly the differences in the temperature contours for both cases, which confirm that the conjugate heat transfer model can take into account the mutual influences of heat transfer on the fluid flow and vice-versa.

| (a) Adiabatic | (b) Conjugate (Stainless Steel) |
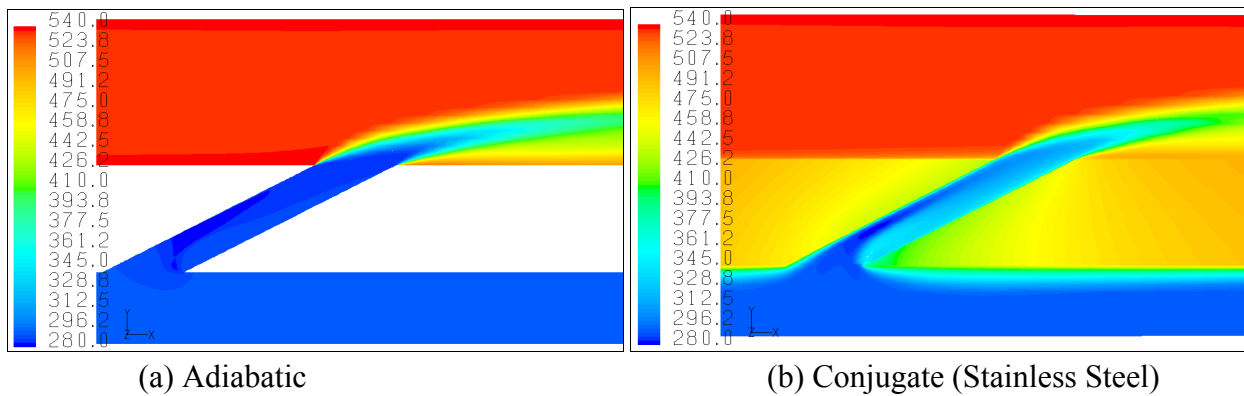
Figure 4.12. Temperature magnitude contours $(Kelvin)$ along centerline plane in the film cooling hole region.

| (a) Adiabatic | (b) Conjugate (Stainless Steel) |
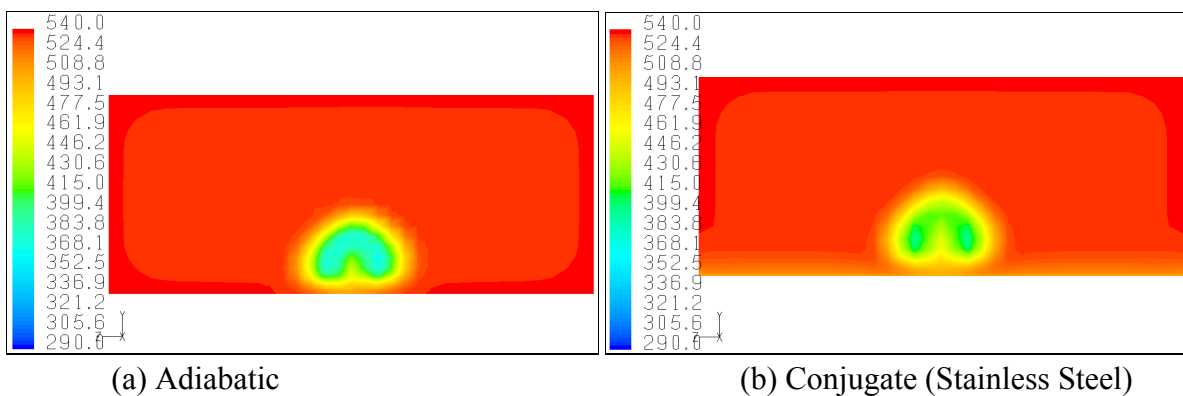
Figure 4.13. Comparison of predicted temperature contours $(Kelvin)$ at plane $(x/D = 5)$ using the RKE turbulence model.

(a) Adiabatic   (b) Conjugate (Stainless Steel)
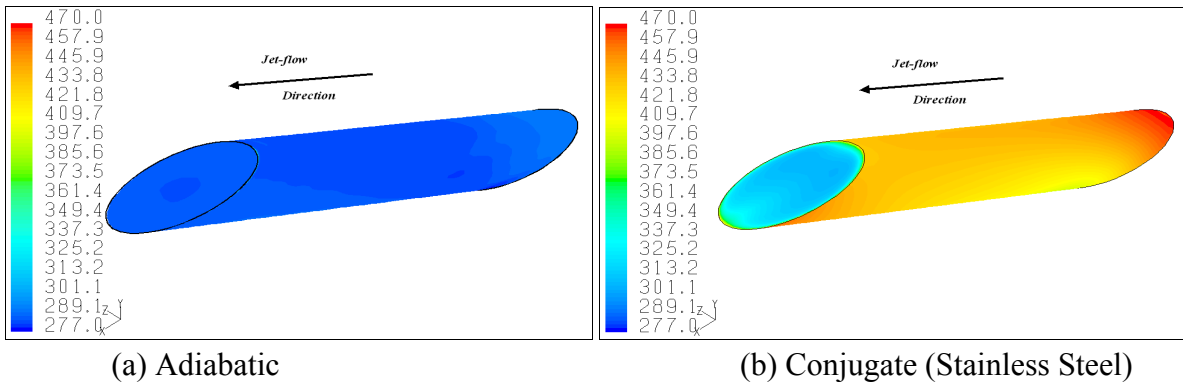
Figure 4.14. Comparison of predicted surface temperature contours ($Kelvin$) along film cooling hole using the RKE turbulence model.

(a) Adiabatic   (b) Conjugate (TECAPEK)

(c) Conjugate (Stainless Steel)
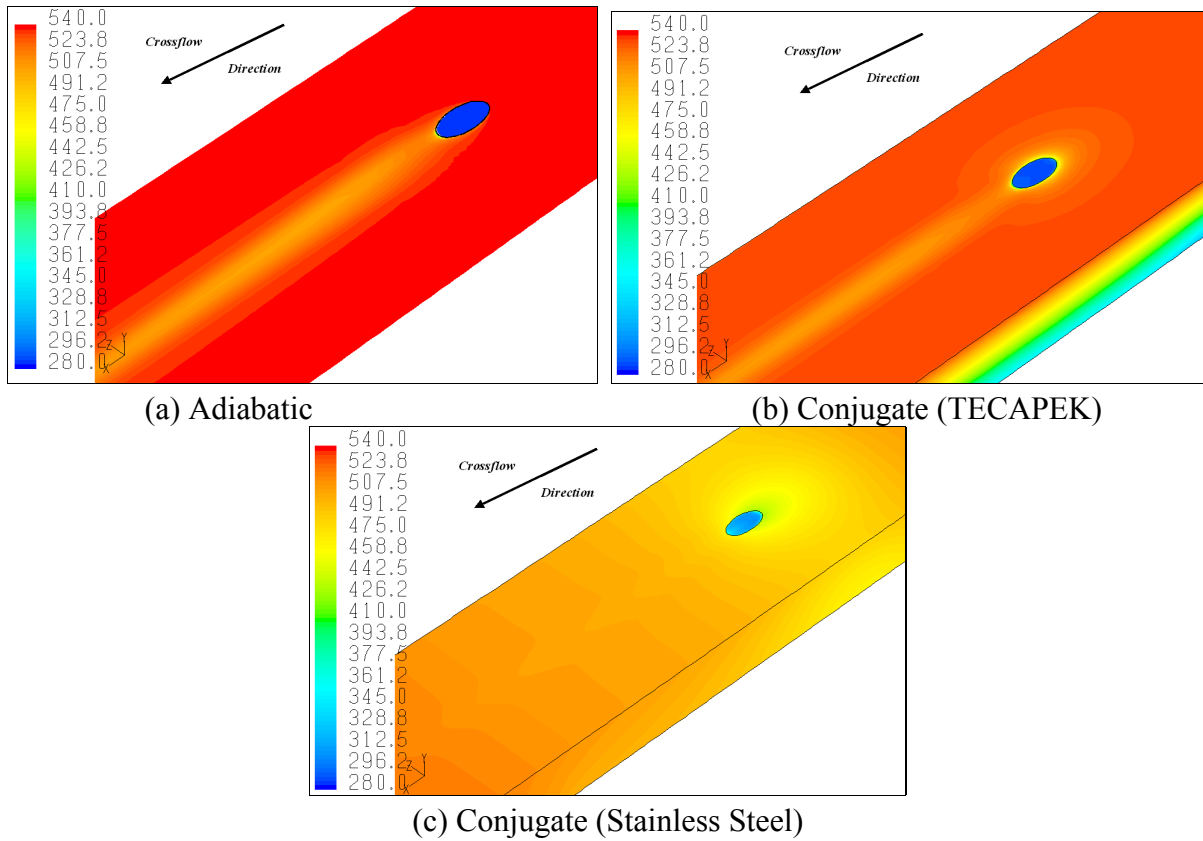
Figure 4.15. Comparison of predicted surface temperature contours ($Kelvin$) along the endwall in the film cooling hole region using the RKE turbulence model.

In this chapter, a comparative study is presented which indicates the ability of different turbulence models to predict the film cooling effectiveness from a cylindrical cooling holes. The

standard k-ϵ model, the RNG k-ϵ model, the realizable k-ϵ model, the standard k-ω model, and also the SST k-ω models have been investigated. The boundary conditions were chosen in a way to be more representative for typical gas turbine applications. The flow and temperature fields were discussed, in addition to local, two-dimensional distribution of film cooling effectiveness for the adiabatic and conjugate cases. Results are compared to experimental data in terms of centerline film cooling effectiveness downstream of the cooling hole. For such applications, it is very important to ascertain the grid dependence of the solutions, and to have a high quality hexahedral gird for accurate results. It is shown that in the region for ($x/D \leq 6$), the predictions of centerline effectiveness by the RKE turbulence model exhibits the best agreement with experimental data. Whereas, the other four models underpredict the film cooling effectiveness, whereas, in the region for ($x/D > 6$), all models overpredicted the centerline film cooling effectiveness, and the best agreement was predicted by the SKE turbulence model. Again, the results confirm that the conjugate heat transfer model shows a significant difference in the temperature predictions in comparison with the adiabatic model cases. Also, results show the effect of the conjugate heat transfer on the temperature field in the film cooling hole region, and the additional heating up of the cooling jet itself.

In gas turbine engines, it is very important to achieve a high overall performance by cooling the blades/vanes effectively. In an attempt to improve the cooling process, the gas turbine designers considered the idea of shaping the cooling holes. Film cooling holes with a diffuser-shaped expansion at the exit portion of the hole are believed to improve the film cooling performance. The increased cross-sectional area at the hole exit compared to a cylindrical hole leads to a reduction of the mean velocity and, thus, of the momentum flux of the jet exiting the hole. Therefore, the penetration of the jet into the mainflow is reduced, resulting in an increased cooling efficiency [34]. Based on this, the work done for the case of cylindrical holes will be extended to fan-shaped cooling holes, which will be discussed in more details in the next chapter.

CHAPTER 5

CONJUGATE HEAT TRANSFER SIMULATION OF FAN-SHAPED FILM COOLING HOLES

5.1 Introduction

It is well known that significant improvement can be achieved of better cooling characteristics of the film by using cooling holes with expanded exits. Film cooling holes with a diffuser-shaped expansion at the exit portion of the hole are believed to improve the film cooling performance, because the increased cross-sectional area at the hole exit compared to a cylindrical hole leads to a reduction of the mean velocity and, thus, of the momentum flux of the jet exiting the hole. Therefore, the penetration of the jet into the mainflow is reduced, resulting in an increased cooling efficiency [20,34]. Based on this, the systematic computational methodology applied to cylindrical cooling holes will be extended and applied to fan-shaped cooling holes.

In this chapter, the film cooling effectiveness for adiabatic and conjugate heat transfer models from a 3D fan-shaped cooling holes will be predicted, and the simulated results will be compared to experimental data available in the open literature. An important issue that will be considered is the grid topology, since it is a fan-shaped hole, it requires a big effort to generate a high quality hexahedral mesh. For this reason, the effect of grid topology; i.e. hexahedral-, hybrid-, and tetrahedral-topology meshes on the predicted film cooling effectiveness will be studied in more detail. The present CHT models will investigate the prediction of film cooling effectiveness from single, scaled-up fan-shaped hole geometry at an injection angle of 30°. The flow conditions considered are a blowing ratio of one, and the coolant-to-mainflow temperature ratio of 0.54. Turbulence closure was obtained using three different turbulence models: the realizable k-ϵ model (RKE), the shear stress transport k-ω model (SST) as well as the $v^2 - f$

model (V2F). Also, the velocity and temperature fields, in addition to centerline and two-dimensional film cooling effectiveness, will be presented. Finally, The predicted centerline film cooling effectiveness will be compared to experimental data reported by Gritsch et al. [34].

5.2 Validation Test Case: Fan-Shaped Cooling Hole

The same experiment used in the previous chapter will also be considered here for the case of fan-shaped cooling hole, see Figure 5.1. This experiment was discussed in more detail previous chapter. For more information read section 4.2.

(a)

(b)
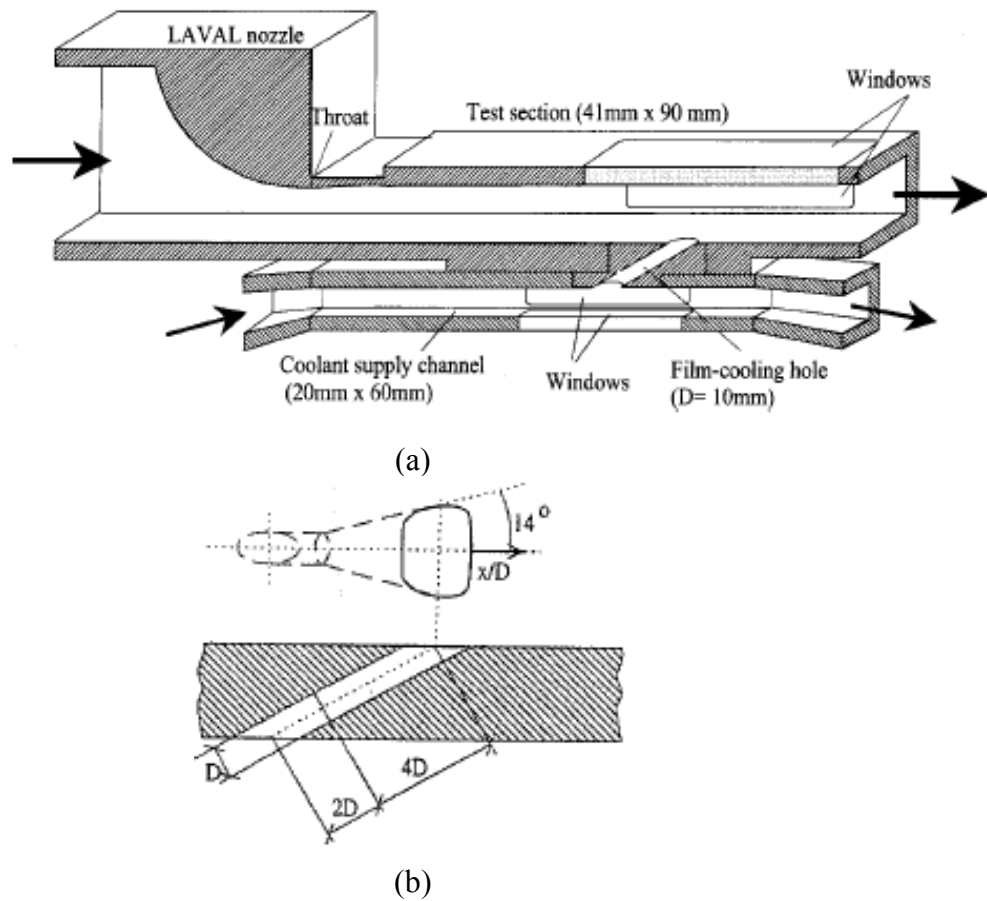
Figure 5.1. Geometry of the experimental test case used in this study: (a) overall setup; (b) fan-shaped cooling hole details from Gritsch et al. [34].

5.3 Numerical Method

Again, a systematic computational methodology is adopted and extended to fan-shaped cooling holes. This methodology consists of a computational model or geometry, high quality grid, boundary conditions, effective turbulence modeling, and solver.

5.3.1 Geometry

The computational domain for the adiabatic cases matched the experimental test case. The solid models of the whole assembly are shown in Figure 5.2. For the adiabatic cases, the computational domain included the coolant supply channel (plenum), the fan-shaped cooling hole, and the main channel (cross hot flow), the crossflow test section was 90 mm in width and 41 mm in height, and plenum cross-section was 60 mm in width and 20 mm in height. The diameter of the film hole was 10 mm with an injection angle of 30°, the metering section is $2D$ long, the lateral expansion is 14° resulting in a hole width of 30 mm at the hole exit, and the exit-to-entry area ratio is 3.0 (areas perpendicular to hole axis). The exit plane for the crossflow was located far downstream of the cooling hole; i.e. $x/D = 30$. The conjugate model was the same as the adiabatic model, but it had an endwall with a cross-sectional area of 90 mm in width and 30 mm in height. Moreover, the width of the plenum had been adjusted from 60 mm to 90 mm. The geometry was generated using Gambit 2.1.2 from Fluent, Inc.
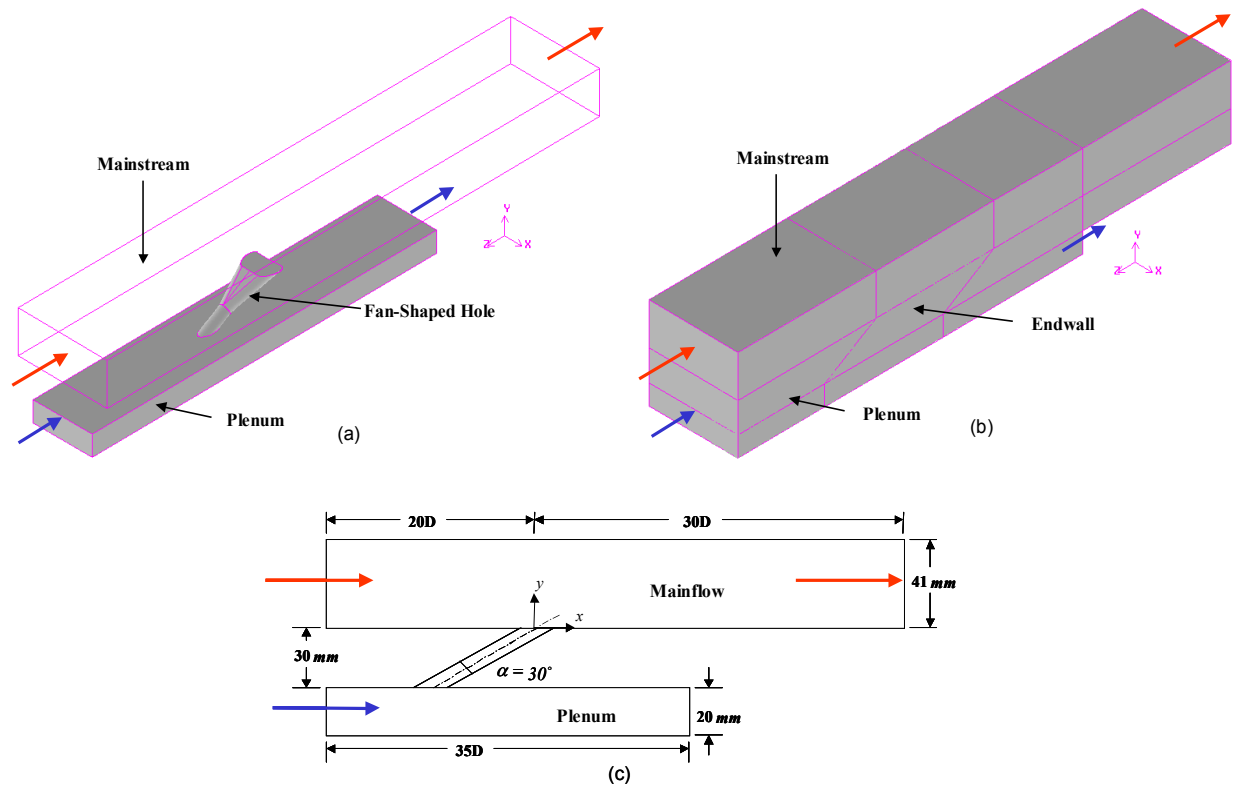
Figure 5.2. Computational domain; (a) solid model of the adiabatic cases, (b) solid model of the conjugate case, and (c) schematic diagram.

5.3.2 Grid

A multi-block numerical grid was used in the present work to allow the highest quality in all regions with the fewest number of cells. Again, multi-blocking refers to a technique in which the domain is partitioned into several different subsections in order to achieve the maximum control over the grid quality and density. Each section was then meshed using an appropriate topology. For the above reason, the model was partitioned into 11 blocks for the adiabatic cases, and 20 blocks for the conjugate case. This allowed the use of a hexahedral mesh in all the blocks to achieve a high aspect ratio especially near the walls. The total number of computational cells is 1,867,168 for the adiabatic cases, and 2,375,139 for the conjugate case. The grid was created in Gambit from Fluent, Inc. The cells in the near-wall layers were stretched away from the

surfaces, and the first mesh point above the end wall is chosen such that the average y^+ is of the order of unity or less. A view of the computation grid for the adiabatic and conjugate cases is shown in Figures 5.3 and 5.4, respectively. Since it takes a big effort (five blocks) to mesh the fan-shaped hole with a hexahedral-topology grid, this study is also concerned with different meshing schemes. For this reason, the fan-shaped hole has been meshed using a hybrid-topology grid and a tetrahedral topology grid. The hybrid grid consists of both prisms near the walls and tetrahedral cells; the total number of cells is 1,871,508. Whereas, the tetrahedral-topology grid consists only of tetrahedral cells with a total number of 1,476,141 cells, see Figure 5.5.

| (a) | (b) |
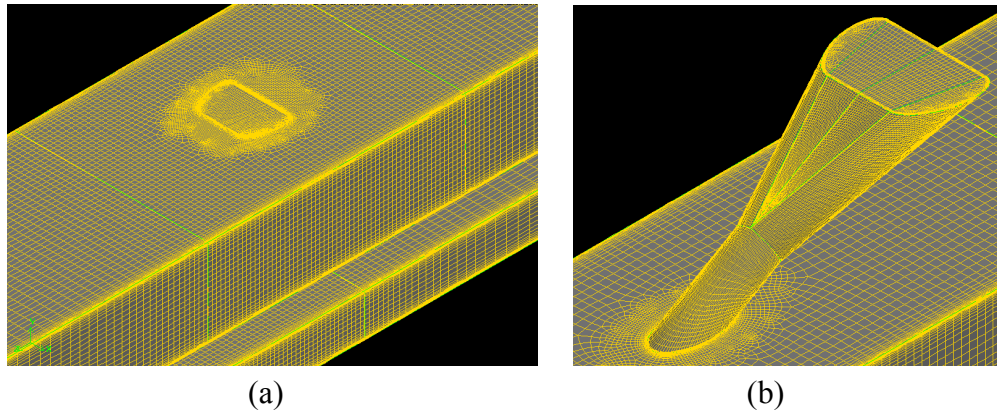
Figure 5.3. Details of the grid used in the adiabatic case: (a) whole domain; (b) mesh for the film-cooling hole region.

| (a) | (b) |
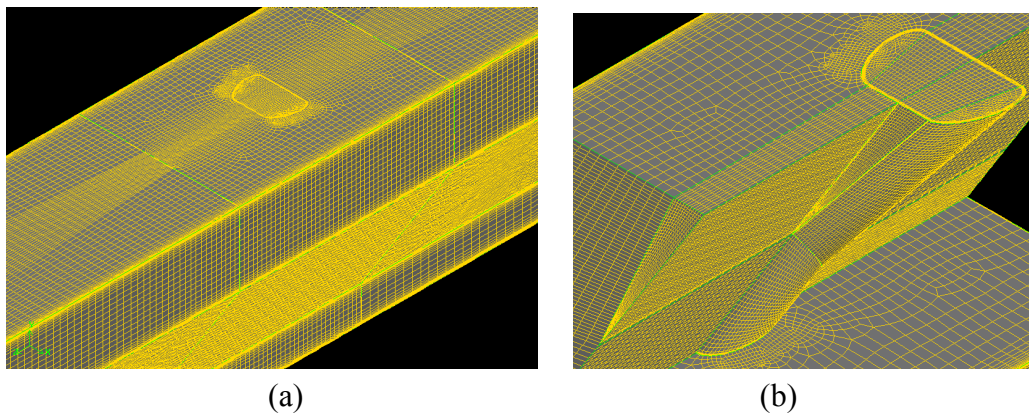
Figure 5.4. Details of the grid used in the conjugate case: (a) whole domain; (b) mesh for the film-cooling hole region with the endwall.

| (a) Hexahedral Mesh | (b) Hybrid Mesh | (c) Tetrahedral Mesh |
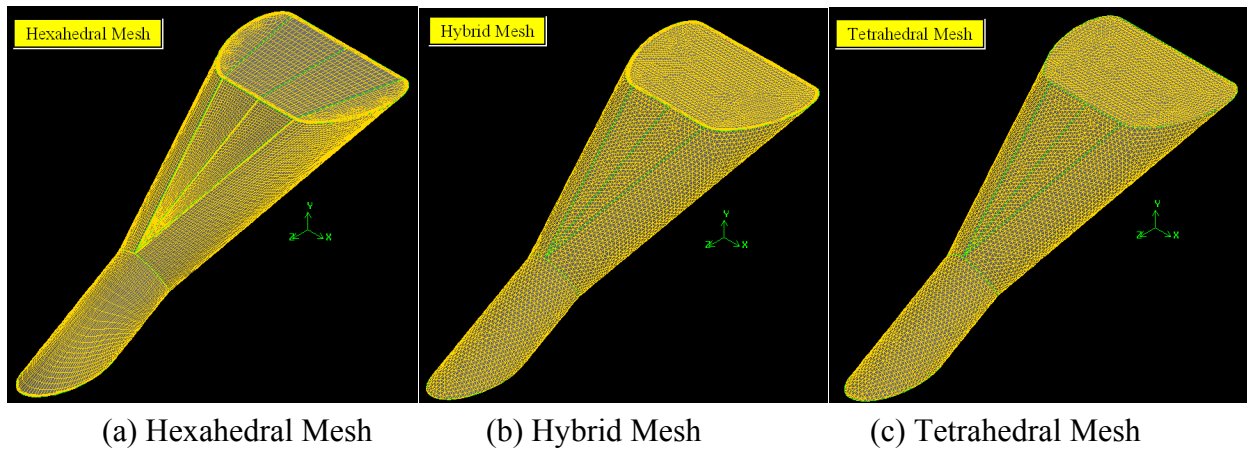
Figure 5.5. Mesh details for the hexahedral-, hybrid-, and tetrahedral-topology grid in the cooling hole region.

5.3.3 Boundary Conditions

The boundary conditions were chosen to match the experimental test case as closely as possible. The total pressure and total temperature are imposed at the channels inlet, static pressure at the outlets. The total temperature at the primary (crossflow) channel inlet is $540K$, and $290K$ in the secondary (plenum) channel inlet. Thus the coolant-to-mainflow temperature ratio is 0.54, which can be assumed to be more representative for typical gas turbine applications. To achieve a blowing ratio of 1.0, the total pressure in the plenum was set to $109750Pa$, whereas, the total pressure at the mainflow inlet is $100400Pa$, and the static pressure at the outlet is $68000Pa$. Inlet turbulence levels are set to 1.5% and 1% in the primary and secondary channels, respectively.

The fluid, air, was modeled as a compressible flow using ideal gas law, whereas, the other properties of air; i.e. specific heat ratio, thermal conductivity, and dynamic viscosity are piecewise-linear functions of temperature. For the conjugate heat transfer model, the endwall material was modeled as a high-temperature plastic material (TECAPEK) with a thermal conductivity of $(0.2\,W/mK)$ for one case, and the other case was AISI 347 stainless steel, with

a density of $(7978 kg/m^3)$, and the thermal conductivity is piecewise-linear function of temperature.

5.3.4 Turbulence Modeling

To investigate the effect of turbulence modeling on film cooling effectiveness, turbulence closure was obtained using three different turbulence models; the realizable k-ϵ model (RKE) of Shih [121] which resulted in a good agreement with the experimental data as shown for the case of cylindrical hole, the SST k-ω model (SST) of Menter [123], and $v^2 - f$ model (V2F) of Durbin [129]. The two-equation approach to turbulence modeling for film cooling problems is considered a "standard" due to ease of implementation and computational economy. The impact of each of the three turbulence models on the prediction of film cooling effectiveness is compared to experimental data [34] in the results section below.

Briefly, the RKE model satisfies the so-called realizability constraints for the Reynolds stresses, specifically requiring positivity of the Reynolds stresses and satisfaction of Schwarz's inequality for the shear stresses. The RKE model has been shown by several researchers to reduce the excessive and non-physical production of turbulent kinetic energy characteristic of the standard k-ϵ model in areas of high irrotational strain. The SST model differs from the standard k-ω model in two ways. First the gradual change from the standard k-ω model in the inner region of the boundary layer to a high-Reynolds number version of the k-ϵ model in the outer part of the boundary layer. Second the modified turbulent viscosity formulation to account for the transport effects of the principal turbulent shear stress. Finally, the V2F model is an alternative to eddy-viscosity models and Reynolds Stress Model. This model is similar to the standard k-ϵ model, but incorporates the near-wall turbulence anisotropy and non-local pressure-strain effects. In fact, it is a general low Reynolds-number turbulence model that is valid all the way up to solid walls, and therefore does not need to make use of wall functions. Although the

model was originally developed for attached or mildly separated boundary layers, it also accurately simulates flows dominated by separation.

The V2F model is a four-equation model based on transport equations for the turbulence kinetic energy (k), its dissipation rate (ϵ), a velocity variance scale $(\overline{v^2})$, and an elliptic relaxation function (f). The distinguishing function of the $v^2 - f$ model is its use of the velocity scale $(\overline{v^2})$ instead of the turbulent kinetic energy (k) for evaluating the eddy viscosity (ϵ). The velocity variance scale $(\overline{v^2})$ which can be thought of as the velocity fluctuation normal to the streamlines, has shown to provide the right scaling in representing the damping of turbulent transport close to the wall, a feature that k does not provide. The turbulent kinetic energy (k), its dissipation rate (ϵ), the velocity variance scale $(\overline{v^2})$, and the elliptic relaxation function (f), are obtained from the following transport equations:

$$\frac{\partial}{\partial t}(\rho k) + \frac{\partial}{\partial x_i}(\rho k u_i) = P - \rho\epsilon + \frac{\partial}{\partial x_j}\left[\left(\mu + \frac{\mu_t}{\sigma_k}\right)\right] + S_k \tag{5.1}$$

$$\frac{\partial}{\partial t}(\rho\epsilon) + \frac{\partial}{\partial x_i}(\rho\epsilon u_i) = \frac{C'_{\epsilon 1}P - C_{\epsilon 2}\rho\epsilon}{T} - \rho\epsilon + \frac{\partial}{\partial x_j}\left[\left(\mu + \frac{\mu_t}{\sigma_k}\right)\frac{\partial\epsilon}{\partial x_j}\right] + S\epsilon \tag{5.2}$$

$$\frac{\partial}{\partial t}(\rho\overline{v^2}) + \frac{\partial}{\partial x_i}(\rho\overline{v^2}u_i) = \rho k f - 6\rho\overline{v^2}\frac{\epsilon}{k} + \frac{\partial}{\partial x_j}\left[\left(\mu + \frac{\mu_t}{\sigma_k}\right)\frac{\partial\overline{v^2}}{\partial x_j}\right] + S_{\overline{v^2}} \tag{5.3}$$

$$f - L^2\frac{\partial^2 f}{\partial x_j^2} = (C_1 - 1)\frac{\frac{2}{3} - \overline{v^2}/k}{T} + C_2\frac{P}{\rho k} + \frac{5\overline{v^2}/k}{T} + S_f \tag{5.4}$$

where

$$P = 2\mu_t S^2, \ S^2 \equiv S_{ij}S_{ij}, \ S_{ij} = \frac{1}{2}\left(\frac{\partial u_i}{\partial x_j} + \frac{\partial u_j}{\partial x_j}\right) \tag{5.5}$$

The turbulent time scale (T), length scale (L), and the other constants are defined in [129-131]. Here, the $v^2 - f$ model uses an elliptic operator to compute a term analogous to the pressure strain correlation of the RSM. Ellipticity is characterized by a modified Helmholtz operator, which introduces wall effects via a linear differential equation.

5.3.5 Film Cooling Effectiveness

The local film cooling effectiveness (η) for the fan-shpaed hole is defined in the same way as it was defined for the case of a cylindrical hole, i.e.

$$\eta(x/D, z/D) = \frac{T(x/D, z/D) - T_{r,m}}{T_{tc} - T_{r,m}} \tag{4.1}$$

where, $T(x/D, z/D)$ is the local temperature, and it is the adiabatic temperature for the adiabatic cases $T_{AW}(x/D, z/D)$, or the conjugate temperature for the conjugate case, $T_{Conj}(x/D, z/D)$. T_{tc} is the mass-weighted average temperature of the coolant at the exit of the cooling hole, and $T_{r,m}$ is the recovery temperature of the mainflow. In the experiment [34], the mainflow recovery temperature was measured on the test plate at a location not affected by the coolant ejection, for this reason, the recovery temperature was calculated at a location of $(x/D = -5)$.

5.3.6 Solver

Again, the simulations were processed using Fluent version 6.1.22 software from Fluent, Inc. Convergence was determined with the following strict criteria: 1) reduction of all residuals of at least four orders of magnitude, and were no longer changing; 2) global mass and energy imbalances dropped below 0.001%; and 3) the flow field was unchanging, and the endwall

surface temperature did not vary with additional iterations, and thus a "steady state" had been achieved.

5.4 Results and Discussion

This simulation was primarily concerned with the computational prediction of adiabatic and conjugate effectiveness downstream of a 3D fan-shaped film cooling hole. Results were obtained for $L/D = 6.0$, blowing ratio of 1.0, and coolant-to-mainflow temperature ratio of 0.54. First, the results will discuss the adiabatic model cases with three different turbulence models and three grid topology schemes, then, the conjugate model cases predicted by the RKE turbulence model.

5.4.1 Velocity Field Results

Since the thermal field of a jet-in-crossflow interaction is dictated by the hydrodynamics, the flow field results were predicted by three turbulence models using a hexahedral mesh, also, the flow field results were predicted for a three topology-grid; i.e. hexahedral-, hybrid-, and tetrahedral-grids using the RKE turbulence model. The computed near-field velocity contours (m/sec) along the centerline plane $(z = 0)$ are shown in Figure 5.6, where the turbulence closure was simulated using the three turbulence models. As it can be seen that all models predicted the low momentum region along the downstream edge and the corresponding high momentum or jetting region along the upstream edge within the film-cooling hole. Also, it can be seen that the flow distribution is quite different from one turbulence model to next. This result is clearer in Figure 5.7: V2F predicts a maximum velocity of 228 m/sec, whereas, RKE model predicts the maximum velocity to be 171 m/sec. Moreover, the flow field predicted by the V2F is significantly different from the one predict by RKE or SST, the flow distribution predicted by

59

SST model looks quite similar to the one predicted by RKE model especially at the film hole exit plane. Figures 5.8 and 5.9 show the velocity contours along the centerline plane in the film cooling hole region and at the cooling hole exit plane. Here, the results were predicted by the RKE turbulence model for the three topology grid; the hexahedral grid, the hybrid grid which was created from prisms near the walls and tetrahedral cells away from the walls, and tetrahedral grid. It can be seen that the flow field predicted for the case of a hybrid mesh is very similar to the case of a hexahedral mesh, whereas the tetrahedral case is very similar to the other cases in the flow core and quite different near the walls, which tells us the need for creating a boundary layer near the walls to be able to capture the high gradients of the flow field.

(a) RKE   (b) SST

(c) V2F
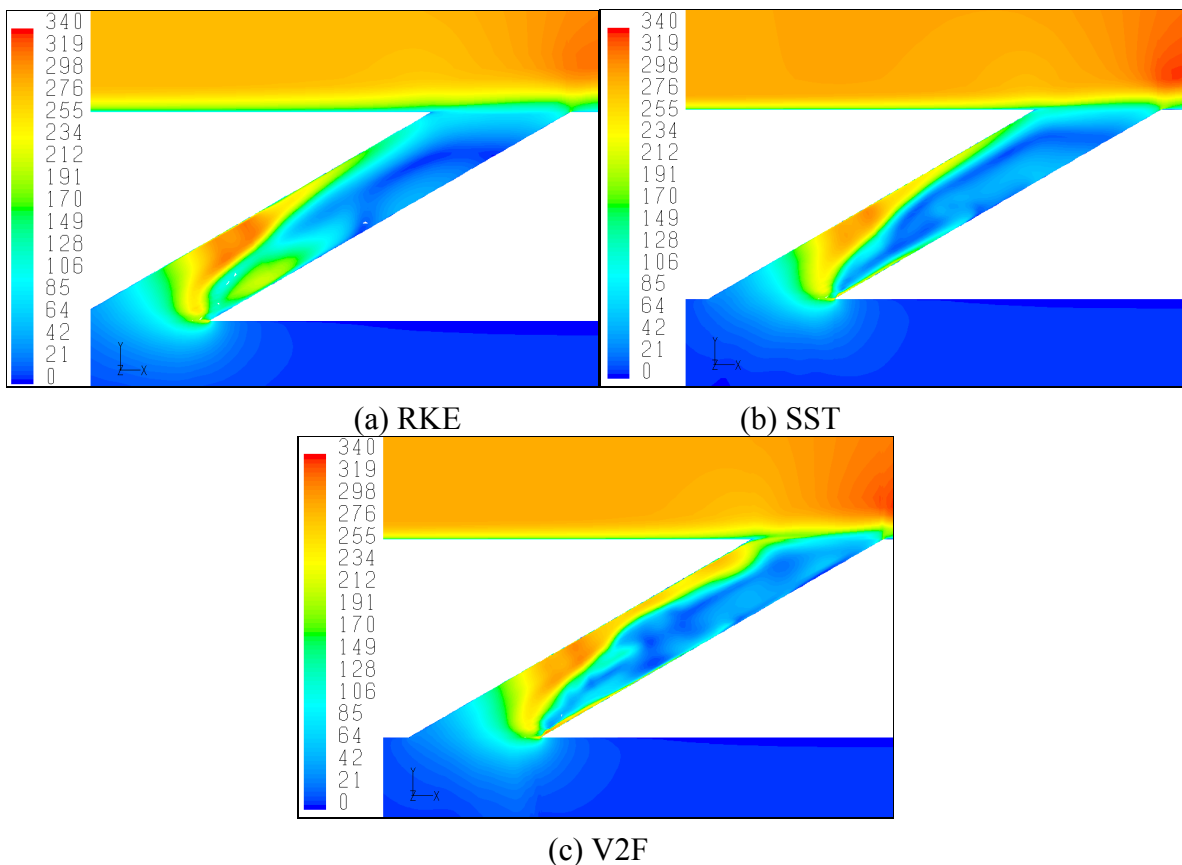
Figure 5.6. Velocity magnitude contours (m/sec) predicted by three turbulence models along centerline plane in the film cooling hole region with a hexahedral-topology grid.

(a) RKE   (b) SST   (c) V2F
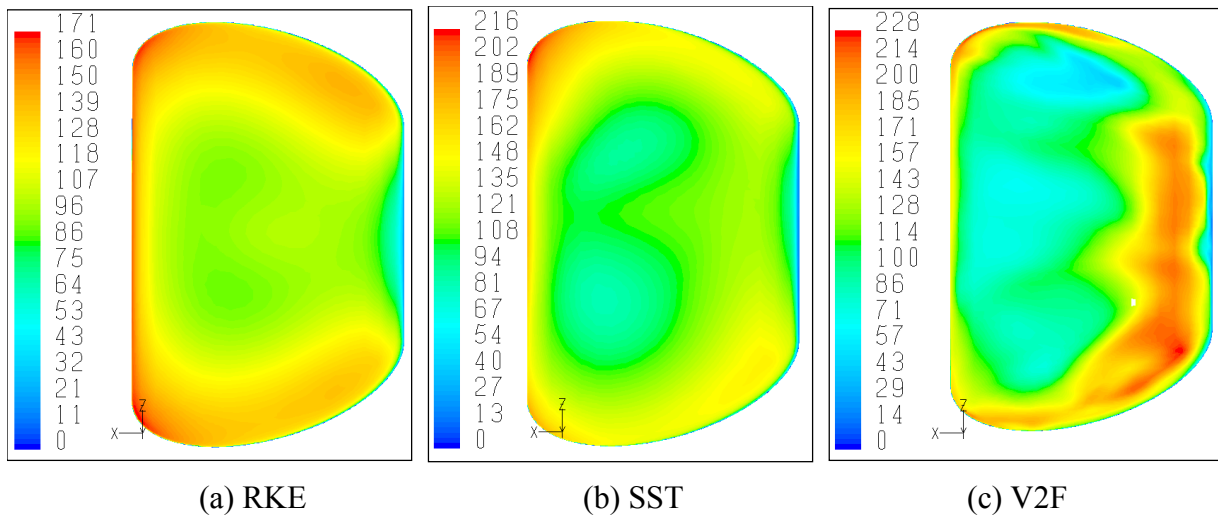
Figure 5.7. Velocity magnitude contours (m/sec) predicted by three turbulence models in the film hole exit plane with a hexahedral-topology grid.

(a) Hexahedral Mesh   (b) Hybrid Mesh

(c) Tetrahedral Mesh
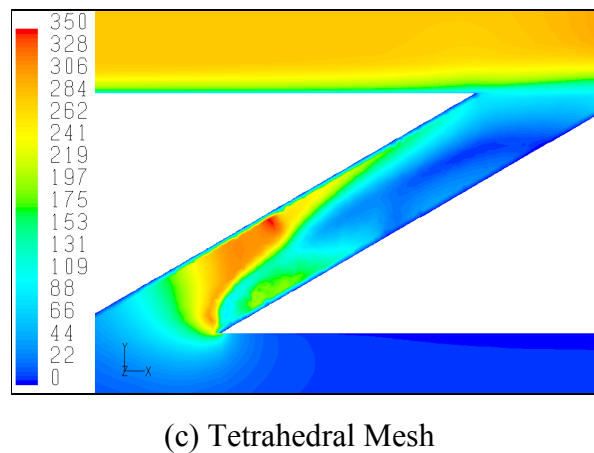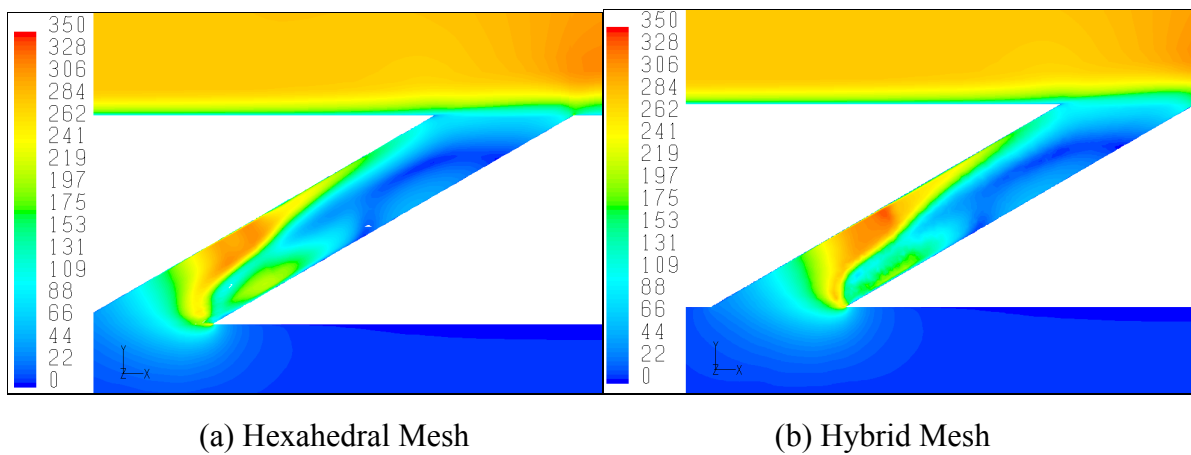
Figure 5.8. Velocity magnitude contours (m/sec) predicted by the RKE turbulence model along centerline plane in the film cooling hole region using three topology-grids.
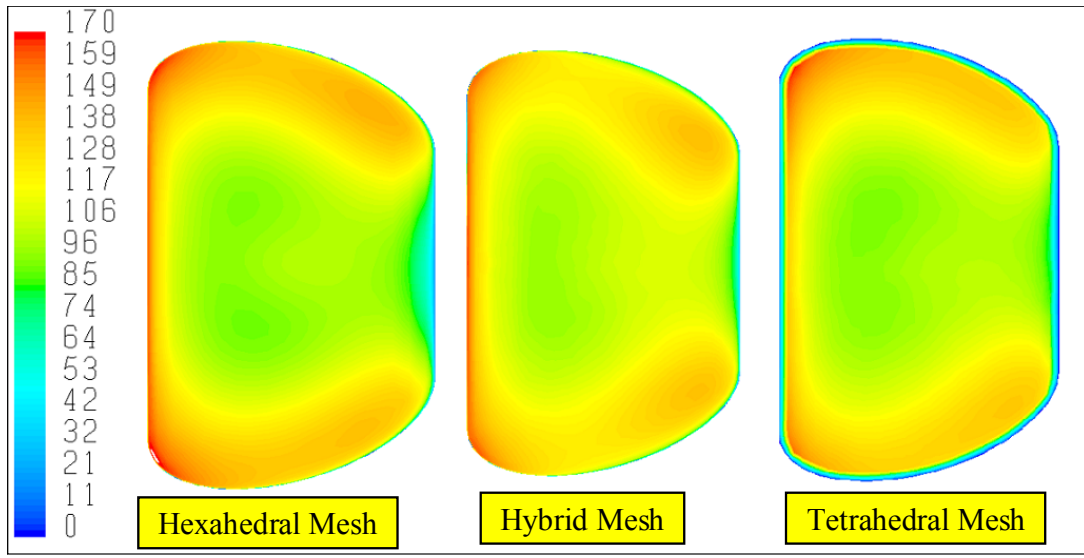
Figure 5.9. Velocity magnitude contours (m/sec) predicted by the RKE turbulence model in the film hole exit plane using three topology-grids.

5.4.2 Film Cooling Effectiveness Results

In this section, the local centerline and two-dimensional distribution of the film cooling effectiveness for the adiabatic and conjugate cases are reported. Note that the streamwise distances are measured from the trailing edge $(x/D = 0)$ of the film hole at the exit plane. Figure 5.10 shows a comparison of computed centerline effectiveness with the data of Gritsch et al. [34] for the three turbulence models with a hexahedral mesh. The blowing ratio for those cases is very close to one. It can be seen that all models overpredict the experimental data in the near hole region; i.e. $(x/D \leq 2)$, whereas, RKE model and SST model predictions are very close to each other in this case (fan-shaped hole). On average, the predictions of RKE and SST models are very close to the experimental data. Surprisingly, the predictions of the V2F model are very different from the experimental data and the predictions of the other two models. The V2F model overpredicts the experimental data by up to 17% in the cooling hole immediate region $(x/D \leq 4)$, and underpredicts the results by up to 27% in the intermediate region

$(x/D > 4)$. Overall, the RKE and SST models give better agreement with experimental data when compared to the V2F model. Figure 5.11 shows the predicted film cooling effectiveness by the RKE model for three topology grids. It can be seen that the film effectiveness predicted with a hexahedral mesh is very similar to the case of a hybrid mesh, whereas, the results predicted with a tetrahedral mesh is higher than the other two cases. An interesting result is that the predicted film effectiveness with a tetrahedral mesh is in a better agreement with experimental data, especially in the region of $(3 < x/D < 6)$.

Figure 5.12 shows the two-dimensional distribution of the local film cooling effectiveness for the three adiabatic cases, as well as the conjugate case predicted by the RKE turbulence model. Qualitatively, all turbulence models tend to agree with the experiment [34], whereas, the distribution of the film cooling effectiveness for the conjugate case is significantly different. The centerline effectiveness for the adiabatic and conjugate cases compared to the experiment is shown in Figure 5.13. The predicted film effectiveness using the conjugate model is in a better agreement with the experimental data compared to the film effectiveness with the adiabatic model. This finding might be attributed to the fact that the experimental data has some conduction effects especially for this case; i.e. fan-shaped hole.
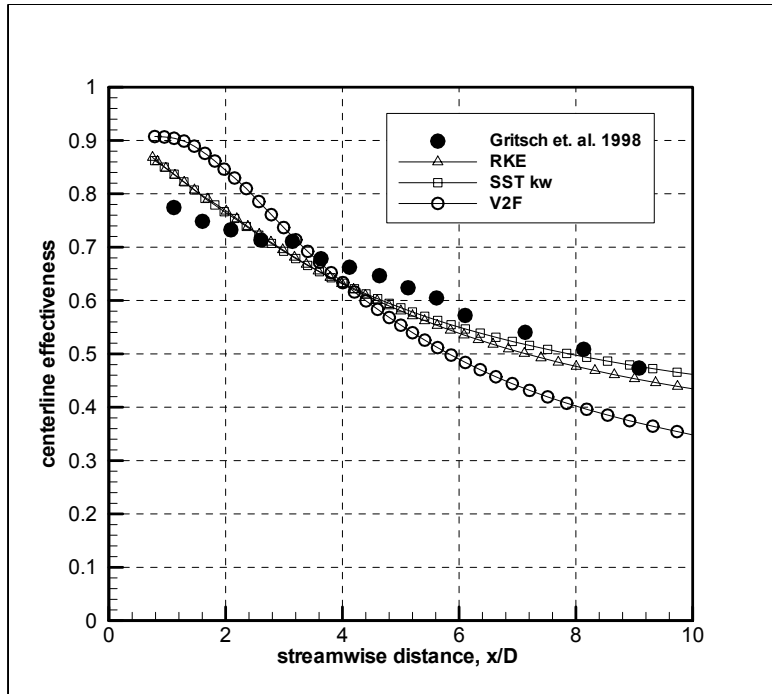
Figure 5.10. Comparison of computed centerline adiabatic effectiveness (η) with data of Gritsch et al. [34] predicted by three turbulence models with a hexahedral-topology grid.
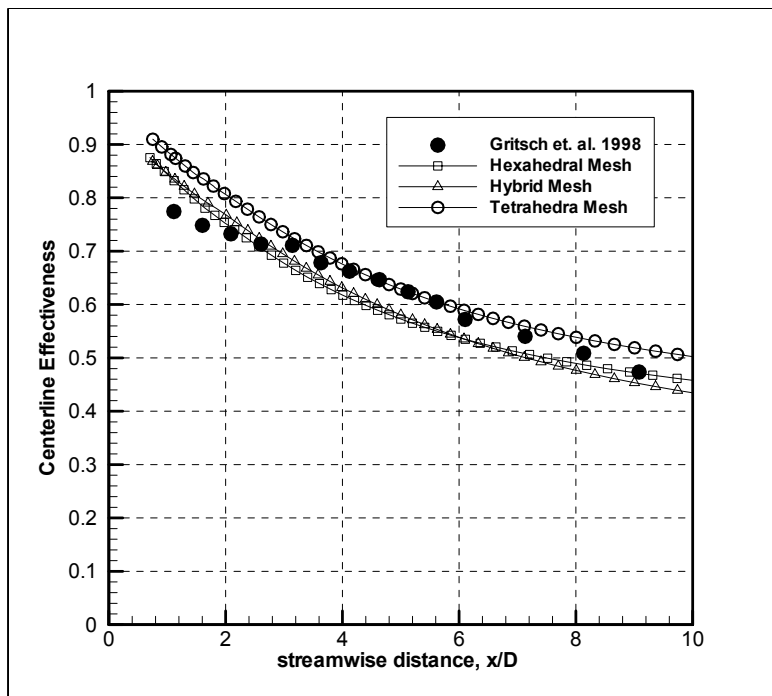
Figure 5.11. Comparison of computed centerline adiabatic effectiveness (η) with data of Gritsch et al. [34] predicted by the RKE turbulence model using three topology-grids.

(a) RKE   (b) SST

(c) V2F   (d) Conj.
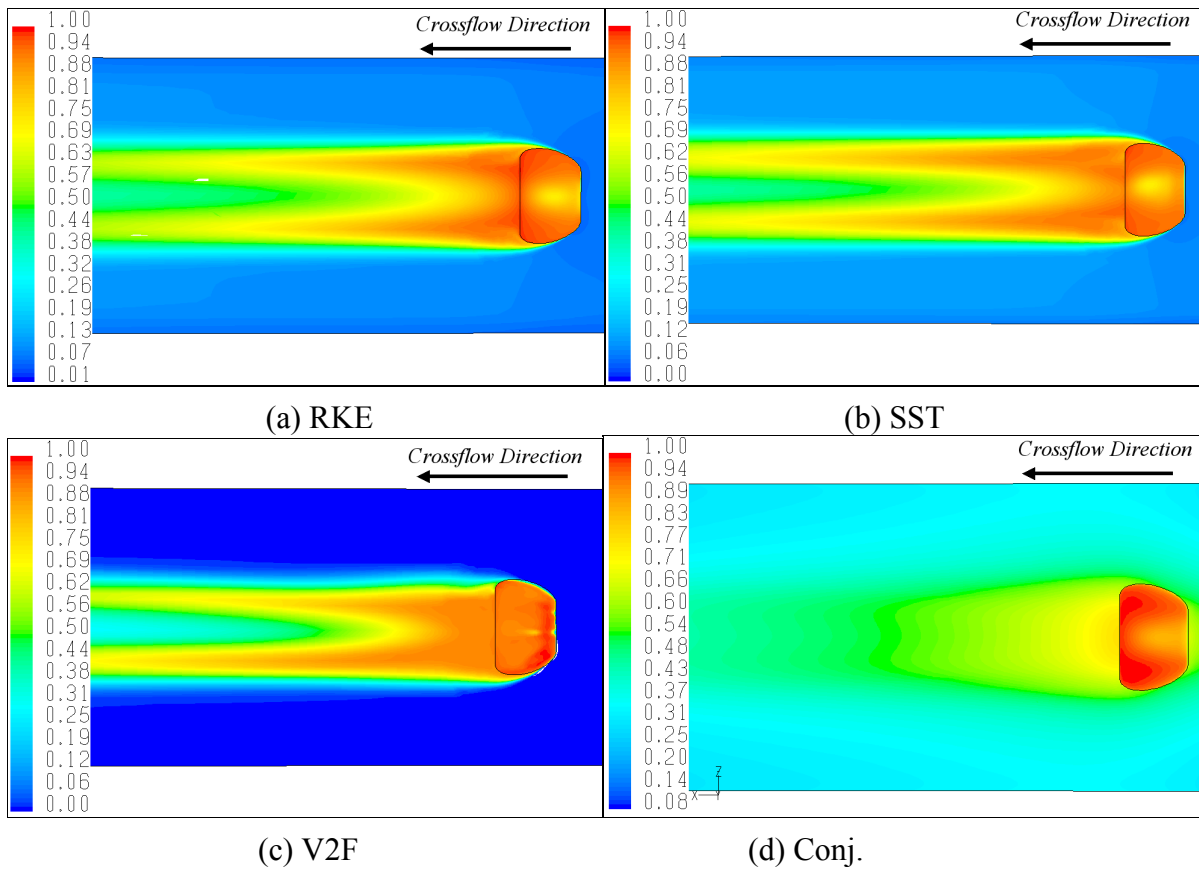
Figure 5.12. Local adiabatic and conjugate effectiveness (η) predicted by three turbulence levels.
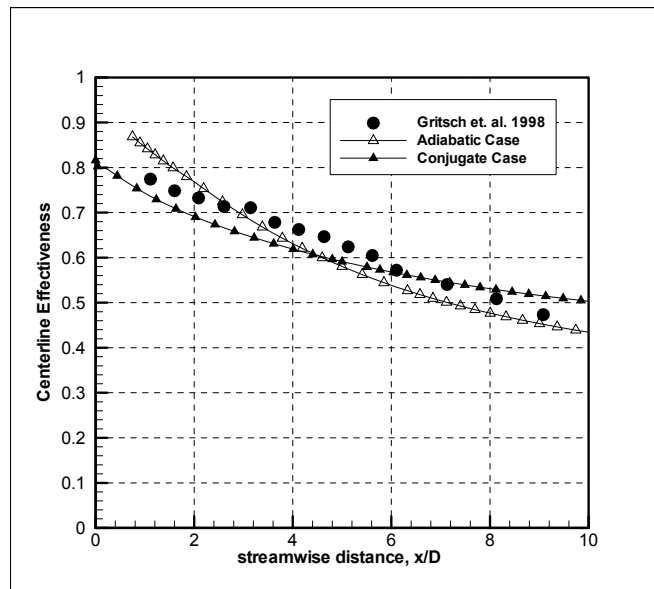
Figure 5.13. Comparison of centerline adiabatic and conjugate effectiveness (η) with data of Gritsch et al. [34] predicted by the RKE turbulence model with a hexahedral-topology grid.

5.4.3 Temperature Field Results

This section presents the temperature distribution in Kelvin for the cases of adiabatic and conjugate heat transfer models. Since the RKE turbulence model gave good agreement with experimental data as shown in the film cooling effectiveness section, it had been used to predict the adiabatic and conjugate cases results. Figure 5.14 shows the computed near hole centerline temperature contours for the adiabatic and conjugate cases, respectively. For the conjugate case, heat fluxes from the hot main flow into the wall lead to heating up the of the solid body. At the film cooling hole, an additional temperature increase of the cooling jet in comparison to the adiabatic case occurs because of the heat transfer from the hot wall into the cooling jet, see Figure 5.15. An isometric view of temperature contours along the endwall and close to the cooling hole region is presented in Figure 5.16 for the adiabatic and two conjugate cases, respectively. The conjugate cases were one with very low thermal conductivity $(0.2W/m.K)$. This corresponds to a high temperature plastic material (TECAPEK) endwall material, and the other conjugate case was for a stainless steel endwall material. In this case, the fan-shaped hole, the results predicted from the adiabatic case is very similar to the results predicted by conjugate case with TECAPEK endwall material, whereas it is not the case for the cylindrical film cooling hole. These figures show clearly the differences in the temperature contours for both cases, which confirm that the conjugate heat transfer model can take into account the mutual influences of heat transfer on the fluid flow and vice versa.
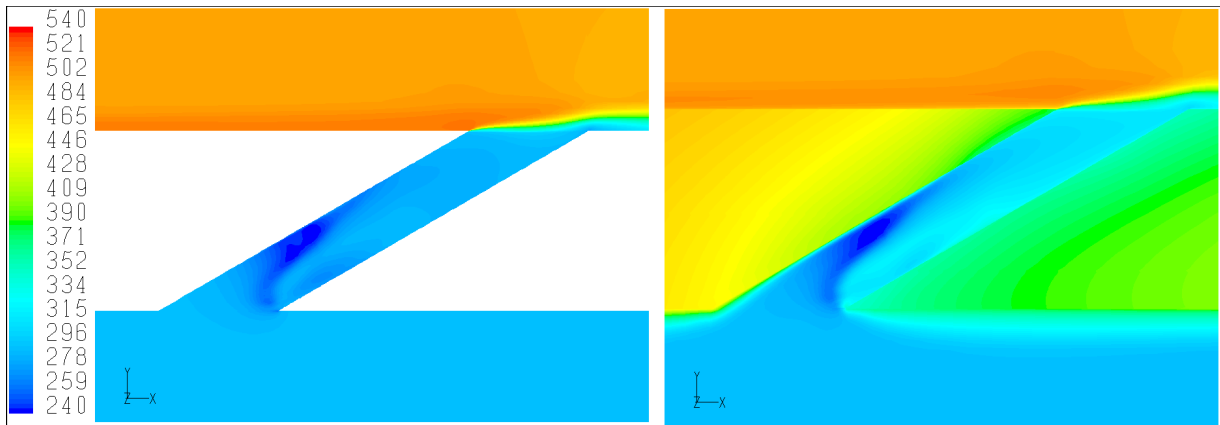
(a) Adiabatic   (b) Conjugate (Stainless Steel)

Figure 5.14. Temperature magnitude contours ($Kelvin$) along centerline plane in the film cooling hole region predicted by the RKE turbulence model with a hexahedral mesh.
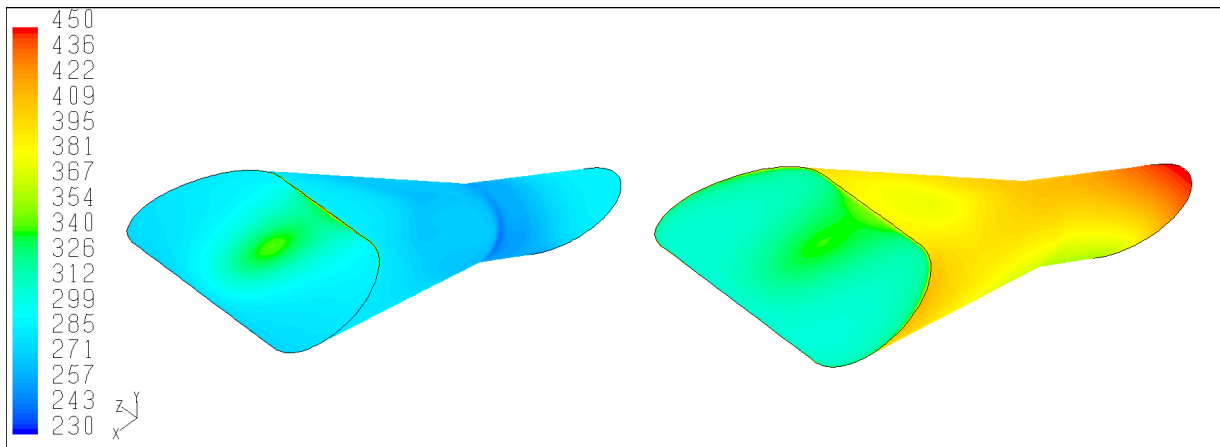
(a) Adiabatic   (b) Conjugate (Stainless Steel)

Figure 5.15. Comparison of predicted surface temperature contours ($Kelvin$) along film cooling hole predicted by the RKE turbulence model with a hexahedral mesh.

(a) Adiabatic   (b) Conjugate (TECAPEK)

(c) Conjugate (Stainless Steel)
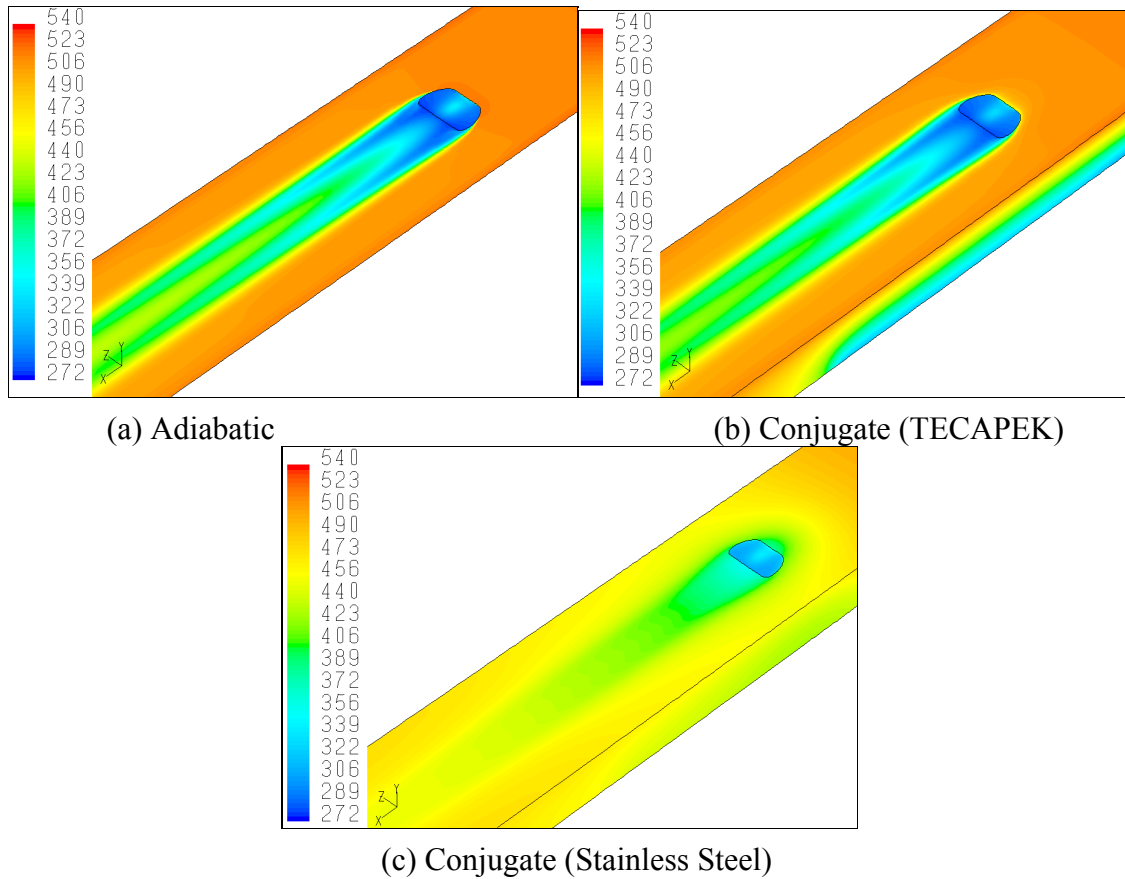
Figure 5.16. Comparison of predicted surface temperature contours ($Kelvin$) along the endwall in the film cooling hole region predicted by the RKE turbulence model with a hexahedral mesh.

In this chapter, a comparative study is presented which indicates the ability of three turbulence models to predict the film cooling effectiveness from a fan-shaped cooling hole. The realizable k-ϵ model, the SST k-ω model, and also $v^2 - f$ turbulence models have been considered. Three topology grids were considered: hexahedral-, hybrid-, and tetrahedral-topology meshes. The boundary conditions were chosen in a way to be more representative for typical gas turbine applications. The flow and temperature fields were discussed, in addition to local, two-dimensional distribution of film cooling effectiveness for the adiabatic and conjugate cases. Results were compared to experimental data in terms of centerline film cooling effectiveness downstream cooling-hole. The predicted results using a hybrid mesh are identical

to the ones predicted using a hexahedral mesh. This will reduce the required time to generate the mesh, especially for fan-shaped holes, and at the same time end up with an accurate results. Surprisingly, the RKE model performs better than the V2F model in predicting the surface temperature distribution and, hence, the film cooling effectiveness. Again, the results confirm that the conjugate heat transfer model shows a significant difference in the temperature predictions in comparison with the adiabatic model cases. The results also, show the effect of the conjugate heat transfer on the temperature field in the film cooling hole region, and the additional heating up of the cooling jet itself.

Up to this point, conjugate heat transfer (CHT) models have been developed to predict the metal temperature for three major cases: film cooling slots, cylindrical cooling holes, as well as fan-shaped cooling holes. A systematic computational methodology is adopted and applied to cylindrical and fan-shaped cooling holes. The results from the CHT simulations will be used to model the experimentally measured surface temperature and surface heat flux distributions along the endwall. So, in the following chapters, a boundary element method based inverse methodology will be developed as a means of retrieving the multi-dimensional heat flux distributions inside the cooling holes with application to film cooling slots, film cooling square holes and film cooling circular or cylindrical holes. The heat conduction problem will be solved using boundary element method (BEM), and the inverse problem will be solved using a genetic algorithm (GA).

CHAPTER 6

GA/BEM INVERSE TECHNIQUE TO RECONSTRUCT HEAT FLUX DISTRIBUTIONS WITHIN FILM COOLING SLOTS

6.1 Introduction

Retrieval of surface heat flux or convective heat transfer coefficient (h) is often accomplished using surface temperature histories provided by thermo-graphic techniques applied in controlled experiments and in conjunction with theoretical assumptions. In this study, the boundary element method (BEM) is applied to resolve 2D and 3D heat transfer and determine heat flux distributions or convective heat transfer coefficient by inverse methods. The BEM is ideally suited for this inverse problem as surface temperatures and fluxes appear as nodal unknowns, which are precisely the variables required in inverse analysis.

From the literature reviewed in Chapter 2, it is clear that, although film cooling has been studied extensively, there is a lack of information with regard to the thermal conditions within the film cooling slot itself. In this chapter, an inverse methodology will be developed as a means of determining heat flux distributions in film cooling slots (2D case). Thermal conditions are overspecified at exposed surfaces amenable to measurement, while the temperature and surface heat flux are unknown at the film cooling slot walls. The unknown temperature and surface heat flux distributions are determined in an iterative manner by solving an inverse problem whose objective is to adjust the film cooling slot wall temperatures and heat fluxes until the temperature and heat flux at the measurement surfaces are matched in an overall heat conduction solution. The heat conduction problem is solved using boundary element method (BEM), and the inverse problem is solved using a genetic algorithm (GA).

6.2 Inverse Problems

Engineering field problems may be broadly classified as forward or inverse. Forward problems are most commonly encountered in traditional engineering analysis. In a forward problem, the following are explicitly specified: governing equation for field variable, physical properties, boundary conditions, initial condition, and system geometry. The purpose of the analysis of the forward problem is to determine the field variable given these inputs. In contrast, in an inverse problem, the following are explicitly specified: part of the conditions in a forward problem and an overspecified condition (usually at the exposed boundary). The purpose of solving the inverse problem is to find the unknown in the conditions of the forward problem using the overspecified condition. Typically, the overspecified condition is provided usually by measuring a field variable at the exposed boundary, as in the case of the inverse geometric problem. However, in some inverse problems, the overspecified condition can be provided by internal measurements of the field variable via embedded sensors. Noise becomes an important concern in the solution of most inverse problems as the overspecified condition is usually provided by an experiment. All inverse problems rely on additional information that is provided by measurement whose values are ladened with random noise. Sampling can produce significant error, see Figure 6.1.
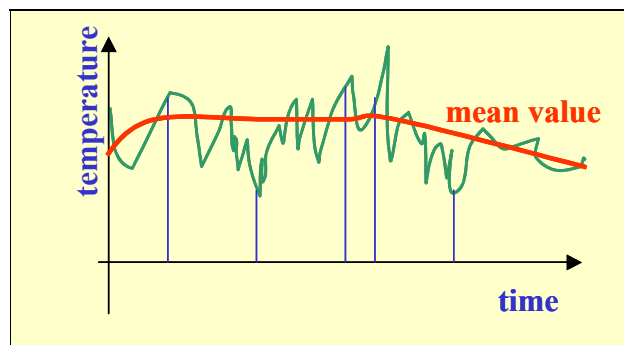
Figure 6.1. Illustration of error-ladened input.

To remedy this inherent feature of inverse problems, least-squares is used to smooth the results of sampling and the measurements are often approximated by simple trial functions to filter out the high frequency error. Moreover, the operator of the inverse problem is ill-conditioned (nearly singular) amplifying the input error, see Figure 6.2.
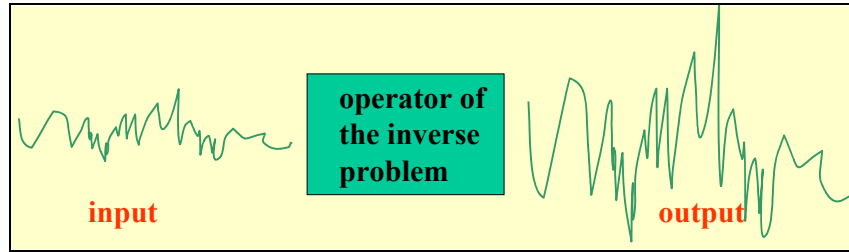
Figure 6.2. Illustration of the ill-posedness of inverse problems.

The methods adopted in the literature to overcome this feature either [82-84] modify the operator by using regularization via Thikonov method, or modify the solver to filter out high frequency error through singular value such as decomposition, conjugate gradient with appropriate stopping criterion, spectral techniques, Kalman filter etc... In this study, the ill-posedness issue is solved by a regularization procedure established in [108,109] to address the inverse reconstruction heat flux distributions.

6.3 Inverse Problem Methodology for Heat Flux Reconstruction

The inverse problem approach to film coefficient reconstruction is developed here. Consider the specific case of a two dimensional film cooling slot supplied by a plenum, see Figure 6.3(a). This configuration is used here for illustration in the development of the inverse problem methodology. The model consists of the domain of the main flow (hot gas), the coolant plenum supply (cold gas), and the endwall with a cooling slot of specified injection angle. The

outlet was located far downstream of the cooling slot. The measured temperature and heat flux over specified surfaces as shown in Figure 6.3(b), will be used as an input for the inverse problem to determine the unknown temperature and heat flux at the cooling slot walls. The heat flux will be measured using an optical thermo-graphic technique under development at University of Central Florida. The inverse problem algorithm developed herein for the reconstruction of heat transfer coefficient distributions is comprised of an objective function to be minimized; i.e. root mean square (RMS) error in heat flux, a minimization algorithm; i.e. genetic algorithm, and a forward problem field solver; i.e. the BEM. Each of these will be discussed in detail in the following sections.
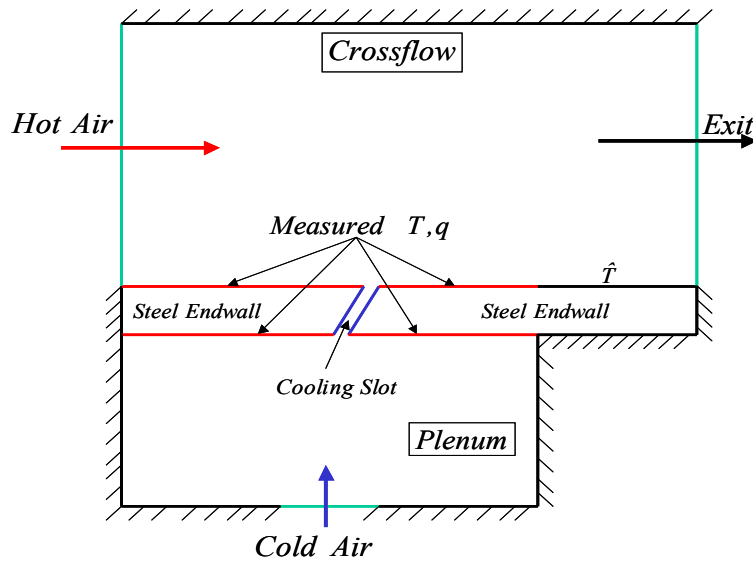
(a) overall configuration.
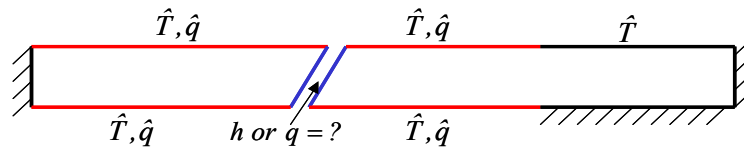
(b) domain of the inverse conduction problem.

Figure 6.3. Schematic for the inverse problem applied to a slot cooling configuration.

6.3.1 The Objective Function and Regularization

The objective of the inverse problem under consideration is to reconstitute the heat transfer coefficients or heat fluxes (h or q) at the cooling slot walls. Here, Cauchy conditions imposed at the surfaces exposed to the hot gases and to the film cooling supply plenum, as shown in the Figure 6.3(b). These surfaces are referred from here on as measurement surfaces. This is due to the fact that the heat flux and temperature are to be simultaneously measured in order to specify Cauchy conditions required to solve the inverse problem. In the inverse problem, the temperature is imposed at these surfaces and an initial heat flux distribution is guessed at the cooling slot walls. A forward steady-state heat conduction problem is solved using the BEM, and an objective function is defined to quantify the difference between the heat flux measured at the exposed surfaces and the heat flux predicted by the BEM under current heat flux estimates at the cooling slot surfaces. In order to reduce the number of unknowns, the heat fluxes are parametrically represented using radial basis functions (RBF) [132,133] as follows, see Figure 6.4:

$$q_{BEM}(\underset{\sim}{q}_A) = \sum_{j=1}^{N_A} q_{A_i} f_j(\vec{r}, \vec{r}_j) \tag{6.1}$$

where, N_A is the number of anchor points, $\vec{r}$ is the position vector, $\vec{r}_j$ is the position vector pointing to the jth anchor point, and the expansion coefficients q_{A_i} are found through a collocation procedure. The conic RBF, $f_j(\vec{r}, \vec{r}_j)$, used in this expansion is:

$$f_j(\vec{r}, \vec{r}_j) = \left| \vec{r} - \vec{r}_j \right| \tag{6.2}$$

Collocating at all the $j = 1, 2...N_A$ anchor points, there arises a linear equation:

$$\underset{=}{F} \underset{\sim}{q}_A = \underset{\sim}{q}_{BEM} \tag{6.3}$$

where $\underline{F}$ is an interpolant matrix. This linear system is solved by standard methods for the expansion coefficients q_{A_i}.
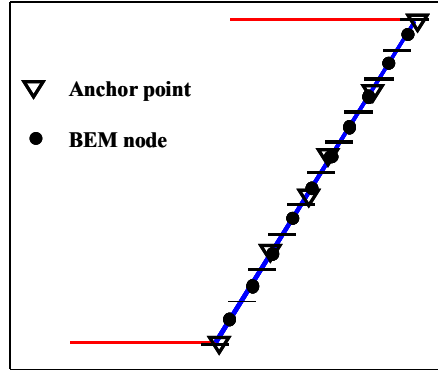
Figure 6.4. Schematic diagram for anchor points using radial basis functions (RBF).

Subsequently, the following objective function is defined to measure the difference between the BEM-computed heat flux, $q_{BEM_i}(\underset{\sim}{q}_A)$, at the $i = 1, 2...N_m$ measuring points and the measured heat flux $\widehat{q}_i$ at the measuring points under the current estimate of $\underset{\sim}{q}_A$:

$$S(\underset{\sim}{q}_A) = \sqrt{\frac{1}{N_m} \sum_{i=1}^{N_m} (q_{BEM_i}(\underset{\sim}{q}_A) - \widehat{q}_i)^2} \tag{6.4}$$

As has been discussed, inverse problems are ill-posed and small errors in inputs are reflected in large errors in the output unless regularization (a form of stabilization) or a stabilizing inverse problem solver is adopted. In this study, the objective functional is therefore regularized using a first order method [108,109] as:

$$S(\underset{\sim}{q}_A) = \sqrt{\frac{1}{N_m} \sum_{i=1}^{N_m} (q_{BEM_i}(\underset{\sim}{q}_A) - \widehat{q}_i)^2} + \beta \sqrt{\frac{1}{N_A} \sum_{i=1}^{N_A} (q_{A_i} - \widehat{q}_{ALS_i}(\underset{\sim}{q}_A))^2} \tag{6.5}$$

where, q_{A_i} is heat flux at the anchor points, and q_{ALS_i} is least-square curve fitted heat flux through the anchor points. In general, the number of anchor points (N_A) is less than the number of measuring points (N_m), and the number of anchor points is chosen in a manner to obtain a converged solution in the sense of small variations in the heat flux distributions as the number of

anchor points is varied. The regularization parameter (β) can take on values from zero (no regularization) to an appropriate positive number. The choice of optimal β is the subject of much research in the inverse problem community. For example, β may be chosen via the L-curve method [134,135] or the discrepancy principle [136,137]. In this study, the optimal β has been determined by constructing a plot of β versus the best fitness, $S(\underset{\sim}{q}_A)^{-1}$. The process starts by setting β to zero which results in the maximum best fitness, then β is increased until the reconstructed heat fluxes manifest no oscillatory behavior. At this point, if two lines are drawn from the two extreme ends, we take value of β at the point of intersection. The mean values of the heat fluxes at the anchor points $\widehat{\underset{\sim}{q}}_{ALS_j}$ are obtained by least-squares fitting a quadratic or higher order polynomial through the anchor point values $\underset{\sim}{q}_{A_j}$, see Figure 6.5:

$$\widehat{\underset{\sim}{q}}_{ALS} = \underline{\underline{P}} \, \underset{\sim}{q}_A \tag{6.6}$$

here, $\underline{\underline{P}}$ is the coefficient matrix of the normal equations, and its dimension is equal to the number of anchor points. The regularization has the effect of drawing the current flux distribution towards its current mean value. Obviously, the amount of stabilization depends on the value of β.
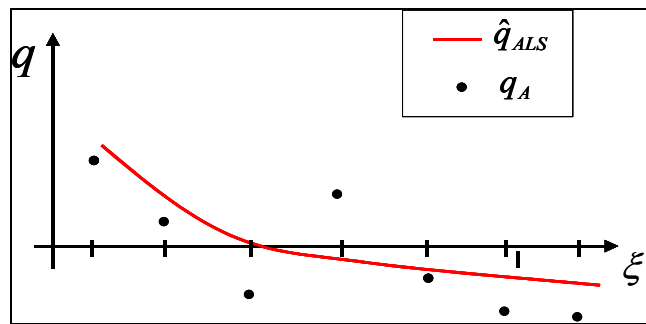
Figure 6.5. Schematic diagram for the least square curve fitting of the heat fluxes at the anchor points.

6.3.2 The Genetic Algorithm

The genetic algorithm (GA) optimization process begins by setting a random set of possible solutions, called the population, with a fixed initial size or number of individuals. Each individual is defined by optimization variables and is represented as a bit string or a chromosome, see Figure 6.6. The GA iteratively alters the heat flux distribution at the cooling slot walls until the measured surface heat fluxes are matched thus, satisfying the Cauchy conditions at the exposed measuring surfaces. It should be noted that GA maximizes objective function as they naturally seek the "best fit" [138]. Thus the objective function computed by the GA is actually:

$$S_{GA}(\underline{q}_A) = S(\underline{q}_A)^{-1} \tag{6.7}$$

The objective function, $S_{GA}(\underline{q}_A)$, is evaluated for every individual in the current population defining the fitness or their probability of survival. At each iteration of the GA, the processes of selection, crossover, and mutation operators are used to update the population of designs. A selection operator is first applied to the population in order to determine and select the individuals that are going to pass information in a mating process with the rest of the individuals in the population. This mating process is called the crossover operator, and it allows the genetic information contained in the best individuals to be combined to form offsprings. Additionally, a mutation operator randomly affects the information obtained by the mating of individuals. This is a crucial step for continuous improvement.

A series of parameters are initially set in the GA code, which determine and affect the performance of the genetic optimization process. The number of parameters per individual or optimization variables, the size of the bit string or chromosome that defines each individual, the number of individuals or population size per generation, the number of children from each mating, the probability of crossover, and the probability of mutation are among the parameters that control the optimization process. This set of operations are carried out generation after

generation until either a convergence criterion (a preset level of acceptable fitness) is satisfied or a maximum number of generations is reached. It is also important to point out that three important features distinguish GA from the other evolutionary algorithms, namely: (1) binary representation of the solution, (2) the proportional method of selection, and (3) mutation and crossover as primary methods of producing variations.
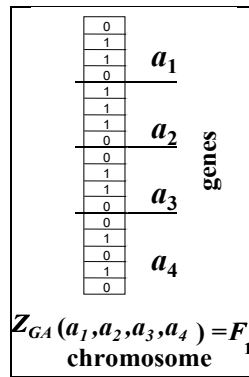
Figure 6.6. Example of an individual in the population characterized by four parameters (genes) encoded in a chromosome yielding the individuals fitness value F_1.

In nature, the properties of an organism are described by a string of genes in the chromosomes. Therefore, if one is trying to simulate nature using computers one must encode the design variable in a convenient way. We adopt a haploid model using a binary vector to model a single chromosome. The length of the vector is dictated by the number of design variables and the required precision of each design variable. Each design variable has to be bounded with a minimum and a maximum value and in the process the precision of the variable is determined. The number of divisions used in the discretization has to be an integer power of two. This procedure allows an easy mapping from real numbers to binary strings and vice versa. This coding process represented by a binary string is one of the distinguishing features of GA and differentiates them from other evolutionary approaches. The haploid GA places all design variables into one binary string, called a chromosome or off-spring. The information contained in the string of vectors comprising the chromosome characterizes an individual in a population. In

turn, each individual is equipped with a given set of design variables to which corresponds a value of the objective function. This value is the measure of "fitness" of the individual design. In a GA, poorly fit designs are not discarded; rather they are kept, as in nature, to provide genetic diversity in the evolution of the population. This genetic diversity is required to provide forward movement of the population during the mating, crossover, and mutation processes which characterize the GA.

The initial population size may grow or diminish to mimic actual biological systems. However, in the GA used here, the population size is not allowed to change while the program is running. Once the population size is fixed, the algorithm initialize all of the chromosomes. This operation is carried out by assigning a random value of zero or one for each bit contained in each of the chromosomes. After initializing the population, evaluation of the fitness of each individual is performed by computing the objective (or fitness) which of course represents a set of possible solutions. Having the values of the objective function for each individual, the selection process can be started. First values of the fitness function for each individual have to be added, and then the probability of being a selected individual is calculated as the ratio between the value of the fitness function of each individual and the sum of all objectives function values. This is given by:

$$P_{selected} = \frac{Fitness(\mathbf{v}_i)}{\sum\limits_{i=1}^{pop-size} Fitness(\mathbf{v}_i)} \tag{6.8}$$

where $\mathbf{v}_i$ is i-th member of the population, and $Fitness(\mathbf{v}_i)$ is the measure of the fitness of that member under its currently evolved parameter set configuration. A weighted roulette wheel is generated, where each member of the current population is assigned a portion of the wheel in proportion to its probability of selection. The wheel is spun as many times as there are individuals in the population to select which members mate. Obviously, some chromosomes would be selected more than once, where the best chromosomes get more copies, the average

stay even, and the worst die off. Once selection has been applied, crossover and mutation occur to the surviving individuals. These operations further expand genetic diversity in the current population. All other probabilities referred to in the description of the GA adopted in this study are computed in an analogous fashion as the selection probability.

The probability of crossover (P_c) is an important parameter that defines the expected population size ($P_c \bullet pop\text{-}size$) of chromosomes which undergoes crossover operation. This is a mating process that allows individuals to interchange intrinsic information contained in the chromosomes. The operation may be implemented in two steps: (1) a random selection based on the probability of crossover is performed to obtain pairs of individuals, and (2) a random number is generated between the first position of the binary vector and the last one to indicate the location of the crossing point which delineates the location about which genetic information is interchanged between two chromosomes.

The mutation operator is the final operator implemented. The probability of mutation (P_m) gives the expected number of mutated bits and every bit in all chromosomes in the whole population has an equal chance to undergo mutation: switch of a bit from zero to one or vice-versa. This process is implemented by generating a random number within the range (0...1) for each bit within the chromosome. If the generated number is smaller than (P_m) the bit is mutated. When the mutation is done on a bit-by-bit basis it is called the creep mutation. Another type of mutation is the jump mutation which is applied to an individual selected to be mutated from this perspective. In this case all bits within the chromosome are switched from zero to one and vice-versa. Following selection, crossover and mutation of the new population is ready for its next evolution until the convergence criteria fitness is reached. It is the very nature of the binary representation of the design variables of the objective function and the random search process which provide yet another implicit degree of regularization in this optimization process. The sensitivity of the objective function can be tuned depending on the size of each element of the chromosome. Thus, low bit representation is insensitive to large variations in input (regularized

but may lead to poor solution due to low resolution), while high bit representation is sensitive to large variations in input (not regularized and therefore may lead to poor solution as well). There is a range of bit size which produces a regularized and sensitive response leading to stable solutions.

The following suitable parameters are chosen to generate results: population size of 50 individuals/generation, a string of eight bits to define each parameter within each individual, one child per mating, a 4% probability of mutation, a 20% probability of creep mutation, and a 50% probability of crossover. This combination of parameters and procedures has been proven to yield efficient and accurate optimization results for different studies carried out in this dissertation.

6.3.3 The Forward Heat Conduction Solver

The boundary elements method (BEM) is used to solve the forward problem. This technique is based on integral equation formulations and is ideally suited for the problem under consideration as it requires only a boundary mesh for steady linear or non-linear heat conduction and the nodal unknowns appearing in the equations are the temperature and heat flux. The governing equation for steady state heat conduction with constant thermal conductivity and no internal heat generation is the Laplace equation for the temperature; i.e.:

$$\nabla^2 T = 0 \tag{6.9}$$

An integral equation (BIE) for the temperature is readily derived as [139,140]:

$$C(\xi)T(\xi) + \oint_{S(x)} q(x)T^*(x,\xi)dS(x) = \oint_{S(x)} T(x)F(x,\xi)dS(x) \tag{6.10}$$

where $C(\xi)$ is one for a source point at the interior and 1/2 for a source point on a smooth boundary, $S(x)$ is the surface bounding for the domain of interest, ξ is the source point, x is the

field point, $q(x)$ is the heat flux, $T^*(x, \xi)$ is the fundamental solution, and $F(x, \xi)$ is its normal derivative with respect to the outward normal.

$$
\begin{aligned}
T^*(x, \xi) &= (-1/2\pi k)lnr(x, \xi) & in\,(2D) \\
T^*(x, \xi) &= 1/4\pi kr(x, \xi) & in\,(3D) \\
F(x, \xi) &= -k\partial G(x, \xi)/\partial n \\
q(x) &= -k\partial T(x)/\partial n \\
C(\xi) &= 1 \ \ if \ \ \xi \ \in \Omega \\
C(\xi) &= 1/2 \ \ if \ \ \xi \ \notin \Omega
\end{aligned}
\tag{6.11}
$$

The integral equation is discretized by introducing a pattern of N-boundary nodes over the surface and boundary elements to model the boundary, temperature, and flux distributions and can be expressed in standard matrix form as [141-143]:

$$
\underline{\underline{H}}\,\underline{T} = \underline{G}\,\underline{q} \tag{6.12}
$$

The influence coefficient matrices $\underline{G}$ and $\underline{H}$ are evaluated numerically, depending on the type of element chosen and the dimension of the problem. In these simulations, all computations are carried out in 2D using exclusively discontinuous quadratic isoparametric boundary elements. In this element type, the geometry, temperature and heat flux are modeled using bi-quadratic shape functions. However, the temperature and heat flux end-nodes are offset from the geometric end-nodes, see Figure 6.7, consequently, this type of element is termed discontinuous. It offers the advantage of superior heat flux determination with none of the complexities plaguing continuous elements, in particular in 3D.
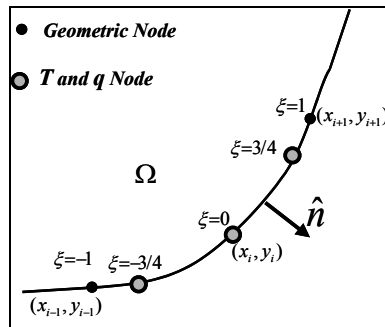
Figure 6.7. Discontinuous isoparametric element: quadratic geometry, T and q.

82

Notice that the geometric nodal locations of the element are ordered counterclockwise such that the normal vector always points outwards from the domain of the problem, thus uniquely defining the outward-drawn normal. The global coordinate system (x, y) is transformed into a local coordinate system (ξ) using the following bi-quadratic shape functions relationships:

$$x(\xi) = \sum_{m=1}^{3} N_m(\xi) x_m \tag{6.13}$$

$$y(\xi) = \sum_{m=1}^{3} N_m(\xi) y_m$$

where x_m and y_m are the locations of the geometric nodes for the element Γ_j. The three bi-quadratic shape functions for the geometry are defined as follows:

$$N_1(\xi) = \frac{\xi}{2}(\xi - 1) \tag{6.14}$$
$$N_2(\xi) = (1 - \xi)(1 + \xi)$$
$$N_3(\xi) = \frac{\xi}{2}(\xi + 1)$$

As mentioned above, the discontinuous boundary elements feature temperature and heat flux end-nodes offset $12.5\,\%$ from the geometric end-nodes while the central node is colocated with the geometric central node of the boundary element, Γ_j, thus:

$$T(\xi) = \sum_{j=1}^{3} M_j(\xi) T_j \quad \text{and} \quad q(\xi) = \sum_{j=1}^{3} M_j(\xi) q_j \tag{6.15}$$

where T_j and q_j are the nodal temperatures and heat fluxes, and the shape functions for the dependent variable are:

$$M_1(\xi) = \frac{2}{9}\xi(4\xi - 3) \tag{6.16}$$
$$M_2(\xi) = \frac{1}{9}(3 - 4\xi)(3 + 4\xi)$$
$$M_3(\xi) = \frac{2}{9}\xi(4\xi + 3)$$

The influence coefficients H_{ij} and G_{ij} that are elements of the matrices $\underline{G}$ and $\underline{H}$ are defined as integrals over the boundary element Γ_j:

$$H_{ij} = \int_{\Gamma_j} M_j(\xi) F(x, \xi_i) \, d\Gamma \qquad (6.17)$$

$$G_{ij} = \int_{\Gamma_j} M_j(\xi) T^*(x, \xi_i) \, d\Gamma$$

and these are evaluated using adaptive quadratures based on Gauss-Kronrod rules. Introducing the boundary conditions, into the discretized BEM equations leads to the standard algebraic form:

$$[A]\{x\} = \{b\} \qquad (6.18)$$

This equation can be solved by direct methods such as LU decomposition or by iterative methods for non-symmetric equations such as generalized minimal residual method (GMRES).

As an example of a BEM mesh, quadratic discontinuous elements have been used to discretize the geometry of interest here. A total of 200 elements used to discrete the whole domain, such that the left block has 60 elements and the right block has 140 elements, and each side of the cooling slot has ten elements. The surface mesh is shown in Figure 6.8 below.

Figure 6.8. Surface mesh of the BEM direct problem.

6.4 Numerical Results

We now present the simulated results in two parts: (1) results of the direct conduction problem, and (2) results of the inverse problem. The input to the inverse problem is provided from the conjugate heat transfer (CHT) simulations for the case of one cooling slot. For more details, see chapter three. Moreover, the direct conduction problem is carried out to provide a consistency check between the commercial CFD code applied for the CHT simulations and the in-house BEM code that is the forward solver for the inverse problem.

6.4.1 Results of The Direct Problem

We establish a solution to the forward problem as a numerical consistency check of the (BEM) solution; i.e. in house code, and conjugate heat transfer (CHT) solution; i.e. commercial code. Since the BEM surface mesh and CHT surface mesh are different from each other, a radial basis function interpolation approach is used to pass information from one grid to the other. The input to the direct problem is the CHT wall temperatures at solid surfaces, as shown in Figure 6.9, to check consistency in the BEM-computed heat fluxes.
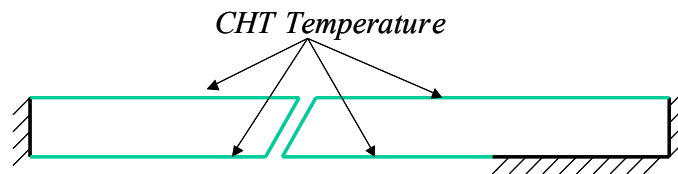
Figure 6.9. Schematic diagram of the BEM direct problem.

The discretized governing equations with the specified boundary conditions have been solved, and the temperature distribution with the heat flux direction is shown in the Figure 6.10.

It can be seen that the temperature expands from $295°K$ to $345°K$, which matches very well the CHT solution.
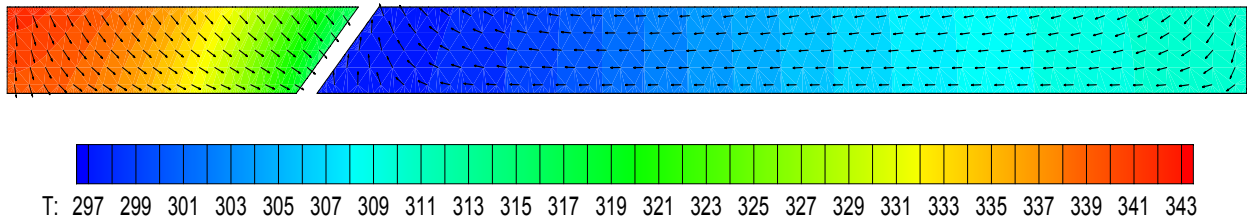
Figure 6.10. Temperature distribution predicted by the BEM direct solution.

The BEM-computed heat fluxes have been compared to the CHT-computed ones in Figure 6.11. The two are in good agreement. Note that the CHT models solved the parabolic heat conduction equation up to the steady-state while the BEM solved the elliptic steady conduction solution.

(a) left edge   (b) right edge
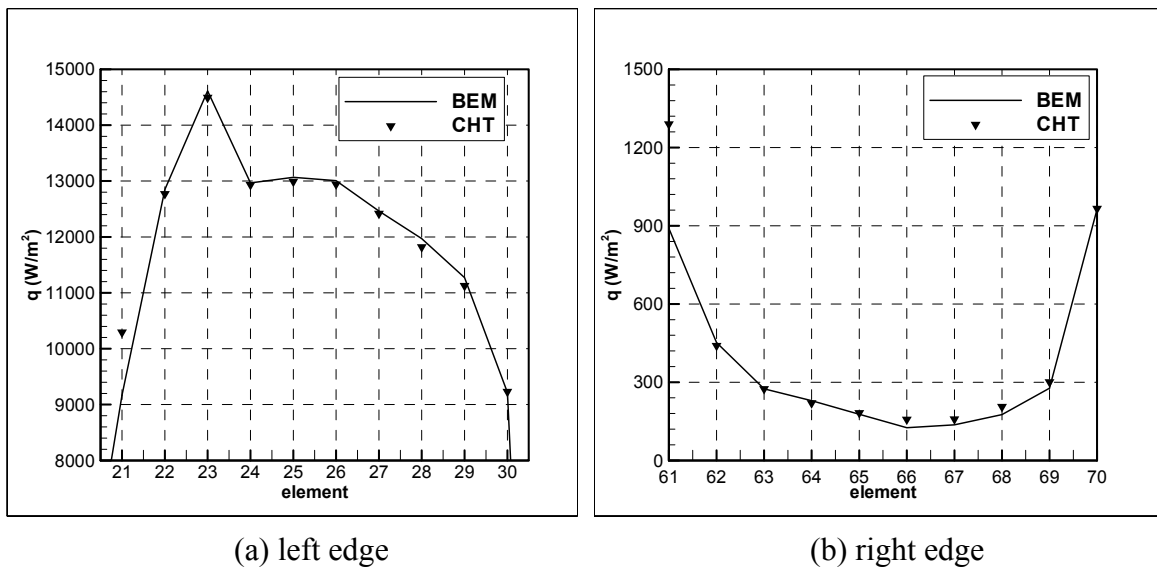
Figure 6.11. Comparison of direct BEM and CHT heat fluxes along cooling slot edges.

6.4.2 Results of The Inverse Problem

The inverse problem results are now presented for several cases. First, we consider the case of exact input data. The problem has been solved for two blocks, the first block models the left edge of the cooling slot, which has 60 elements. The elements of the left edge of the cooling slot are $21 - 30$. The second block models right edge of the cooling slot, which has 140 elements. The elements of the right edge of the cooling slot are $61 - 70$, as shown in the Figure 6.12 below. The problem has been solved with 21 anchor points. The results for the reconstructed heat fluxes at the left and right edges of the cooling slot are shown in Figure 6.13. The results are shown at zero regularization with 7th order polynomial least-squares fit. The 7th order polynomial was chosen to obtain the best fit in q_A without introducing oscillations in the functional approximations. An initial guess of q between $0 - 15 \, kW/m^2$ along the left edge and $0 - 2 \, kW/m^2$ along the right edge is taken at all anchor points to begin the minimization process in all cases.
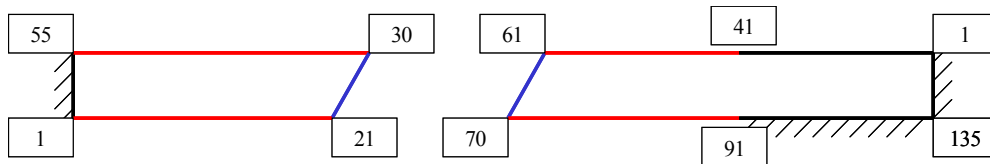
Figure 6.12. Reference node numbering for the BEM discretization of the inverse problem.

Figure 6.14 shows best fitness as function of regularization/tuning parameter. In this figure, the process started with zero regularization which gives the maximum best fitness, then the regularization parameter is increased until the reconstructed heat fluxes manifest no oscillatory behavior. If two lines are drawn from the two extreme ends, the optimal value of β is found at the point of intersection. In this case, the best fitness was at a regularization parameter of 10^{-7}

for the left edge and 10^{-5} for the right edge. As a result, the reconstructed heat fluxes matched the measured ones as shown in Figures 6.15 and 6.16.
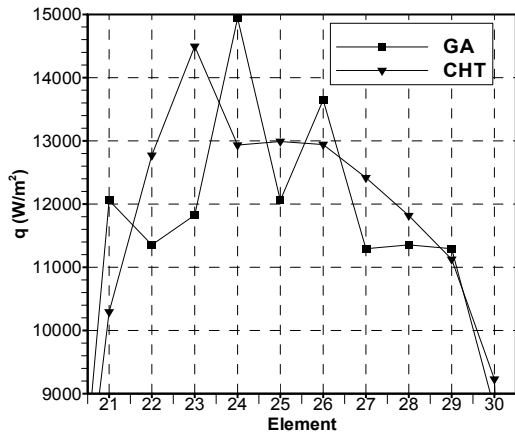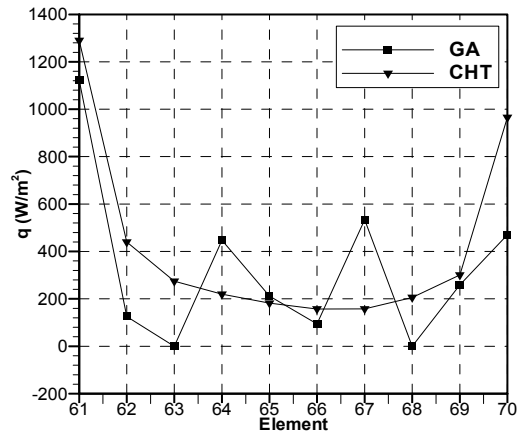
(a) left edge   (b) right edge

Figure 6.13. BEM reconstructed heat fluxes (q) through cooling slot with regularization parameter; ($\beta = 0$).
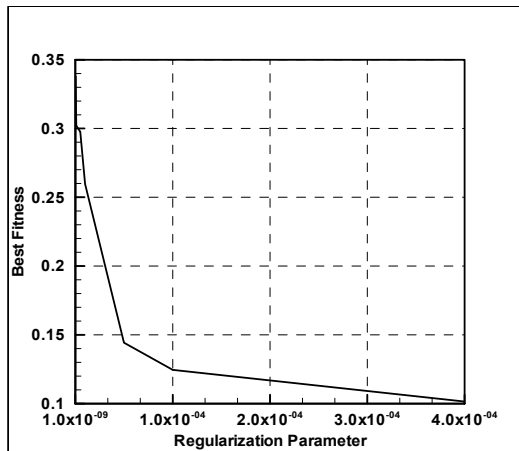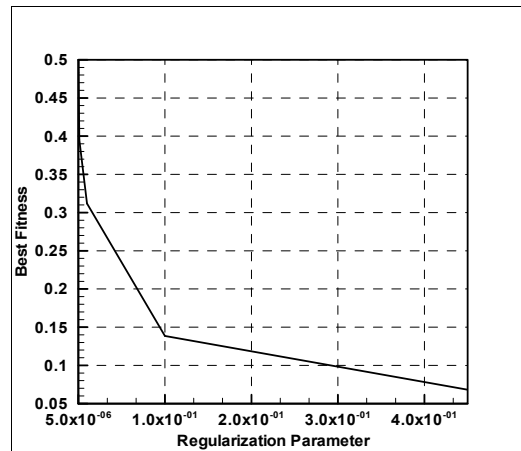
(a) left edge   (b) right edge

Figure 6.14. Plot of the regularization parameter β versus the best fitness.
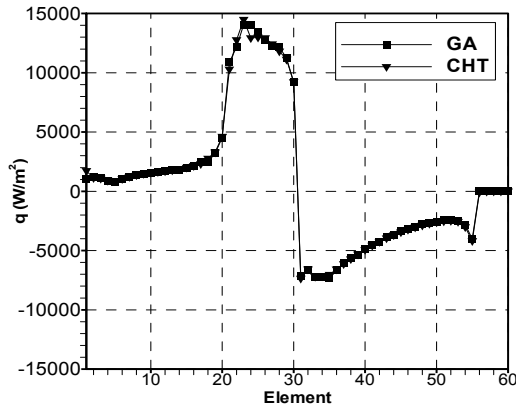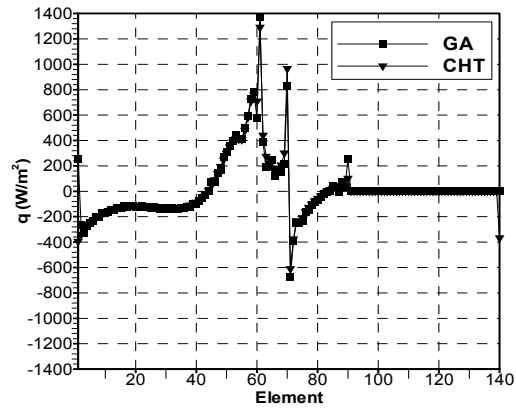
(a) $\beta = 10^{-7}$ (b) $\beta = 10^{-5}$

Figure 6.15. Comparison of reconstructed regularized GA and CHT heat fluxes at: (a) left block and (b) right block.
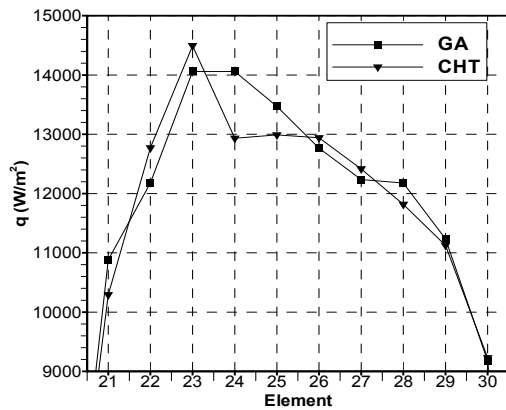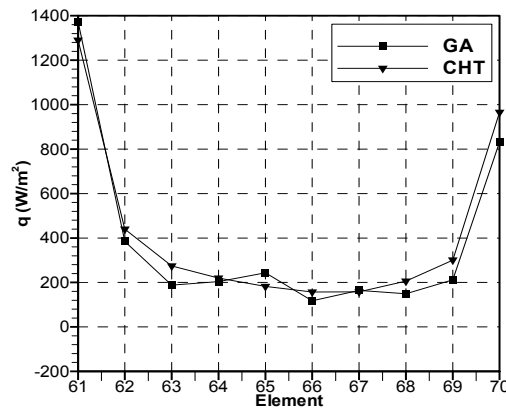
(a) $\beta = 10^{-7}$ (b) $\beta = 10^{-5}$

Figure 6.16. Close up of reconstructed regularized GA and CHT heat fluxes through cooling slot at: (a) left edge and (b) right edge.

Next, results are presented for the case of error-laden inputs. Here, a random number generator is employed to generate random errors of maximum levels $\pm 0.5°C$ in the temperature and $\pm 50\ W/m^2$ in the heat flux. The results are shown in the figures below. It can be noted that the GA reconstructed heat fluxes are robust to these random errors yielding very accurate results. The reconstructed heat fluxes at an input error of $\pm 0.25°C$ and $\pm 25\ W/m^2$ are shown in

Figure 6.17 along left and right edges of the cooling slot and Figure 6.17 for an input error of $\pm\,0.5°C$ and $\pm 50\ W/m^2$. It can be seen that the reconstructed and the simulated heat fluxes are matching each other quite well.
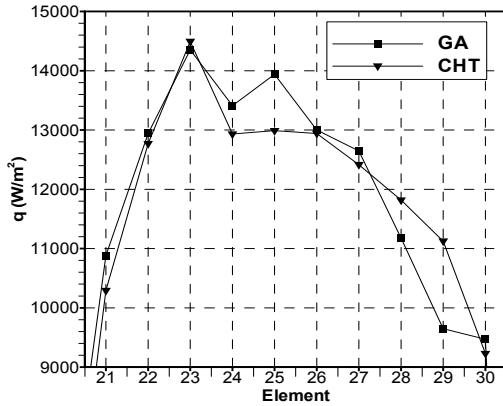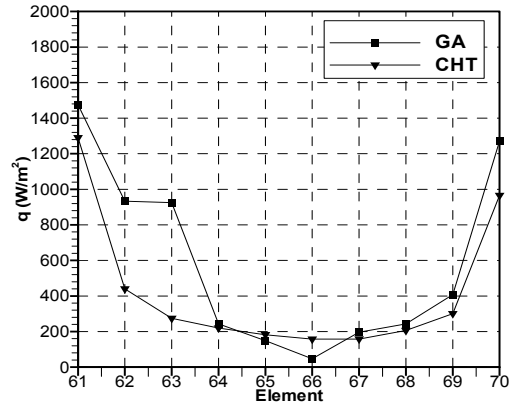
(a) $\beta = 0.1$ (b) $\beta = 0.01$

Figure 6.17. Comparison of reconstructed heat flux using GA-based method with CHT heat fluxes through cooling slot at: (a) left edge and (b) right side. Input Errors: $\epsilon_T = \pm0.25°C, \epsilon_q = \pm\,25W/m^2$.
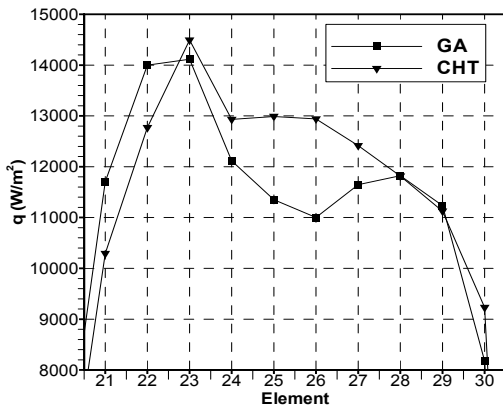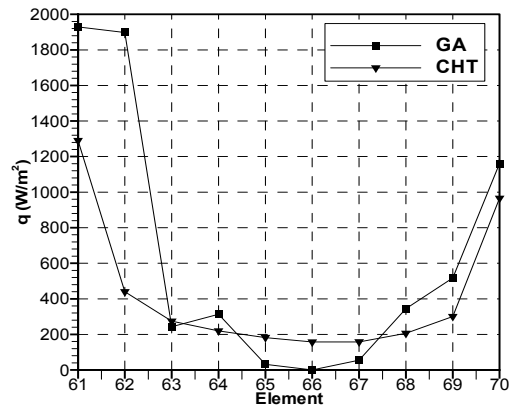
(a) $\beta = 0.1$ (b) $\beta = 0.01$

Figure 6.18. Comparison of reconstructed heat flux using GA-based method with CHT heat fluxes through cooling slot at: (a) left edge and (b) right side. Input Errors: $\epsilon_T = \pm0.5°C, \epsilon_q = \pm\,50W/m^2$.

In this chapter, an inverse problem approach as a means of determining heat flux distributions along the walls of cooling slots is developed. The heat flux distributions are determined in an iterative manner by solving an inverse problem whose objective is to adjust the film cooling slot wall temperatures and heat fluxes until the temperature and heat flux at the measurement surfaces are matched in an overall heat conduction solution. The heat conduction problem is solved using boundary element method (BEM), and the inverse problem is solved using a genetic algorithm (GA). It can be noted that the GA reconstructed heat flux is robust, yielding very accurate results to both cases: exact input data, and error-laden inputs.

In the following chapter, a more generalized methodology will be developed to reconstruct the heat flux distributions along the walls of the cooling slots/holes, this methodology will be applied to one- and two-cooling slots. This methodology is called a singular superposition BEM inverse technique for the reconstruction of multi-dimensional heat flux distributions. The advantage of this approach is eliminating the need to mesh the surface of the film cooling slot and the need to parametrize the heat flux over that surface. Rather, the heat flux is determined in a post-processing stage after the inverse problem is solved. This constitutes a tremendous advantage in solving the inverse problem, particularly in 3D applications.

CHAPTER 7

SINGULARITY SUPERPOSITION/BEM INVERSE TECHNIQUE TO RECONSTRUCT HEAT FLUX DISTRIBUTIONS WITHIN FILM COOLING SLOTS

7.1 Introduction

In the previous chapter, an inverse methodology based on boundary element method (BEM) and a genetic algorithm (GA) was developed. Here, a more generalized technique will be developed to reconstruct the heat flux distributions for the cases of one- and two-cooling slots. This technique is called a singular superposition/BEM inverse technique or a hybrid singularity superposition/boundary element-based inverse method for the reconstruction of multi-dimensional heat flux distributions. Cauchy conditions are imposed at exposed surfaces that are readily reached for measurements while convective boundary conditions are unknown at surfaces that are not amenable to measurements such as the edges of cooling slots.

The purpose of the inverse analysis is to determine the heat flux distribution along cooling slot surfaces. This is accomplished in an iterative process by distributing a set of singularities at the vicinity of the cooling slot surface inside a fictitious extension of the physical domain with a given initial strength distribution. A forward steady-state heat conduction problem is solved using the boundary element method (BEM), and an objective function is defined to measure the difference between the heat flux measured at the exposed surfaces and the heat flux predicted by the BEM under the current strength distribution of the singularities. A genetic algorithm (GA) iteratively alters the strength distribution of the singularities until the measuring surfaces heat fluxes are matched, thus satisfying Cauchy conditions. Subsequent to the solution of the inverse problem, the heat flux at the inaccessible surface is computed using BEM. The hybrid singularity superposition/BEM approach thus eliminates the need to mesh the surface of

the film cooling slot and the need to parametrize the heat flux over that surface. Rather, the heat flux is determined in a post-processing stage after the inverse problem is solved. This constitutes a tremendous advantage in solving the inverse problem, particularly in 3D applications.

7.2 Singularity Superposition and Inverse Problem Methodology

Again, the inverse problem approach to heat flux reconstruction is developed here. Considering the specific case of a 2D film cooling slot supplied by a plenum, see Figure. 7.1(a). The model consists of a domain for the main flow (hot air or crossflow), the coolant plenum supply (cold air), and the endwall with single or multiple cooling slots. The measured temperature and heat flux at over-specified surfaces are shown in Fig. 7.1(b), will be used as an input for the inverse problem to determine the unknown temperature and heat flux at the film-cooling slot walls.

The inverse problem algorithm developed herein is comprised of the forward problem solver (i.e. a hybrid singular superposition/BEM method) and an inverse problem solver (i.e. a genetic algorithm to determine strength distribution of the sinks to match Cauchy conditions imposed at exposed surfaces).

(a) overall configuration.

(b) domain of the inverse conduction problem.
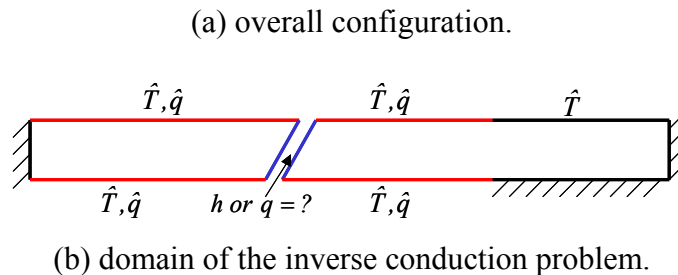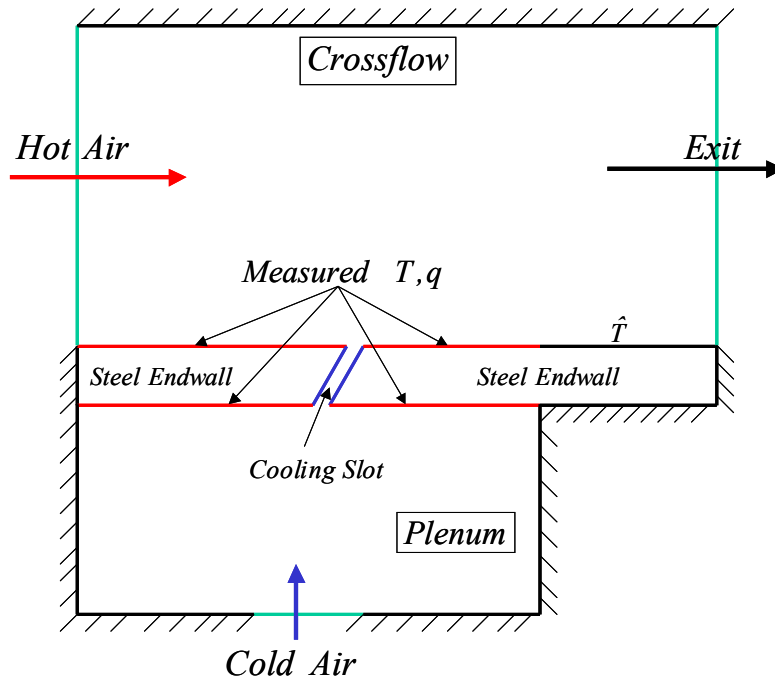
Figure 7.1. Schematic diagram for the Inverse Problem.

7.2.1 The Forward Problem Solver

The purpose of the inverse problem is to determine the heat flux distribution (q) at the cooling slot edges. This is accomplished in an iterative process. The temperature is imposed at these edges. To simulate the extraction of energy from the coolant, a distribution of singularities (sinks) is located in the vicinity of the surface within a fictitious extension of the physical domain with a given initial strength distribution, see Figure 7.2. The fictitious boundaries will be insulated to prevent energy from flowing through them. This way all the energy that was extracted through the physical cooling surface is captured by the sinks.

94
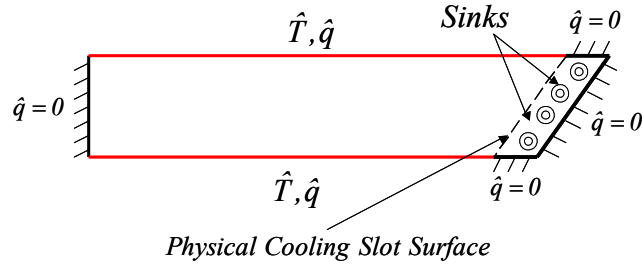
Figure 7.2. Thermal singularity superposition configuration.

The mathematical formulation that follows this idea consists of the Poisson equation for the temperature $T(x, y)$ where the generation term is the summation of singular field perturbations characterized by NS localized Dirac delta functions as:

$$\nabla.[k\nabla T(x,y)] + \sum_{K=1}^{NS} Q_K \delta(x, y, x_K, y_K) = 0 \qquad (7.1)$$

where k is the thermal conductivity, Q_K represents the strength of the sinks, NS is the number of sinks, (x_K, y_K) are location of the Kth sink, and δ is the Dirac delta function. Although an analytical direct solution is possible for the configuration shown above, a numerical approach will be adopted for generality. A numerical technique that lends itself perfectly for this application is the boundary element method (BEM) due to its boundary-only discretization feature, and its ability to relate the field variable values anywhere in the domain to the information along the boundary. These characteristics of the BEM will make it possible to isolate the effects of the added singular perturbations and compute the field variable values only where necessary. A standard BEM formulation starts with the introduction of an arbitrary function $G(x, y, x_i, y_i)$ and a transformation of the governing equation into an integral equation over the domain Ω as:

$$\int_\Omega \nabla.[k\nabla T(x,y)]G(x, y, x_i, y_i)d\Omega = \sum_{K=1}^{NS} Q_K \int_\Omega \delta(x, y, x_K, y_K)G(x, y, x_i, y_i)d\Omega \quad (7.2)$$

To transform the domain integral into contour integrals over the boundary Γ; Green's second identity is applied on the left-hand side and the sifting property of the Dirac delta function is applied on the right-hand side of the equation above yielding:

$$\int_{\Omega} \nabla.[k\nabla G(x,y,x_i,y_i)]\, T(x,y)\, d\Omega + \oint_{\Gamma} H(x,y,x_i,y_i)\, T(x,y)\, d\Omega - \tag{7.3}$$

$$\oint G(x,y,x_i,y_i)\, q(x,y)\, d\Gamma = \sum_{K=1}^{NS} Q_K\, G(x_K,y_K,x_i,y_i)$$

where:

$$H(x,y,x_i,y_i) = -k\, \partial G(x,y,x_i,y_i)/\partial n \tag{7.4}$$
$$q(x,y) = -k\partial T(x,y)/\partial n$$

Now, the Dirac delta function is used to perturb the adjoint operator on the arbitrary function $G(x,y,x_i,y_i)$ present in the last remaining domain integral in the equation as:

$$\nabla.[k\nabla G(x,y,x_i,y_i)] = -\delta(x,y,x_i,y_i) \tag{7.5}$$

For 2D problems $G(x,y,x_i,y_i)$ can be found to be the free-space solution to the adjoint equation as:

$$G(x,y,x_i,y_i) = \frac{-1}{2\pi k} ln\sqrt{(x-x_i)^2 + (y-y_i)^2} \tag{7.6}$$

Again, the sifting property of the Dirac delta function is recast to lead to the following boundary-only integral equation:

$$C(x_i,y_i)\, T(x_i,y_i) - \oint_{\Gamma} T(x,y)H(x,y,x_i,y_i)d\Gamma + \tag{7.7}$$

$$\oint_{\Gamma} q(x,y)\, G(x,y,x_i,y_i)d\Gamma = \sum_{K=1}^{NS} Q_K\, G(x_K,y_K,x_i,y_i)$$

Introducing boundary discretization yields the following relation:

$$C_i\, T_i - \sum_{j=1}^{N} \widehat{H}_{ij}\, T_j + \sum_{j=1}^{N} G_{ij}\, q_j = \sum_{K=1}^{NS} Q_K\, G(x_K,y_K,x_i,y_i) \tag{7.8}$$

where:

$$C_i = 1 \quad \text{if} \ (x_i, y_i) \in \Omega \qquad (7.9)$$
$$C_i = \frac{1}{2} \quad \text{if} \ (x_i, y_i) \in \Gamma$$
$$C_i = 0 \quad \text{if} \ (x_i, y_i) \notin \Omega$$

Following the discretization of the boundary (Γ) with (N) nodal locations and the collocation of (x_i, y_i) at these (N) locations, the above equation reduces to the following simultaneous set:

$$\sum_{j=1}^{N} G_{ij}\, q_j - \sum_{j=1}^{N} H_{ij}\, T_j = S_i \qquad (7.10)$$

where:

$$H_{ij} = \widehat{H}_{ij} - \frac{1}{2}\delta_{ij} \qquad (7.11)$$
$$S_i = \sum_{K=1}^{NS} Q_K\, G(x_K, y_K, x_i, y_i)$$

Again, a quadratic discontinuous isoparametric boundary elements were used [140]. Provided that a well-posed problem is conformed with a properly defined geometry and set of boundary conditions, see Figure 7.3, the discretized boundary integral equation, Equation. (7.10) is reduced to:

$$A_{ij}\, x_j = b_i + S_i \qquad (7.12)$$

with $i = 1...N$ and where S_i contains the effects of the added singularities Q_K. The solution to this system provides the full distribution of temperatures and fluxes around the boundary that can be used later in the same formulation to calculate temperatures and heat fluxes anywhere in the domain Ω. Notice that the system in Equation (7.12) needs to be generated and decomposed only once. Changing the strength of the singularities can be efficiently accounted for in the solution by just updating the right-hand side vector and solving the system again by back substitution.
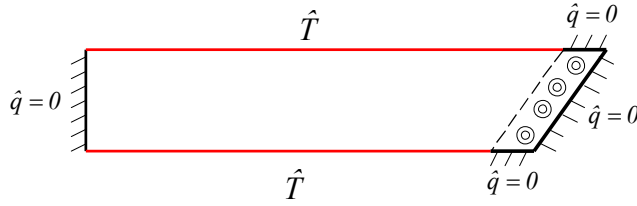
Figure 7.3. Set of boundary conditions for the BEM problem.

7.2.2 The Inverse Problem Solution

The purpose of the inverse problem is to determine the heat flux distributions at the film cooling slot edges. This is done in an iterative process; the temperature is imposed at these surfaces and a distribution of sinks is located within the fictitious extension of the physical domain with a given initial strength distribution. A forward steady-state heat conduction problem is solved using the boundary element method (BEM), and an objective function is defined to measure the difference between the heat flux measured at the exposed surfaces and the heat flux predicted by the BEM under current strength distribution of the sinks. This can be accomplished by minimizing the following least-squares functional:

$$S(Q_K) = \sqrt{\frac{1}{N_m} \sum_{i=1}^{N_m} [q_i(Q_K) - \widehat{q}_i]^2} \tag{7.13}$$

where N_m is the number of measuring points, $\widehat{q}_i$ are the measured heat fluxes at the measuring points, and $q_i(Q_K)$ are the computed heat fluxes for a given set of sink strengths. An additional term might be added to the functional to act as a regularization term as:

$$S(Q_K) = \sqrt{\frac{1}{N_m} \sum_{i=1}^{N_m} [q_i(Q_K) - \widehat{q}_i]^2} + \beta \sqrt{\sum_{i=1}^{Nw} [q_{w_i}(Q_K) - \overline{q}_w]^2} \tag{7.14}$$

98

where, Nw is the number of measuring points at the film-cooling slot wall, β is the regularization parameter, $q_{w_i}(Q_K)$ are the computed heat fluxes at slot physical wall for a given set of sink strengths, and $\overline{q}_w$ are the averaged normal heat fluxes at the physical cooling slot wall. However, the inherent regularization property of genetic algorithm (minimization method of choice in this study), in addition to the discrete nature of a finite number of singularities (sinks) to simulate the extracted energy, makes it unnecessary to add any additional regularization to the functional, and would just slow down the minimization process (i.e. β was set to zero). Once the functional, $S(Q_K)$, is minimized, the resulting heat flux distribution along the physical film cooling slot wall can be smoothed-out by simple least-squares means. Figure 7.4 below illustrates the calculation of the normal heat fluxes at the edge of the cooling slot at a post-processing stage by computing the heat flux vector components at internal points of the extended domain distributed along the location of the actual edge.
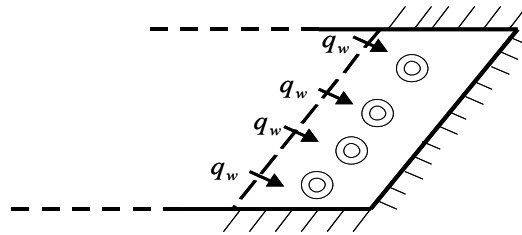
Figure 7.4. Calculation of the cooling surface heat fluxes after the functional optimization process.

As the inverse problem is now well-defined, a means of minimization of the objective function must be sought to be able to provide a global approximation that disregards the multiple local minimae that will arise as a result of the inherent non-linearity of this problem. This feature along with many more can be found in the genetic algorithm (GA) lending themselves perfectly for such application. GA is robust adaptive search techniques that mimic the idea of Darwinian evolution using rules of natural selection to investigate highly complex multidimensional

problems. As a non-gradient-based optimization technique the use of GA is advantageous for this until a best-fit is found that application.

7.2.3 The Genetic Algorithm

Again, the optimization technique for this case is chosen to be the genetic algorithm (GA), for more details see section 6.3.2. It should be noted that GA maximizes objective function as they naturally seek the best fit. Thus the objective function computed by the GA is defined as the inverse of the least-square functional S(Q_K):

$$Z_{GA}(Q_K) = S(Q_K)^{-1} \tag{7.15}$$

The following suitable parameters are chosen to generate results: population size of 50 individuals/generation, a string of eight bits to define each parameter within each individual, one child per mating, a 4% probability of jump mutation, a 20% probability of creep mutation, and a 50% probability of crossover. This combination of parameters and procedures has been proven to yield efficient and accurate optimization results for different cases carried out in this study.

7.3 Numerical Results

The results of the inverse problem will be presented for two cases; the results for one cooling slot, and the results for two cooling slots. Again, the conjugate heat transfer (CHT) simulations presented in the third chapter will provide a numerical input to the inverse problem, the numerical results simulate measurements.

7.3.1 Results of the Inverse Problem for One Cooling Slot

Results are now presented for the inverse analysis of one cooling slots case. Each side of the solid (metal) block is analyzed as a separate domain for the BEM analysis. To ensure that the results are independent of the number of sinks, the results have been generated using six and ten singularities (sinks) distributed within the extended domain which in each case occupies the size of the slot itself. To achieve a grid independent solution, the one-cooling slot case is modeled with 47 and 62 boundary elements for the left block and 97 and 142 boundary elements for the right block. The genetic algorithm provided a global optimum for the strength of the six and ten uniformly distributed sinks after 200 generations for both the left and right blocks. Figure 7.5 shows the BEM discretization as well as a plot of the temperature contours and the heat flux vector field for the two blocks combined.

After the singularity strengths were optimized, the normal heat fluxes along the actual edges of the cooling slots were found in a post-processing stage by simply calculating heat flux vector components on internal points distributed inside the extended domain where the actual cooling slot edges are located. Figures 7.6 through 7.8 show the BEM/GA predicted normal heat fluxes along the left and right edges of the cooling slot in comparison with the CHT simulated normal heat fluxes. A summary of the least square errors at variable numbers of sinks and elements for both edges of the cooling slot are shown in Table 7.1. The results reveal good accuracy in predicting the heat flux distributions. It can be seen that a distribution of ten singularities (sinks) is suitable to reconstruct heat flux distributions along left and right edges of the cooling slot. Also, the results are grid independent with 62, 142 elements for the left and right edges, respectively; see Figure 7.8.

T: 297 299 301 303 305 307 309 311 313 315 317 319 321 323 325 327 329 331 333 335 337 339 341

Figure 7.5. BEM discretization and resulting temperature contour plot with heat flux vector field for the one cooling slot case.

(a) Left Edge (47 elements)   (b) Right Edge (97 elements)

Figure 7.6. Plot of the predicted heat flux compared to the CHT simulated heat flux along the walls of the one cooling slot case with six singularities (sinks).
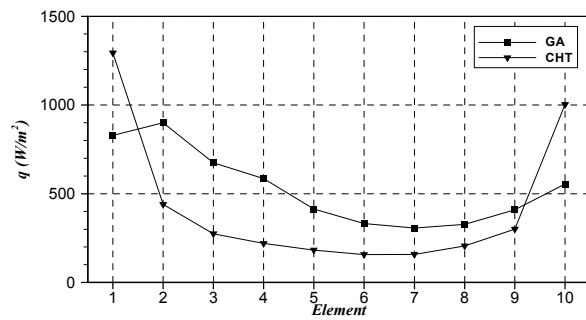
(a) Left Edge (47 elements)   (b) Right Edge (97 elements)

Figure 7.7. Plot of the predicted heat flux compared to the CHT simulated heat flux along the walls of the one cooling slot case with ten singularities (sinks).
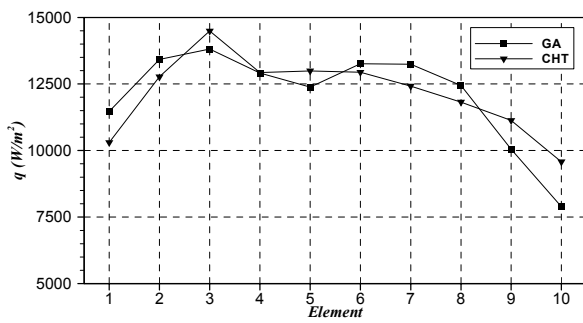
(a) Left Edge (62 elements)   (b) Right Edge (142 elements)
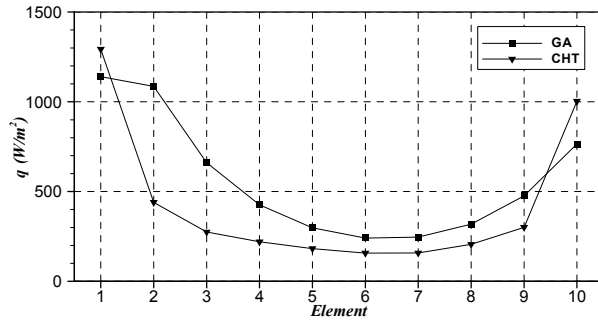
Figure 7.8. Plot of the predicted heat flux compared to the CHT simulated heat flux along the walls of the one cooling slot case with ten singularities (sinks).

Table 7.1. A summary for the least square errors (LSE) for the one cooling slot case.

Left Edge	LSE (W/m^2)	Right Edge	LSE (W/m^2)
$NS = 10, N = 62$	882.5	$NS = 10, N = 142$	269.1
$NS = 10, N = 47$	935.4	$NS = 10, N = 97$	276.0
$NS = 6, N = 47$	978.2	$NS = 6, N = 97$	324.8

7.3.2 Results of the Inverse Problem for Two Cooling Slots

The two-cooling slots case is modeled with 62 boundary elements for the left block, 69 boundary elements for the mid block, and 142 boundary elements for the right block. This number of elements ensure a grid independent solution. The genetic algorithm provided a global optimum for the strength of the 10 uniformly distributed sinks after 200 generations for the left, mid, and right blocks. Figure 7.9 shows the BEM discretization as well as the temperature contours and the heat flux vector field for the three blocks combined.

Again, the normal heat fluxes along the actual edges of the cooling slots were found in the post-processing stage after the singularity strengths were optimized. Figure 7.10 shows the BEM/GA predicted normal heat fluxes along the left and right edges of the first cooling slot in comparison with the CHT simulated normal heat fluxes, and Figure 7.11 shows the BEM/GA

predicted normal heat fluxes along the left and right edge of the first cooling slot in comparison
with the CHT simulated normal heat fluxes. Again, the results are in a good agreement with the
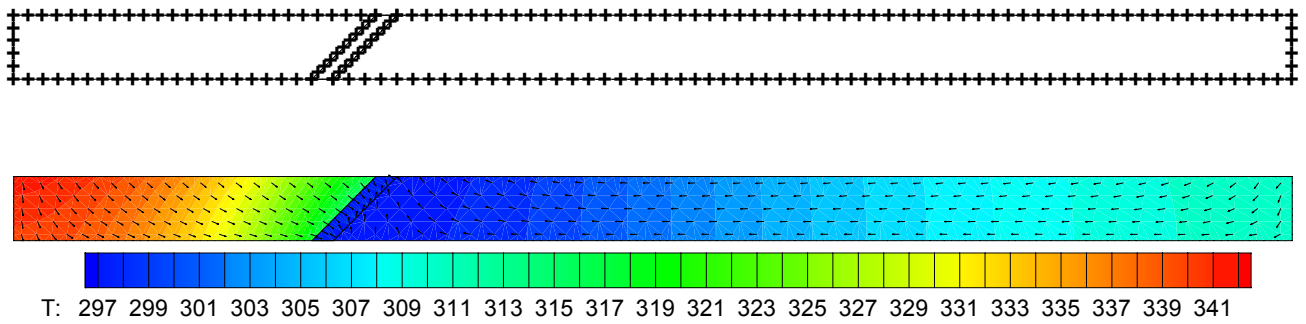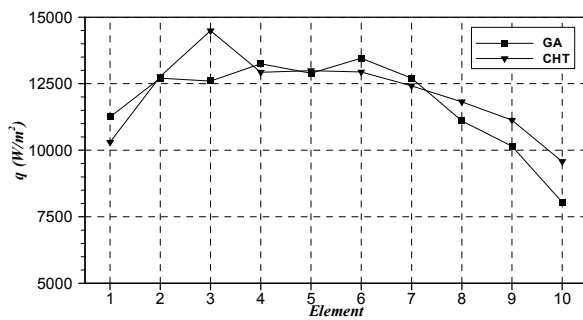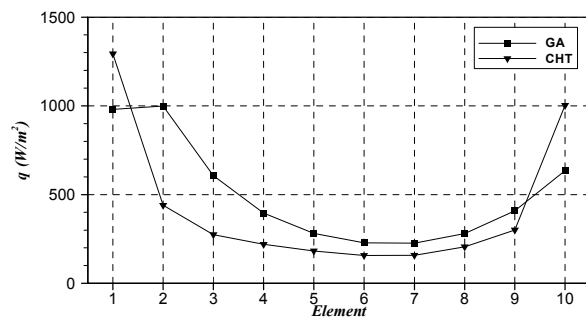CHT simulated heat fluxes.
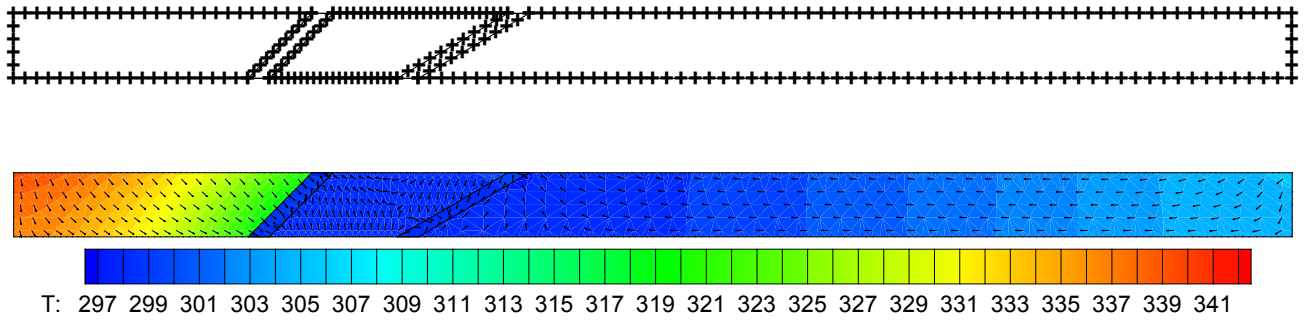
Figure 7.9. BEM discretization and resulting temperature contour plot with heat flux vector field
for the two cooling slots case.

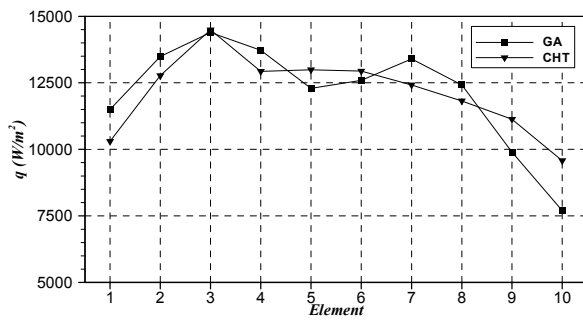(a) Left Edge   (b) Right Edge
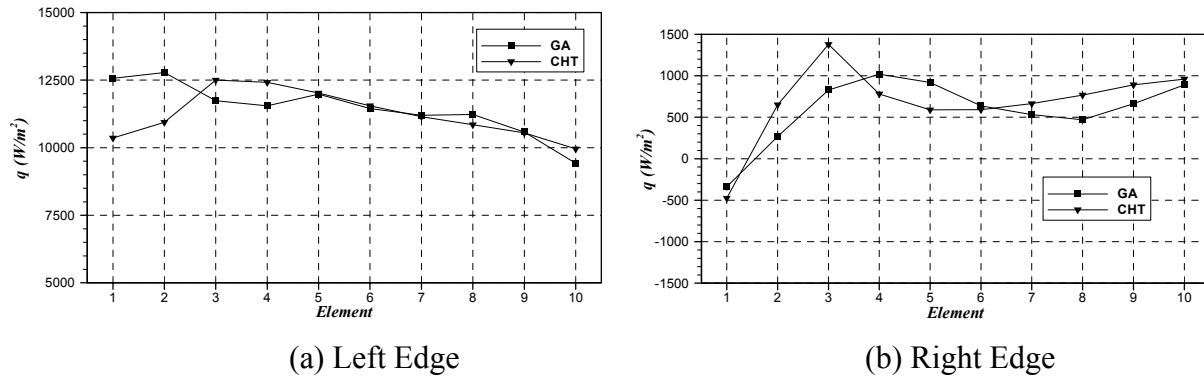
Figure 7.10. Plot of the predicted heat flux compared to the CHT simulated heat flux along the
walls of the first cooling slot with ten singularities (sinks).

(a) Left Edge   (b) Right Edge
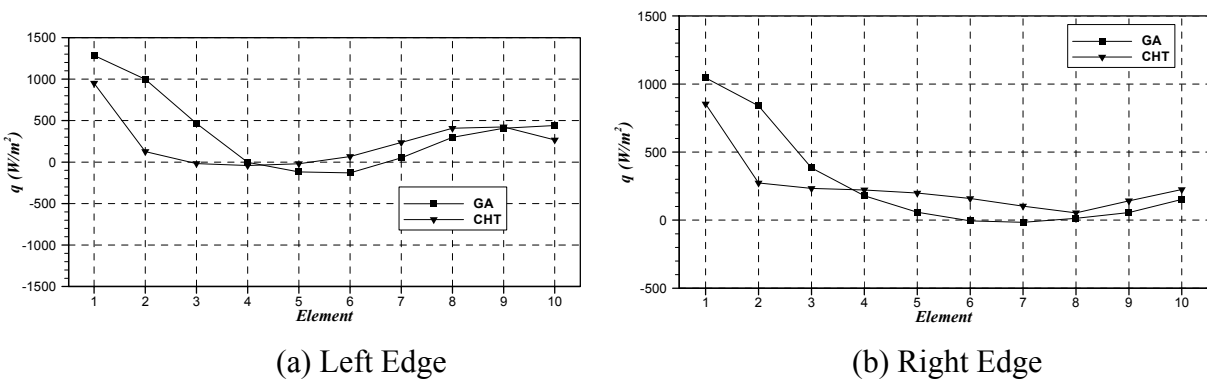
Figure 7.11. Plot of the predicted heat flux compared to the CHT simulated heat flux along the walls of the second cooling slot ten singularities (sinks).

In this chapter, a hybrid singularity superposition/boundary element-based inverse problem method for the reconstruction of multi-dimensional heat flux distributions was developed. Cauchy conditions are imposed at exposed surfaces that are readily reached for measurements while convective boundary conditions are unknown at surfaces that are not amenable to measurements such as the edges of cooling slots. The purpose of the inverse analysis is to determine the heat flux distribution along cooling slot edges. This is accomplished in an iterative process by distributing a set of singularities at the vicinity of the cooling slot surface inside a fictitious extension of the physical domain with a given initial strength distribution. A forward steady-state heat conduction problem is solved using the boundary element method (BEM), and an objective function is defined to measure the difference between the heat flux measured at the exposed surfaces and the heat flux predicted by the BEM under the current strength distribution of the singularities. A genetic algorithm iteratively alters the strength distribution of the singularities until the measuring surfaces heat fluxes are matched, thus satisfying Cauchy conditions. Subsequent to the solution of the inverse problem, the heat flux at the inaccessible surface is computed using the BEM. The hybrid singularity superposition/BEM approach thus eliminates the need to mesh the surface of the film cooling slot and the need to parametrize the heat flux over that surface. Rather, the heat flux is

determined in a post-processing stage after the inverse problem is solved. The results provided validate the approach and reveal agreement between the BEM/GA reconstructed heat fluxes and the CHT simulated heat fluxes along the inaccessible cooling slot walls.

Since this technique predicts agreement with the conjugate heat transfer (CHT) simulations for the 2D cases; i.e. one- and two-cooling slots, we extend this technique for three-dimensional applications. In the next chapter, a hybrid singularity superposition/boundary element-based inverse method for the reconstruction of heat flux distributions in film cooling holes will be developed. This technique will be applied with a vertical square cooling hole, and cylindrical cooling hole as test cases.

CHAPTER 8

SINGULARITY SUPERPOSITION/BEM INVERSE TECHNIQUE TO RECONSTRUCT HEAT FLUX DISTRIBUTIONS WITHIN FILM COOLING HOLES

8.1 Introduction

In the previous chapter, a hybrid singularity superposition/boundary element-based inverse problem method was developed to reconstruct heat flux distributions for the cases of one and two cooling slots. Here, this technique will be extended to 3D applications, and specifically to film cooling holes. The advantage of this technique is to eliminate the need of meshing the cooling holes, which requires a large amount of effort to achieve a high quality mesh. Moreover, the use of singularity distributions significantly reduces the number of parameters sought in the inverse problem. In this technique the inlets and the exits of the cooling holes will be assigned as an adiabatic boundary condition and a distribution of singularities (sinks) will be located inside the physical boundaries of each cooling hole (usually along cooling hole centerline) with a given initial strength distribution. A forward steady-state heat conduction problem is solved using the boundary element method (BEM), and an objective function is defined to measure the difference between the heat flux measured at the exposed surfaces and the heat flux predicted by the BEM under the current strength distribution of the singularities. A Genetic algorithm (GA) iteratively alters the strength distribution of the singularities until the measuring surfaces heat fluxes are matched, thus satisfying Cauchy conditions. Subsequent to the solution of the inverse problem, the heat flux at the inaccessible surfaces is computed using BEM. The distribution of the heat flux at the walls of the cooling hole is determined in a post-processing stage after the inverse problem is solved. Again, this constitutes a tremendous advantage in solving the inverse problem, particularly in the application of film cooling holes.

8.2 Singularity Superposition and Inverse Problem Methodology

Considering the case of a 3D film cooling hole supplied by a plenum, see Figure. 8.1(a). The model consists of the hot gas domain, the coolant plenum supply (cold air), and the endwall with single square/circular cooling hole. The measured temperature and heat flux at over-specified surfaces (red color) are shown in Fig. 8.1(b), will be used as an input for the inverse problem to determine the distributions of the temperature and heat flux along the film-cooling hole walls. Also, the sides of the endwall in addition to the inlet and the exit surfaces of the cooling hole are set to be an adiabatic.

The inverse problem algorithm developed herein is similar to the one developed in the previous chapter. Again, this methodology comprised of the forward problem solver: a hybrid singular superposition/BEM method, and an inverse problem solver: genetic algorithm to determine strength distribution of the sinks to match Cauchy conditions imposed at exposed surfaces.
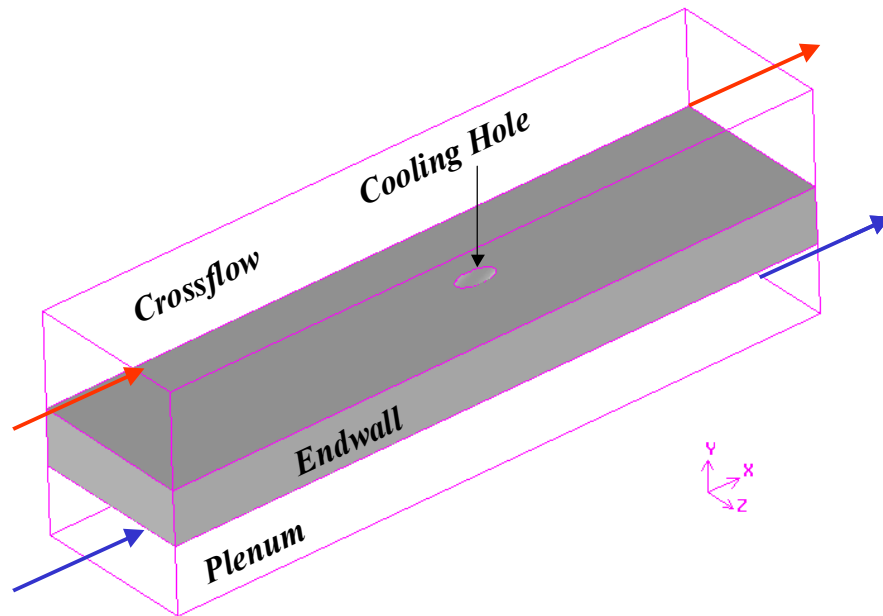
(a) overall configuration.
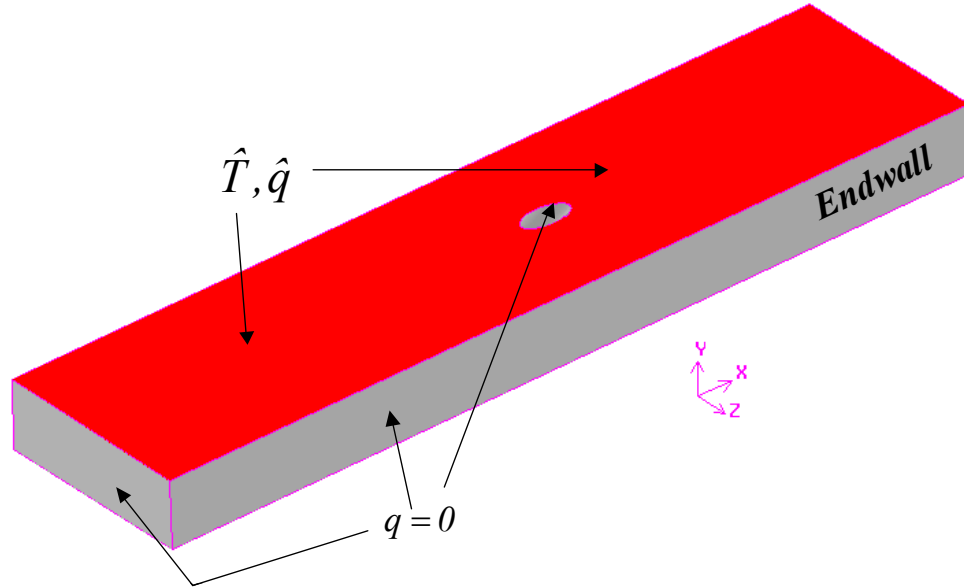
(b) domain of the inverse conduction problem.

Figure 8.1. Schematic diagram for the Inverse Problem.

8.2.1 The Forward Problem Solver

The purpose of the inverse problem is to determine the heat flux distribution (q) at the walls of the cooling hole. This is accomplished in an iterative process. The temperature is imposed at the exposed surfaces (top/bottom surfaces of the endwall), and to simulate the extraction of energy from the coolant, a distribution of singularities (sinks) is located in the vicinity of the cooling hole surfaces within the hole physical domain with a given initial strength distribution, see Figure 8.2, usually, the sinks will be located along the cooling hole centerline. The inlet and the exit surfaces of the cooling hole will be insulated to prevent energy from flowing through them, this way all the energy that was extracted through the physical cooling surface is captured by the sinks.

•Top/Bottom Surfaces: Cauchy Conditions

• Gray Surfaces: Adiabatic Conditions

• Blue Line/Dots: Location of Singularities
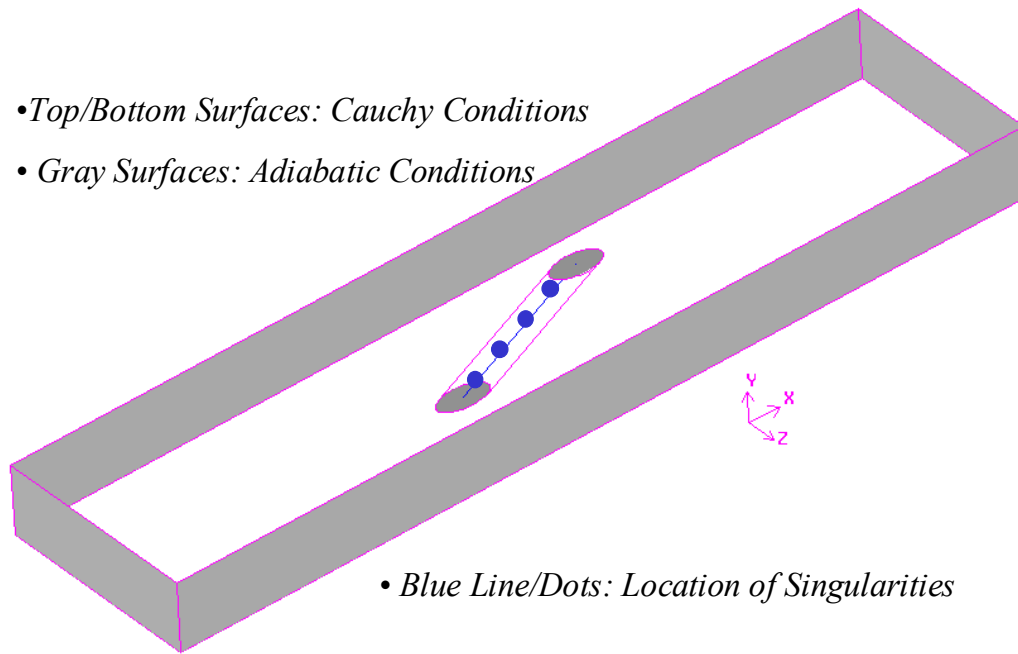
Figure 8.2. Thermal singularity superposition configuration.

The mathematical formulation of the 3D case is similar to the 2D case by extending the governing equations from two-dimensions to three-dimensions. The Poisson equation for the temperature $T(x, y, z)$ is:

$$\nabla.[k\nabla T(x,y,z)] + \sum_{K=1}^{NS} Q_K \delta(x,y,z,x_K,y_K,z_K) = 0 \qquad (8.1)$$

where the generation term is the summation of singular field perturbations characterized by the number of singularities/sinks (NS) localized Dirac delta functions, k is the thermal conductivity ($W/m.K$), Q_K represents the strength of the sinks, (x_K, y_K, z_K) represents location of the Kth sink, and δ is Dirac delta function. Again, the boundary elements method (BEM) approach is adopted to solve this problem. A standard BEM formulation starts with the introduction of an arbitrary function $G(x, y, z, x_i, y_i, z_i)$ and a transformation of the governing equation into an integral equation over the domain Ω as:

$$\int_{\Omega} \nabla.[k\nabla T(x,y,z)]G(x,y,z,x_i,y_i,z_i)d\Omega = \tag{8.2}$$

$$\sum_{K=1}^{NS} Q_K \int_{\Omega} \delta(x,y,z,x_K,y_K,z_K)G(x,y,z,x_i,y_i,z_i)d\Omega$$

To transform the domain integral into contour integrals over the boundary (Γ); Green's second identity is applied on the left-hand side and the sifting property of the Dirac delta function is applied on the right-hand side of the equation above yielding:

$$\int_{\Omega} \nabla.[k\nabla G(x,y,z,x_i,y_i,z_i)]\,T(x,y,z)\,d\Omega + \tag{8.3}$$

$$\oint_{\Gamma} H(x,y,z,x_i,y_i,z_i)\,T(x,y,z)\,d\Omega - \oint G(x,y,z,x_i,y_i,z_i)\,q(x,y,z)\,d\Gamma =$$

$$\sum_{K=1}^{NS} Q_K\,G(x_K,y_K,z_K,x_i,y_i,z_i)$$

where:

$$H(x,y,z,x_i,y_i,z_i) = -k\,\partial G(x,y,z,x_i,y_i,z_i)/\partial n \tag{8.4}$$
$$q(x,y,z) = -k\partial T(x,y,z)/\partial n$$

Now, a Dirac delta function is used to perturb the adjoint operator on the arbitrary function $G(x,y,z,x_i,y_i,z_i)$ present in the last remaining domain integral in the equation as:

$$\nabla.[k\nabla G(x,y,z,x_i,y_i,z_i)] = -\delta(x,y,z,x_i,y_i,z_i) \tag{8.5}$$

For 3D problems $G(x,y,z,x_i,y_i,z_i)$ can be found as the free-space solution to the adjoint equation as:

$$G(x,y,z,x_i,y_i,z_i) = \frac{1}{4\pi k\sqrt{(x-x_i)^2 + (y-y_i)^2 + (z-z_i)^2}} \tag{8.6}$$

Again, the sifting property of the Dirac delta function is recasted to lead to the following boundary-only integral equation:

$$C(x_i, y_i, z_i)\, T(x_i, y_i, z_i) - \oint_\Gamma T(x, y, z) H(x, y, z, x_i, y_i, z_i) d\Gamma + \tag{8.7}$$

$$\oint_\Gamma q(x, y, z)\, G(x, y, z, x_i, y_i, z_i) d\Gamma = \sum_{K=1}^{NS} Q_K\, G(x_K, y_K, z_K, x_i, y_i, z_i)$$

Introducing boundary discretization yields the following relation:

$$C_i\, T_i - \sum_{j=1}^{N} \widehat{H}_{ij}\, T_j + \sum_{j=1}^{N} G_{ij}\, q_j = \sum_{K=1}^{NS} Q_K\, G(x_K, y_K, z_K, x_i, y_i, z_i) \tag{8.8}$$

where:

$$
\begin{aligned}
C_i &= 1 \ \text{if } (x_i, y_i, z_i) \in \Omega \\
C_i &= \frac{1}{2} \ \text{if } (x_i, y_i, z_i) \in \Gamma \text{ (smooth boundaries)} \\
C_i &= 0 \ \text{if } (x_i, y_i, z_i) \notin \Omega
\end{aligned}
\tag{8.9}
$$

Following the discretization of the boundary (Γ) with (N) nodal locations and the collocation of (x_i, y_i, z_i) at these (N) locations, the above equation reduces to the following simultaneous set:

$$\sum_{j=1}^{N} G_{ij}\, q_j - \sum_{j=1}^{N} H_{ij}\, T_j = S_i \tag{8.10}$$

where:

$$H_{ij} = \widehat{H}_{ij} - \frac{1}{2}\delta_{ij} \tag{8.11}$$

$$S_i = \sum_{K=1}^{NS} Q_K\, G(x_K, y_K, z_K, x_i, y_i, z_i)$$

In this case, constant boundary elements were used, see [140]. The strength of singularities can be estimated by carrying out an energy balance over the domain of the inverse problem (endwall) which yields to Equation (8.1), then integrating Equation (8.1) over the domain (Ω) yields the following relations:

$$\int_\Omega \nabla.[k\nabla T(x,y,z)]d\Omega + \sum_{K=1}^{NS} Q_K \int_\Omega \delta(x,y,z,x_K,y_K,z_K)d\Omega = 0 \qquad (8.12)$$

$$\oint_\Gamma k\nabla T(x,y,z).\vec{n}d\Gamma + \sum_{K=1}^{NS} Q_K = 0 \qquad (8.13)$$

$$-\oint_\Gamma q_n d\Gamma + \sum_{K=1}^{NS} Q_K = 0 \qquad (8.14)$$

or

$$\sum_{K=1}^{NS} Q_K = \oint_\Gamma q_n d\Gamma = \sum_{\Gamma_W} q_n A_{\Gamma_W} = \sum_{\Gamma_i} q_n A_{\Gamma i} \qquad (8.15)$$

where A is the surface area of the each boundary, Γ_W are the wall boundaries of the cooling hole, and Γ_i are the surface boundaries for the domain of the inverse problem. Provided that a well-posed problem is conformed with a properly defined geometry and set of boundary conditions, see Figure 8.3, the discretized boundary integral equation, Equation. (8.10) is reduced to:

$$A_{ij} x_j = b_i + S_i \qquad (8.16)$$

with $i = 1...N$ and where S_i contains the effects of the added singularities Q_K. The solution to this system provides the full distribution of temperatures and heat fluxes around the boundary that can later be used in the same formulation to calculate temperatures and heat fluxes anywhere in the domain Ω. Notice that the system in Equation (8.16) needs to be generated and LU-decomposed only once, and changing the strength of the singularities can be efficiently accounted for in the solution by just updating the right-hand side vector and solving the system again by a forward and back substitution.

- *Top/Bottom Surfaces: First type boundary (Temperature)*
- *Gray Surfaces: Adiabatic Conditions*
- *Blue Line/Dots: Location of Singularities*
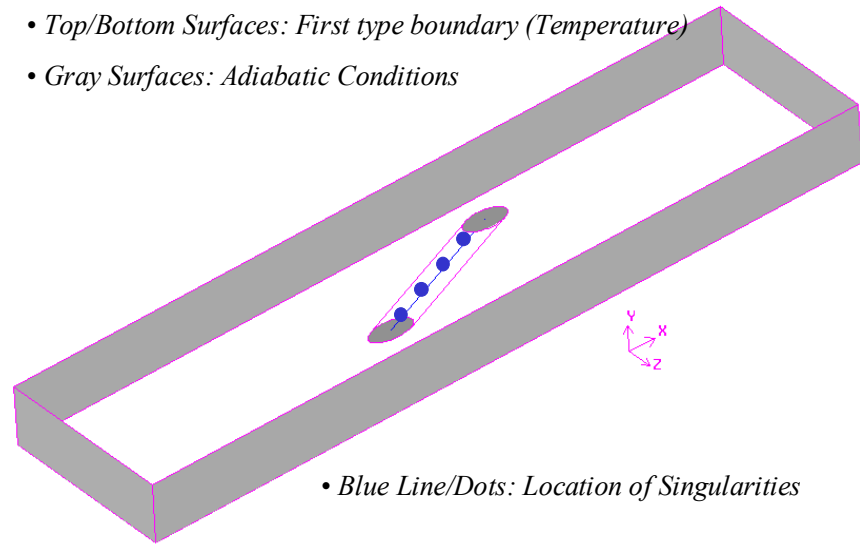
Figure 8.3. Set of boundary conditions for the BEM problem.

8.2.2 The Inverse Problem Solution

The purpose of the inverse problem is to determine the heat flux distributions at the surfaces/walls of the film cooling hole. This is done in an iterative process; the temperature is imposed at exposed surfaces (top/bottom surfaces) and a distribution of singularites (sinks) is located within the physical domain of the cooling hole (along cooling hole center line) with a given initial strength distribution. A forward steady-state heat conduction problem is solved using the boundary element method (BEM), and an objective function is defined to measure the difference between the heat flux measured at the exposed surfaces and the heat flux predicted by the BEM under current strength distribution of the sinks. This can be accomplished by minimizing the following least-squares functional:

$$S(Q_K) = \sqrt{\Big(\sum_{i=1}^{N_m} R_i\Big)\Big(\frac{1}{N_m}\sum_{i=1}^{N_m} \frac{\big[q_i(Q_K) - \widehat{q}_i\big]^2}{R_i}\Big)} \qquad (8.16)$$

where N_m is the number of measuring points, $\widehat{q}_i$ are the measured heat fluxes at the measuring points, and $q_i(Q_K)$ are the computed heat fluxes for a given set of sink strengths, R_i is defined to measure the smallest distance between any element and the location of the singularities (sinks); i.e. R_i is equal to the minimum of either $R1_i$ or $R2_i$, where $R1_i$ and $R2_i$ are defined as follows:

$$R1_i = (x_{ci} - x_{exit})^2 + (y_{ci} - y_{exit})^2 + (z_{ci} - z_{exit})^2$$
$$R2_i = (x_{ci} - x_{inlet})^2 + (y_{ci} - y_{inlet})^2 + (z_{ci} - z_{inlet})^2 \qquad (8.17)$$

where (x_{ci}, y_{ci}, z_{ci}) are the coordinates of the center of the i-th element, $(x_{inlet}, y_{inlet}, z_{inlet})$ is the physical center of the cooling hole inlet, and $(x_{exit}, y_{exit}, z_{exit})$ is the physical center of the cooling hole exit. As we mentioned before that the inherent regularization property of the genetic algorithms (minimization method of choice in this study), in addition to the discrete nature of a finite number of singularities (sinks) to simulate the extracted energy, makes it unnecessary to add any additional regularization to the functional, and would just slow down the minimization process. Once the functional, $S(Q_K)$, is minimized, the resulting heat flux distribution along the physical walls of the film cooling hole can be smoothed-out by simple least-squares means. Moreover, the calculation of the normal heat fluxes at the walls of the cooling hole (four lines, one line per side) is done at a post-processing stage by computing the heat flux vector components at internal points along the walls of the cooling hole (4-lines).

8.2.3 The Genetic Algorithm

Again, the optimization technique is chosen to be the genetic algorithm (GA), for more details see section 6.3.2. As we mentioned before that GA maximizes objective function as they naturally seek the best fit. Thus the objective function computed by GA is defined as the inverse of the least-square functional $S(Q_K)$:

$$Z_{GA}(Q_K) = S(Q_K)^{-1} \qquad (8.18)$$

The following suitable parameters were chosen to generate results: a population size of 50 individuals/generation, a string of eight bits to define each parameter within each individual. The mating process produces one child per mating using uniform crossover which produces a higher level of diversity than single point crossover, a 4 % probability of jump mutation, a 20% probability of creep mutation, and a 50% probability of crossover. The population is not allowed to grow (static population) and elitistic generation (the best parent survives to the next generation). The population is completely eliminated after 50 generations if there is no further improvement, keeping the best number of the population (restart). This combination of parameters and procedures has been proven to yield efficient and accurate optimization results for different cases carried out in this study.

8.3 Numerical Results

The results of the inverse problem are presented for two cases: the results for single square cooling hole, and the results for single circular cooling hole. For the case of a square cooling hole, a forward problem is solved using the BEM first to generate boundary conditions at the exposed surfaces (top/bottom surfaces), those are in turn used to simulate inputs to the inverse problem. In contrast, for the case of the circular hole, a full conjugate heat transfer (CHT) model is developed to simulate the experimentally measured data at the exposed surfaces, which will provide a numerical input for the inverse problem.

8.3.1 Results of the Inverse Problem for Square Cooling Hole

First, a solution to the forward problem will be established to used in obtaining heat flux measurements which serves to simulate a numerical input to the inverse problem. In specific,

116

consider a rectangular endwall (($x = 11cm$) × ($y = 21cm$) × ($z = 3cm$)) with a vertical square cooling hole located at the geometrical center of the endwall, the cross-sectional area of the cooling hole is ($1cm \times 1cm$). The problem is discretised using (($Nx = 11$) × ($Ny = 21$) × ($Nz = 3$)) constant elements for the endwall and (($Nh = 1$) × ($Nh = 1$)) for the cooling hole, the total number of elements is calculated according to the following relation:

$$N = 2(NxNy + NxNz + NyNz) + 4NzNh - 2NhNh \qquad (8.19)$$

Based on the above relation the total number of elements for the direct problem is 664 constant elements. The geometry, the BEM discretization, and the boundary condition definitions are shown in Figure 8.4: notice that the temperate is in units of (K) and the heat transfer coefficient is in units of (W/m^2K). The endwall material is stainless steel with a constant thermal conductivity of ($k = 14.9\,W/m.K$)
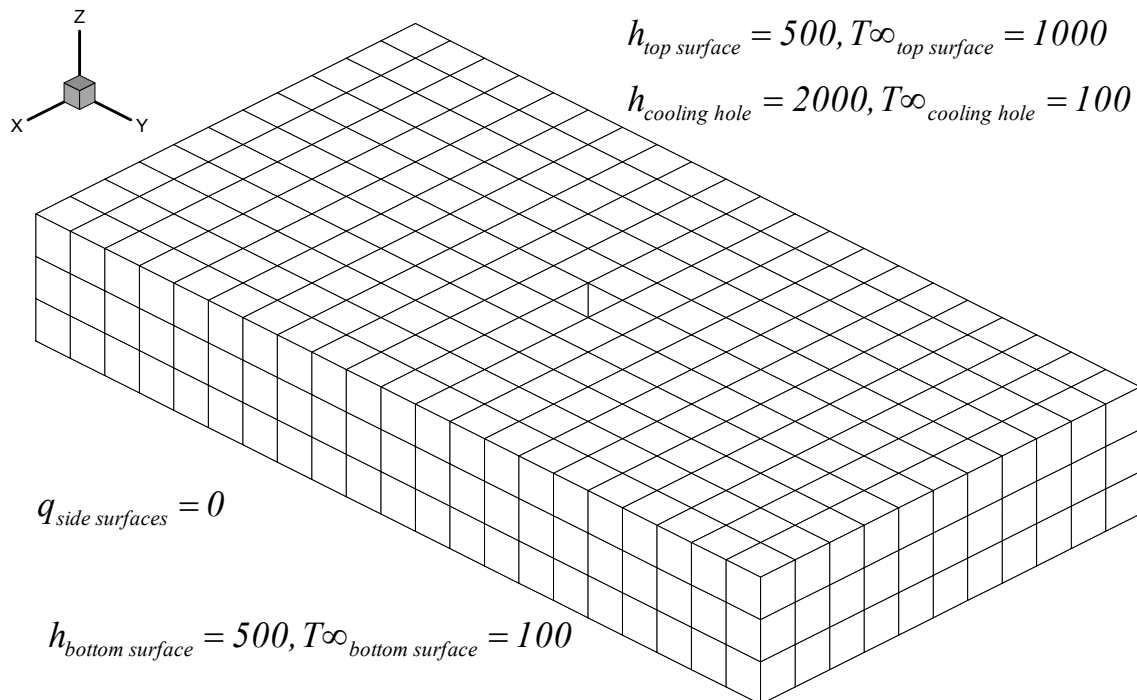
Figure 8.4. Geometry, BEM mesh, and boundary conditions used in solving the forward problem of a vertical square hole.

The discretized governing equations with the specified boundary conditions have been solved, and the temperature distribution is shown in the Figure 8.5, it can be seen that the temperature expands from $200°K$ to $680°K$.
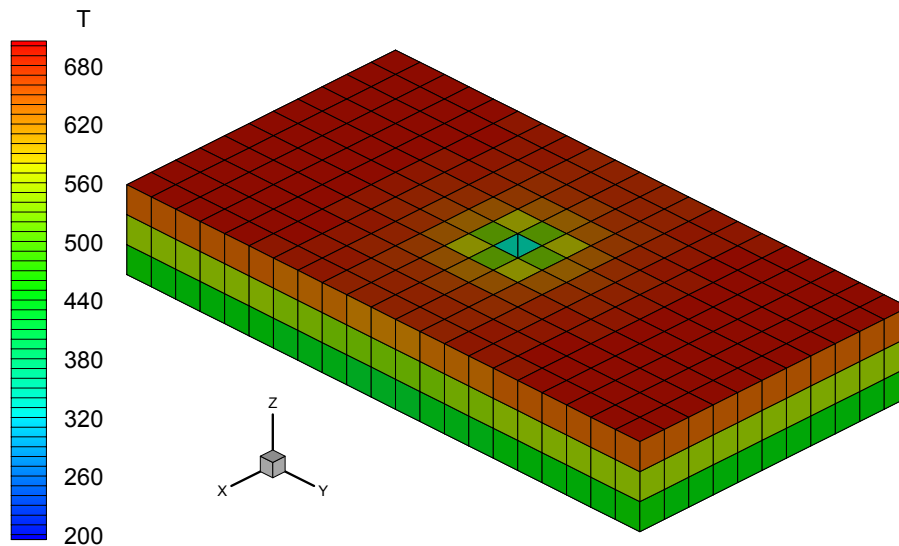
Figure 8.5. Temperature distributions for case of vertical square cooling hole predicted by the BEM direct solution.

The inverse problem had been solved just for the rectangular endwall without the square cooling hole in it, the same discretization was used in the direct problem is applied in the inverse problem which gives a total number of 654 constant elements; i.e. $((2 \times 11 \times 21) + (2 \times 11 \times 3) + (2 \times 21 \times 3))$. The boundary conditions along the sides of the endwall are adiabatic, whereas Cauchy conditions which were obtained from the direct solution are applied at the top and the bottom surfaces. The inlet and the exit surfaces of the cooling hole are set to an adiabatic boundary condition to ensure that all energy extracted by the cooling hole is captured by the sinks. In this case, the sinks are located at the geometrical center of the cooling hole. A distribution of three sinks were found to be a suitable number to have an optimized solution. An initial guess of the strength of sinks (Q_K) is set to be between $- 400$

and zero (W/m^2) to begin the minimization process. The genetic algorithm provided a global optimum for the strength of the three uniformly distributed sinks after 600 generations with a best fitness of 0.0725. Figure 8.6 shows the BEM discretization as well as the temperature contour plot field along the endwall.
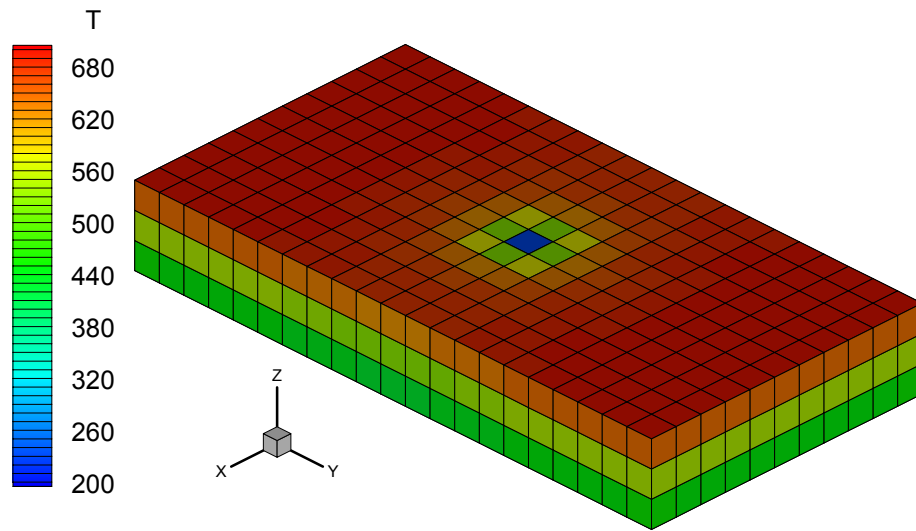
Figure 8.6. BEM discretization and resulting temperature contour plot for the case of a vertical square cooling hole predicted by the inverse solution.

After the singularity strengths were optimized, the normal heat fluxes along the actual walls of the cooling hole were found in a post-processing stage by calculating heat flux vector components on internal points distributed along each side of the actual walls of the cooling hole. Because of problem symmetry, the GA predicted temperatures and heat fluxes can be compared to the direct solution along one side of the cooling hole. Figures 8.7 and 8.8 shows the BEM/GA reconstructed temperature and normal heat fluxes along one side/wall of the square cooling hole in comparison with the direct simulated temperature and normal heat fluxes. The results reveal good accuracy in predicting the temperature and heat flux distributions. It can be seen that a

distribution of three singularities (sinks) is quite good to reconstruct heat flux distributions along the sides of the square cooling hole.

Figure 8.7. Plot of GA predicted temperature compared to the direct simulated temperature along one side of the vertical square cooling hole.
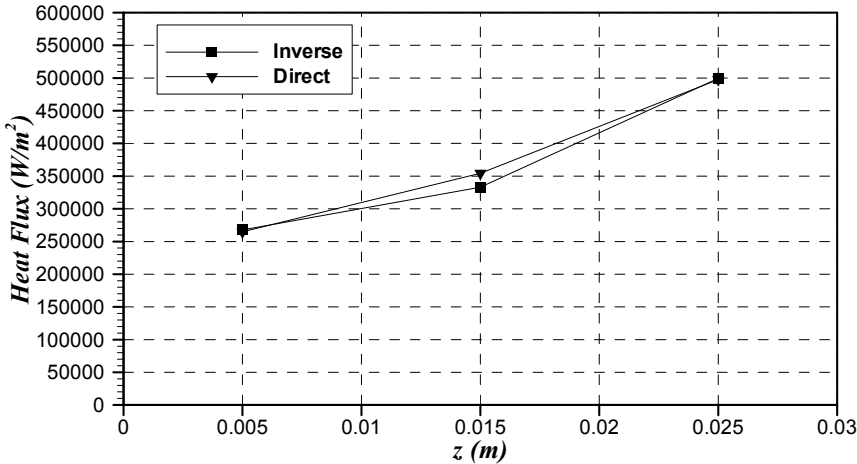
Figure 8.8. Plot of the GA predicted heat flux compared to the direct simulated heat flux along one side of the vertical square cooling hole.

8.3.2 Results of the Inverse Problem for Circular Cooling Hole

For the case of the circular hole, a full conjugate heat transfer (CHT) model is developed to simulate the experimentally measured data at the exposed surfaces, which provides a numerical input for the inverse problem. More details about the conjugate heat transfer simulations are explained in chapter four. In this case, the endwall dimensions are $((x = 50cm) \times (y = 3cm) \times (z = 9cm))$ with single circular cooling hole. The cooling hole has a diameter of $(D = 1cm)$ with an injection angle of 30° with the axial direction. Here, the conjugate heat transfer simulations were modeled using a linear model for the thermal conductivity $(k = 16.63 \, W/m.K)$. Since the mesh for CHT model is different from the BEM mesh, the CHT simulated temperatures and heat fluxes were interpolated from the CHT mesh to BEM mesh using radial basis functions (RBF) interpolation with 20 points. The inverse problem is modeled using a discretization of 1254 constant elements; i.e. $((2 \times 50 \times 90) + (2 \times 50 \times 3) + (2 \times 9 \times 3))$. The CHT mesh and the BEM mesh are shown in Figure 8.9.
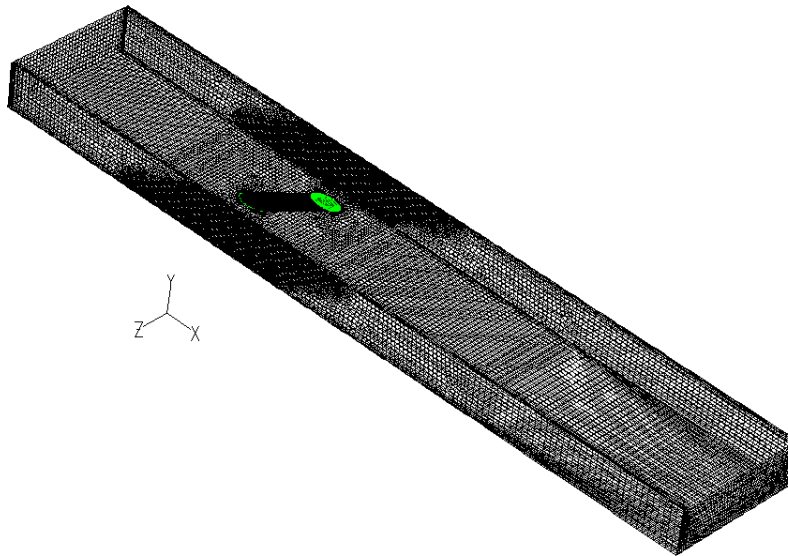
(a) CHT mesh
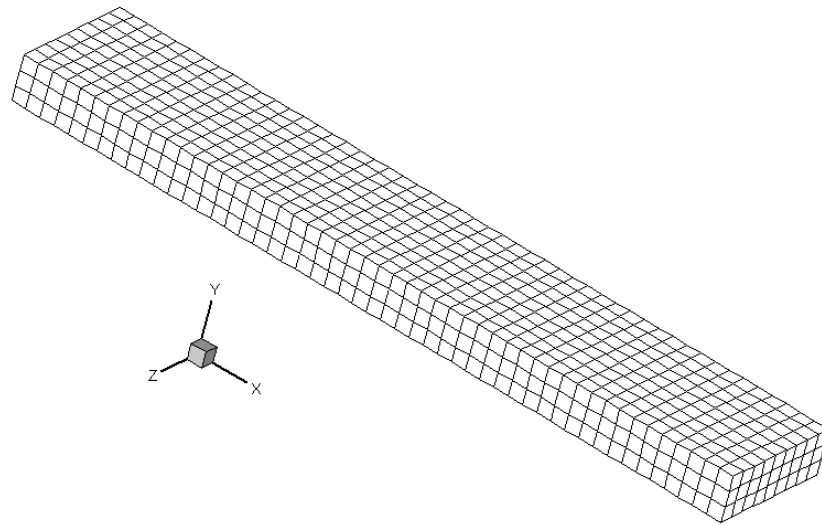
(b) BEM mesh

Figure 8.9. A plot of CHT mesh and the BEM mesh used for solving the circular cooling hole.

The inverse problem was solved using a distribution of 20 singularities (sinks). Those sinks were distributed along five lines such that there are four sinks per line. The optimum location of the lines were found to be one line at the geometrical center of the circular hole, whereas, the other four lines were located by offsetting the centerline by a distance of $(D/4)$ in the four sides, as shown in Figure 8.10. An initial guess of the strength of sinks (Q_K) is set to be between -200 and 200 (W/m^2) to begin the minimization process.
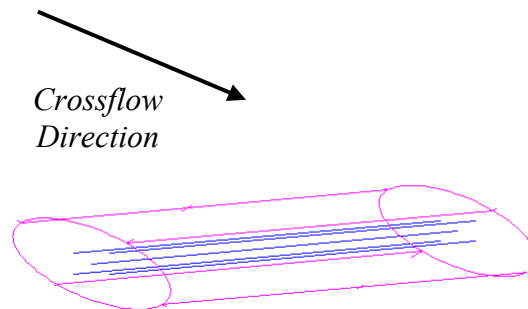
Figure 8.10. Location of the 20 singularities (sinks) along the five lines (blue) used for solving the inverse problem of circular cooling hole.

The genetic algorithm provided a global optimum for the strength of the twenty uniformly distributed sinks after 2000 generations with a best fitness of 0.00156. Figure 8.6 shows a temperature contours predicted by both the CHT simulation as well as the GA solution.
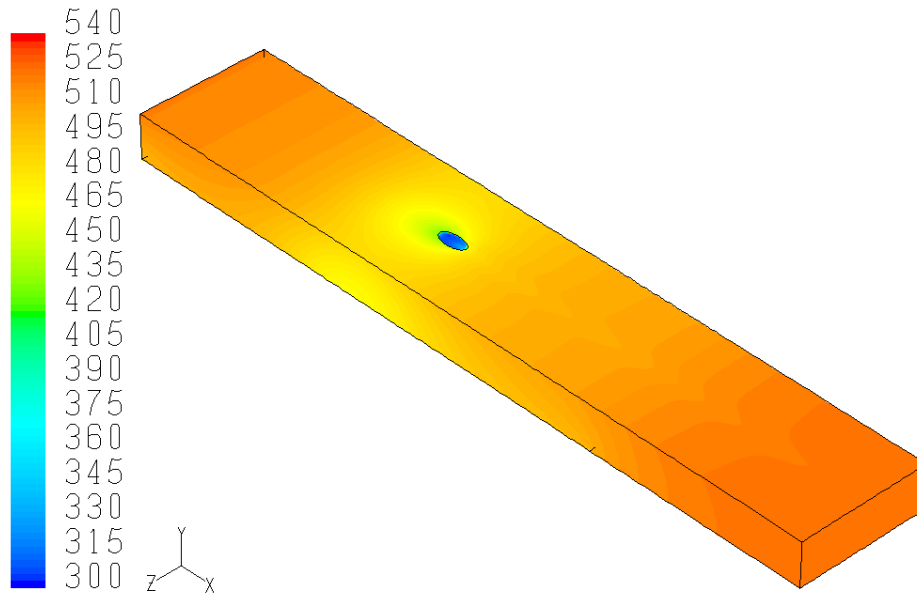
(a) CHT solution
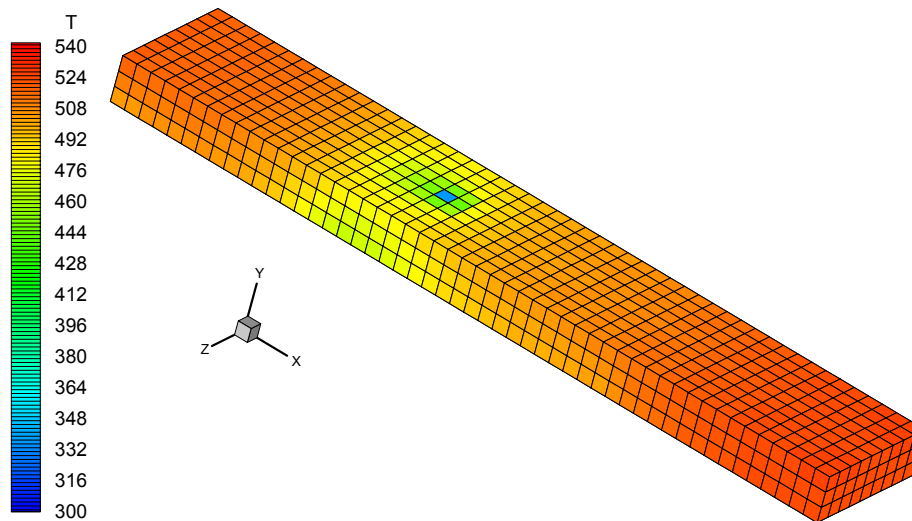
(B) GA solution

Figure 8.11. A plot of the temperature contours predicted by both CHT and GA solutions for circular cooling hole.

Again, after the singularity strengths were optimized, the normal heat fluxes along the actual walls of the cooling hole were found in a post-processing stage by calculating heat flux vector components on internal points distributed along each side of the actual walls of the cooling hole. In this case, the GA reconstructed temperatures and heat fluxes were compared to the CHT simulated ones along four lines; Line-1 through Line-4, located at the physical walls of the cooling hole as shown in Figure 8.12. Figures 8.13 and 8.14 shows the BEM/GA reconstructed temperature and normal heat fluxes along the four lines/edges of the circular cooling hole in comparison with the CHT simulated temperature and normal heat fluxes. The results reveal good accuracy in predicting the temperature and heat flux distributions. It can be seen that a distributions of twenty singularities (sinks) along five lines is good enough to reconstruct heat flux distributions along the sides of the circular cooling hole.
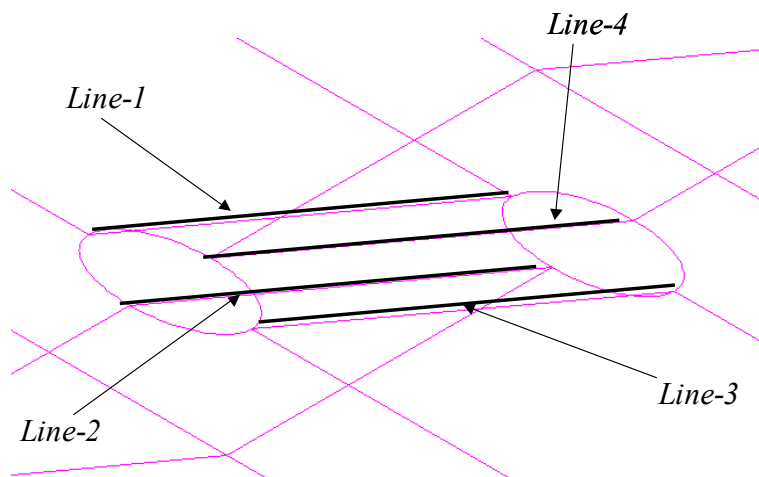
Figure 8.12. Location of the four lines/edges used to compare the GA predicted results to the CHT simulated ones for the case of circular cooling hole.
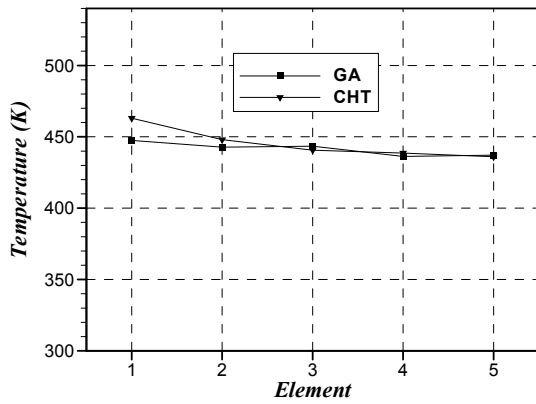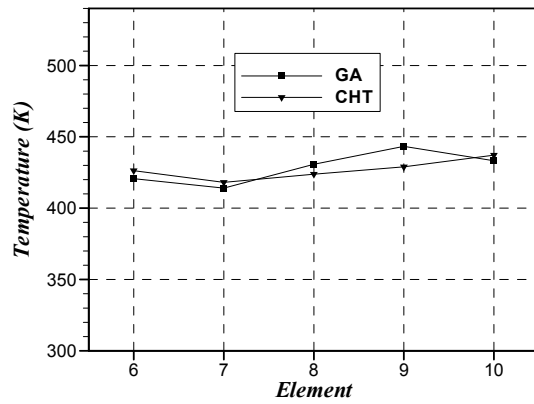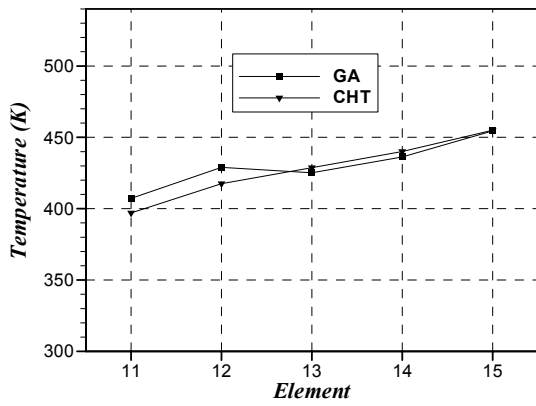
(a) *Line-1*   (b) *Line-2*

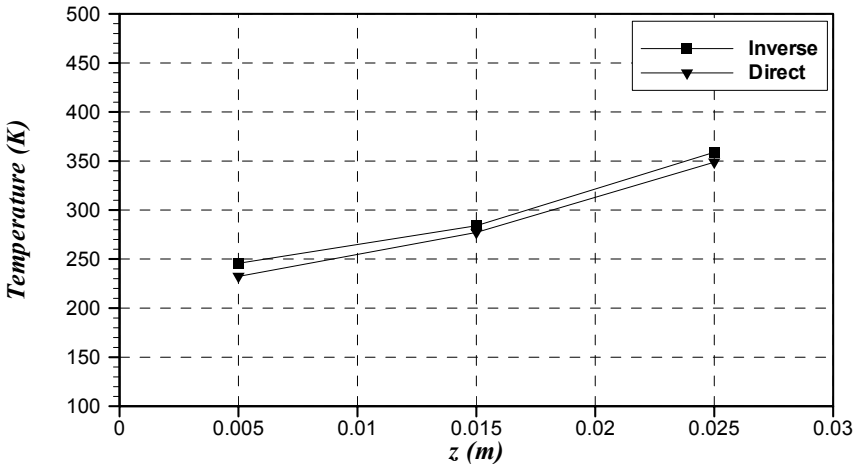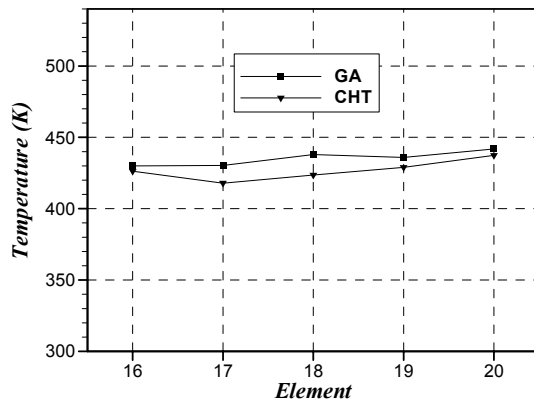(c) *Line-3*   (d) *Line-4*

Figure 8.13. Plot of GA predicted temperature compared to the CHT simulated temperature along four lines for the case of circular cooling hole.
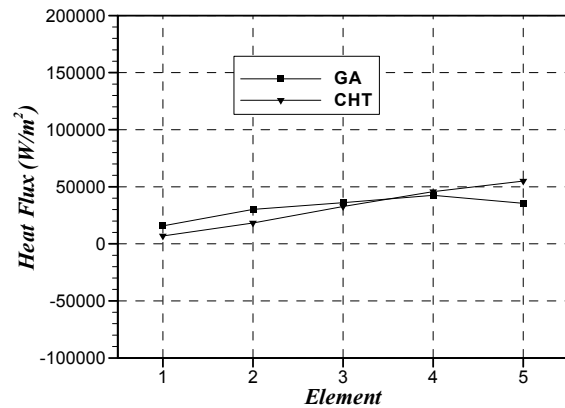
(a) *Line-1*   (b) *Line-2*
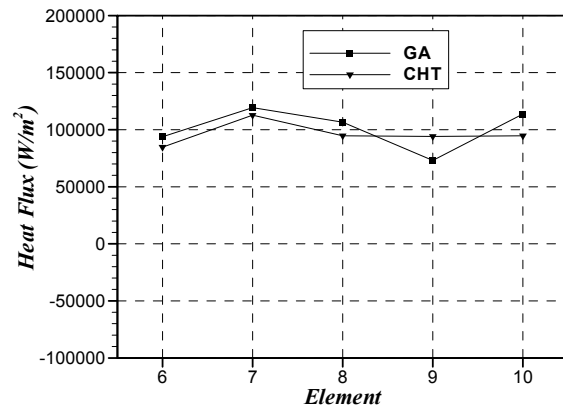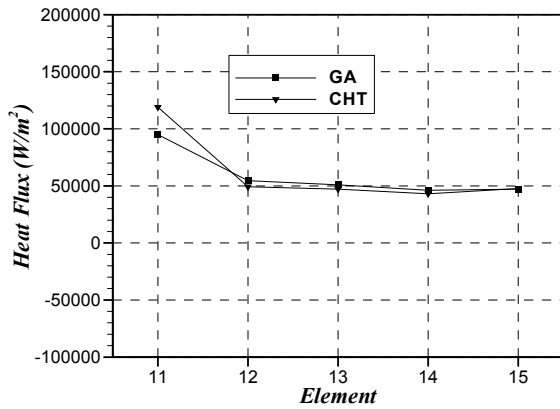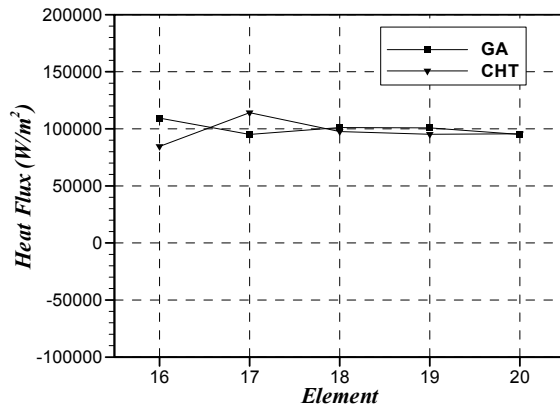
(c) *Line-3*   (d) *Line-4*

Figure 8.14. Plot of GA predicted temperature compared to the CHT simulated temperature along four lines for the case of circular cooling hole.

In this chapter, a hybrid singularity superposition/boundary element-based inverse problem method for the reconstruction of 3D heat flux distributions was developed. Cauchy conditions are imposed at exposed surfaces that are readily reached for measurements while convective boundary conditions are unknown at surfaces that are not amenable to measurements such as the walls of cooling holes. The purpose of the inverse analysis is to determine the heat flux distribution along edges/walls of the cooling holes. This is accomplished in an iterative process by distributing a set of singularities at the vicinity of the cooling hole surfaces along the cooling hole centerline with a given initial strength distribution. A forward steady-state heat conduction problem is solved using the boundary element method (BEM), and an objective function is defined to measure the difference between the heat flux measured at the exposed surfaces and the heat flux predicted by the BEM under the current strength distribution of the singularities. A genetic algorithm iteratively alters the strength distribution of the singularities until the measuring surfaces heat fluxes are matched, thus, satisfying Cauchy conditions. The hybrid singularity superposition/BEM approach thus eliminates the need to mesh the surfaces of the film cooling hole and the need to parametrize the heat flux over that surface. Rather, the heat

126

flux is determined in a post-processing stage after the inverse problem is solved. The results provided validate the approach and reveal good accuracy between the BEM/GA predicted heat fluxes and the CHT simulated heat fluxes along the inaccessible cooling hole walls.

Once the heat flux distributions are determined, it is the practice in heat transfer to report the result by defining the local film coefficient (h_x) as the local heat flux normalized with respect to an appropriate reference temperature. The resulting film coefficient distributions are then fit to a correlations reflecting dependency on position, the Prandtl and Reynolds numbers, which will be the subject of the next chapter.

CHAPTER 9

CORRELATING HEAT TRANSFER COEFFICIENTS

9.1 Introduction

Once the heat flux distributions are determined, it is the practice in heat transfer to report the result by defining the local film coefficients (h_x) as the local heat flux normalized with respect to an appropriate reference temperature as:

$$h_x = \frac{q_{w,x}}{(T_{wall,x} - T_{ref})} \tag{9.1}$$

where h_x is the local heat transfer coefficient ($W/m^2.K$), $q_{w,x}$ is local wall heat flux (W/m^2), $T_{wall,x}$ is local wall temperature (K), and T_{ref} is a reference temperature (K). The reference temperature can be defined as the fluid bulk temperature, or the adiabatic wall temperature. In this study, we set the reference temperature to be equal to the fluid bulk temperature at the cooling slot/slot inlet which is amenable to measurements. The dependency of the local heat transfer coefficient on the relevant dimensionless parameters is readily found from dimensional analysis to be:

$$h_x = f(Re_x, Pr) = \frac{Nu_x k}{D} \tag{9.2}$$

where Re_x is the local Reynolds number, k is thermal conductivity for fluid (air), Pr is Prandtl number which is equal to 0.72 for air, D is the diameter of the cooling hole/slot (for a slot, $D = 2w$), w is the slot width, and Nu_x is local Nusselt number.

It is interesting to compare results of curve fitting the local heat transfer coefficient to existing correlations, for example, the Dittus-Boelter equation for constant wall temperature (CT) boundary condition in a cylindrical pipe is [144]:

$$Nu_D = 0.023 Re_D^{4/5} Pr^n \tag{9.3}$$

with $n = 0.4$ for $T_s > T_m$ (heating), and $n = 0.3$ for $T_s < T_m$ (cooling), this formula is applicable for $Re_D \gtrsim 10,000$, $(L/D) \gtrsim 10$, and $0.7 \leq Pr \leq 160$. T_s, T_m are surface and bulk temperatures, respectively. It is noted that the above formula tends to over-predict the Nusselt number for gases by at least 20%, and to under-predict Nusselt number for the higher-Prandtl-number fluids by $7 - 10\%$ [145]. Another formula derived by Kays and Crawford [145] for turbulent flow in a circular tube with fully developed velocity and temperature profiles in a cylindrical pipe subjected to a constant wall heat rate (CH) is:

$$Nu_D = 0.022 Re_D^{0.8} Pr^{0.5} \tag{9.4}$$

and for a constant wall temperature, the above equation can be modified by lowering the coefficient a few percents to yield (CT):

$$Nu_D = 0.021 Re_D^{0.8} Pr^{0.5} \tag{9.5}$$

In this chapter, the heat transfer coefficient will be defined and curve fitted for two cases: the first case is single cooling slot case at an injection angle of 45º, and the second case is a single cylindrical cooling hole at an injection angle of 30º.

9.2 The One Cooling Slot Case

In this case, the endwall has one cooling slot at an injection angle of 45º, the slot opening is $(s = 0.005\,m)$, slot width is $(w = 0.0071\,m)$ which gives a hydraulic diameter of $(D = 2w = 0.014\,m)$. A schematic diagram for the endwall is shown in Figure 9.0.
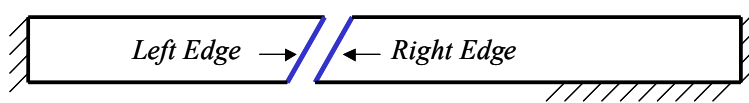
Figure 9.1. A schematic diagram for the endwall with one cooling slot case.

The thermal conductivity for air is ($k = 0.026 \, W/m.K$), the mass flow rate through the cooling slot is ($\dot{m} = 0.354 \, kg/sec$), length of the cooling slot is ($L = 0.0212 \, m$), coolant inlet temperature is ($T_{c,in} = 297.6 \, K$), and the coolant exit temperature is ($T_{c,out} = 295.5 \, K$), and the reference temperature is the fluid bulk temperature which is equal to ($T_{ref} = T_m = 294.77 \, K$). The result of curve fitting the local heat transfer coefficient at the left-side of the cooling slot is, see Figure 9.2(a):

$$h_x = \frac{1 + 0.046 Re_x^{0.40} Pr^{0.61}}{(2.536 \times 10^{-5} + x^{2.32})^{0.51}} \tag{9.6}$$

and at the other side of the cooling slot, i.e. the right side, is given by, see Figure 9.2(b):

$$h_x = \frac{2379 Pr (Re_x)^{-0.821}}{(0.0221 - x)^{1.38}} \tag{9.7}$$

(a) Left Edge   (b) Right Edge
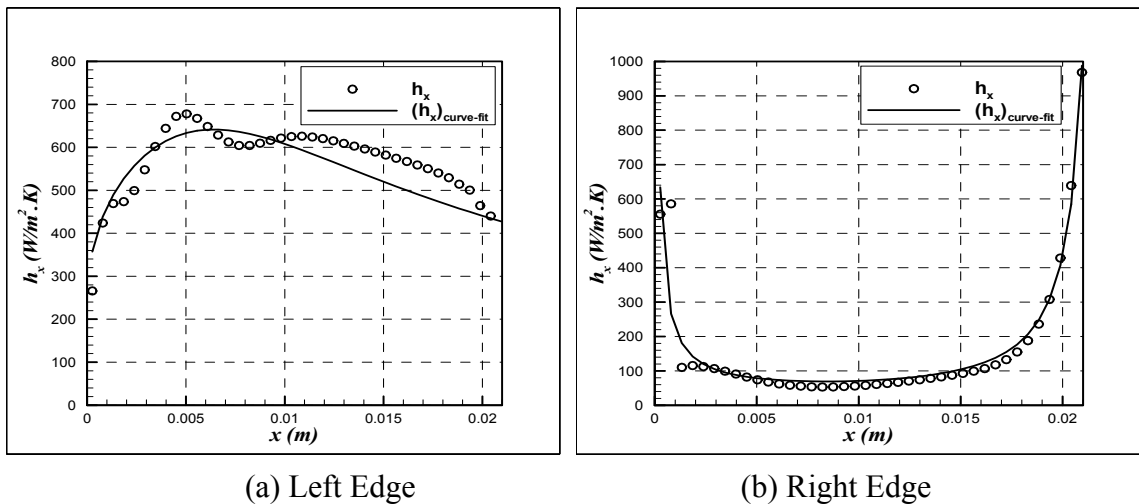
Figure 9.2. Curve fitting the local heat transfer coefficient along cooling slot edges for the case of one cooling slot.

A comparison in terms of Nusselt number for the average curve fitted heat transfer coefficient along each side and the values predicted by the other correlations is shown in Table 9.1. It can be seen that the average curve fitted Nu_D for both sides is approximately equal to the

average Nu_D predicted by Dittus-Boelter and Kays-Crawford correlations for a constant wall temperature, and it is in a better agreement with the average Nu_D predicted by Dittus-Boelter equation for a constant wall temperature and Kays-Crawford correlation for a constant wall heat rate.

Table 9.1. A comparison of the average Nusselt number for the case of one cooling slot.

Correlation Name	$(Nu_D)_{avg.}$
Left Side, Curve fitted	292.0
Right Side, Curve fitted	78.8
Average of left and right sides	185.4
Dittus-Boelter Equation, (*CT*)	205.5
Kays & Crawford Equation, (*CH*)	168.3
Kays & Crawford Equation, (*CT*)	160.6
Average of Dittus (*CT*) & Kays (*CH*)	186.9
Average of Dittus (*CT*) & Kays (*CT*)	183.1

9.3 The Single Cylindrical Cooling Hole Case

This is a 3D gas turbine endwall with one single, scaled-up cylindrical film cooling hole at an injection angle of 30°, a diameter of 10 mm, and length-to-diameter ratio of $(L/D = 6)$. The endwall has a cross-sectional area of 90 mm in width and 30 mm in height with total length of 500 mm, the geometry is shown in Figure 9.3.
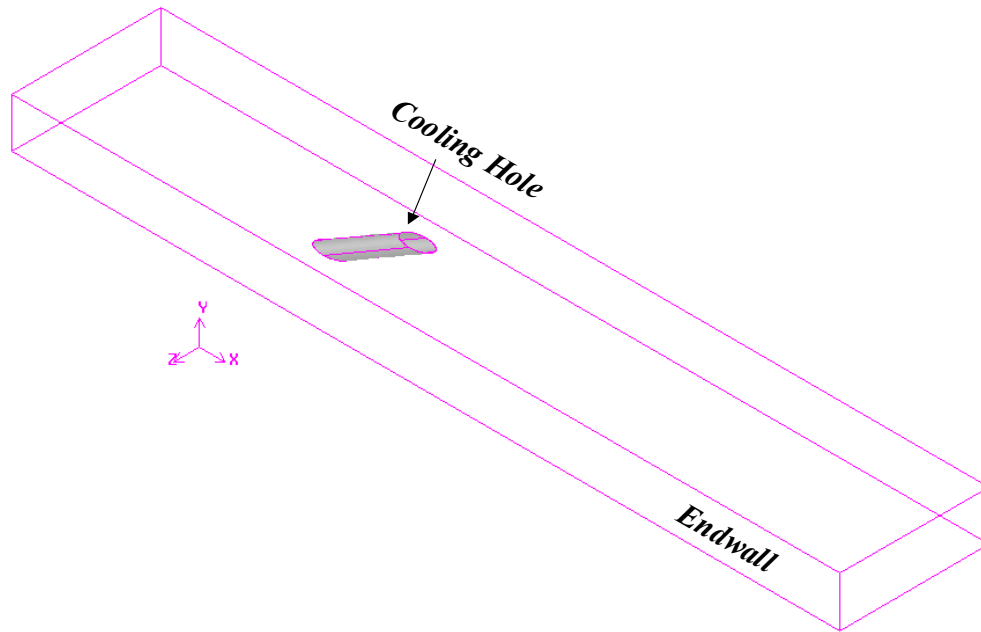
Figure 9.3. Geometry for the 3D endwall with single, scaled-up cylindrical cooling hole.

In this case, the analyses were done at more representative gas turbine engine conditions. For example, the coolant-to-mainflow temperature ratio was set to 0.54; i.e. the total temperature at the primary and secondary channels inlets were $540K$ and $290K$, respectively. In order to investigate this case at different blowing ratios from one up to five, the total pressure in the plenum was set to $109750Pa$, the total pressure at the mainflow inlet was $100400Pa$, and the static pressure at the mainflow outlet was adjusted to endup with the targeted blowing ratio. The conjugate cases with one cylindrical cooling hole are summarized in Table 9.2, where M is blowing ratio, $\dot{m}$ is the mass flow rate, Re_D is the Reynolds number based on cooling hole diameter, and $h_{avg.}$ is the area weight average along the walls of the cooling hole based on the plenum bulk temperature as a reference temperature.

Table 9.2. A summary for the conjugate heat transfer CHT models with one cylindrical cooling hole case.

No.	$P_{exit}\,(Pa)$	M	$\dot{m}\,(kg/sec)$	Re_D	$h_{avg.}\,(W/m^2K)$
1	$30,000$	1.21	0.0134	$107,508$	787.00
2	$68,000$	1.24	0.0126	$99,497$	744.70
3	$85,000$	1.34	0.0107	$81,367$	658.22
4	$94,000$	1.61	0.0091	$66,435$	575.00
5	$95,400$	1.74	0.0088	$63,618$	558.94
6	$97,050$	2.08	0.0084	$60,062$	538.83
7	$98,600$	2.56	0.0080	$56,451$	510.67
8	$99,500$	3.52	0.0078	$54,356$	506.25
9	$100,000$	4.88	0.0076	$53,051$	491.20

A plot of the velocity (m/sec) and temperature (K) contours along the cooling hole centerline plane $(z = 0)$ are shown in Figure 9.4. It can be seen that as the blowing ratio increases the jet penetrates deeper into the crossflow which results in a poorer fim cooling performance.
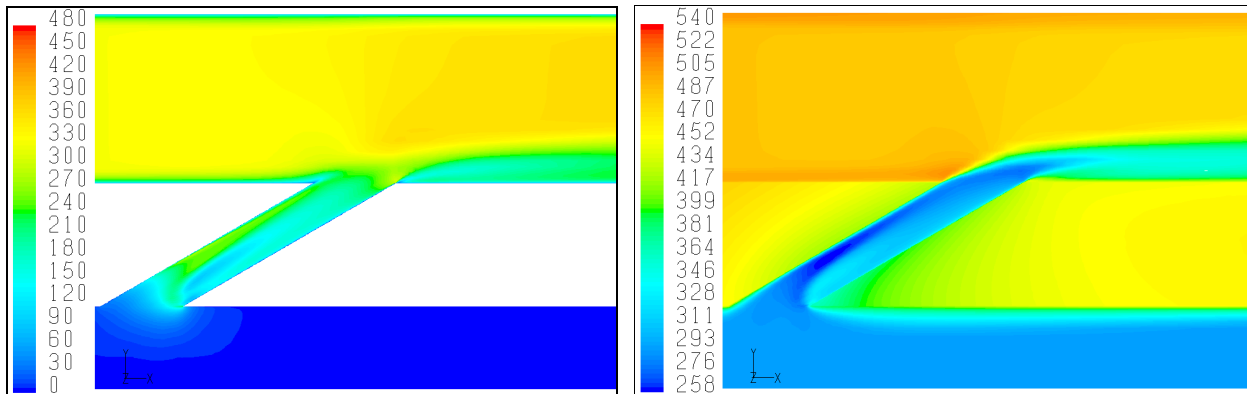
(a) Blowing Ratio, $M = 1.21$
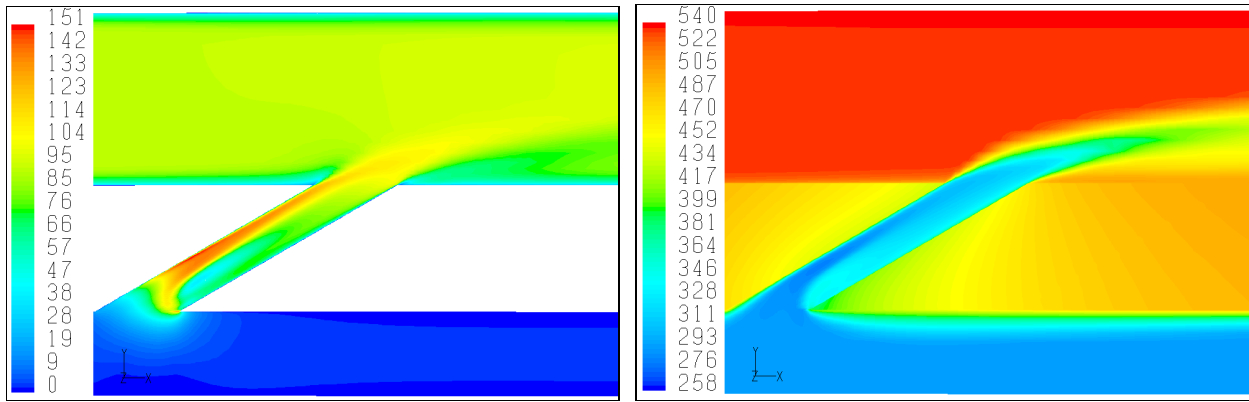
(b) Blowing Ratio, $M = 2.08$
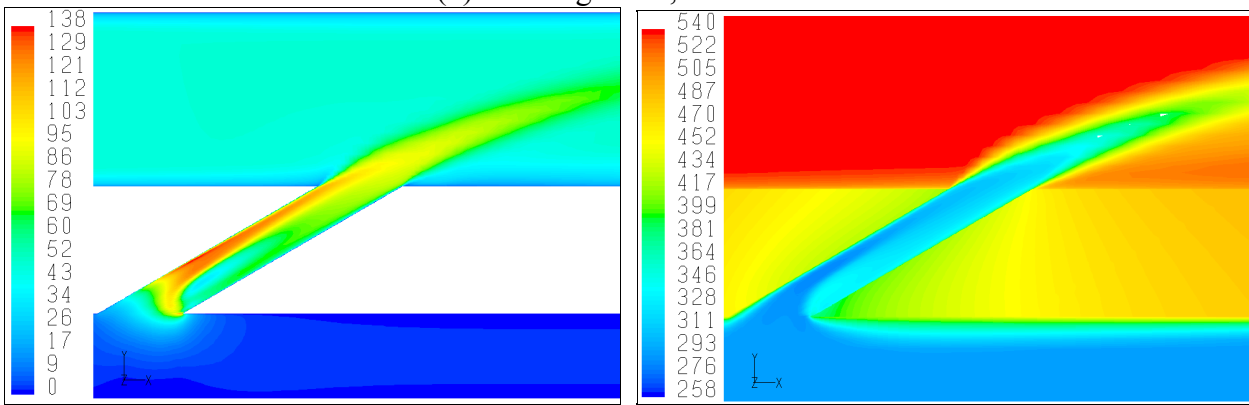
(c) Blowing Ratio, $M = 3.52$
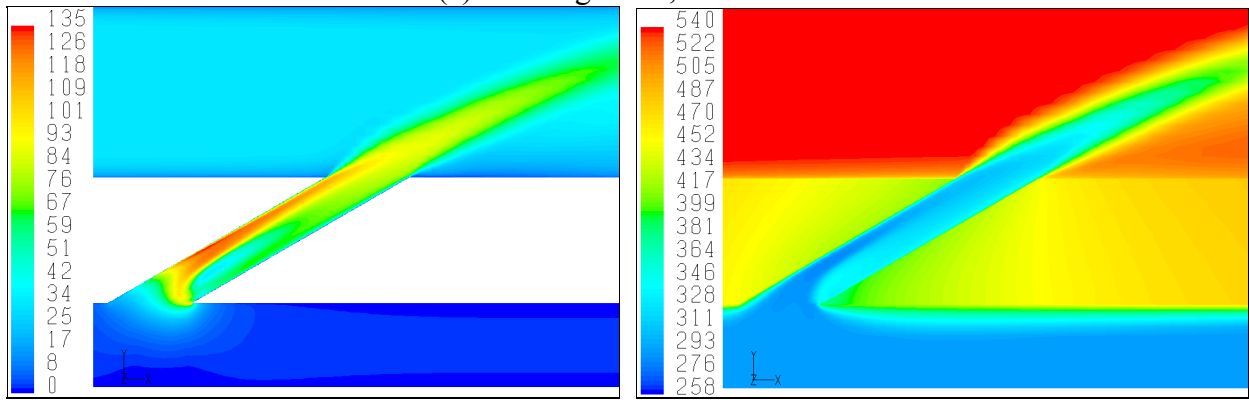
(d) Blowing Ratio, $M = 4.88$

Figure 9.4. Velocity magnitude contours (m/sec) on the left and temperature magnitude contours (K) on the right along centerline plane $(z = 0)$ in the film cooling hole region at different blowing ratios.

134

The result of curve fitting the average heat transfer coefficient along the walls of the cooling hole, see Figure 9.5, is:

$$\overline{h}_{\text{curvefitted}} = \frac{0.244 + Re_D^{0.65} \, Pr^{0.44} \, TR^{1.04}}{(0.315 + M^{0.04})^{0.20}} \tag{9.8}$$

where M is the blowing ratio, Re_D is the Reynolds number based on the cooling hole diameter, Pr is Prandtl number, and TR is the coolant-to-mainflow temperature ratio and it is equal to 0.54. Given that the thermal conductivity for air is ($k = 0.02767 \, W/m.K$), then the average Nusselt number based on the cooling hole diameter is:

$$Nu_D = \frac{0.088 + 0.36Re_D^{0.65} \, Pr^{0.44} \, TR^{1.04}}{(0.315 + M^{0.04})^{0.20}} \tag{9.9}$$
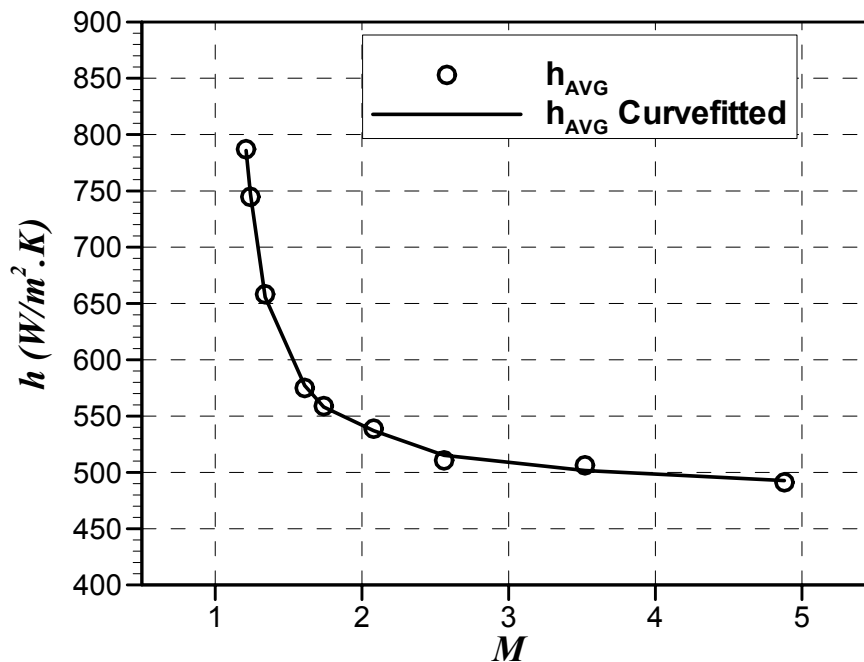
Figure 9.5. Curve fitting the average heat transfer coefficient along the walls of the cylindrical cooling hole.

CHAPTER 10

CONCLUSIONS AND RECOMMENDATIONS

Based on the work presented in this study the following conclusions are drawn:

1. In this study, conjugate heat transfer (CHT) finite volume models were developed to predict the metal temperature, and hence the film cooling effectiveness for 2D and 3D endwalls with application to film cooling slots/holes.

2. Considering the cooling slots models, a comparative study, indicating the ability of different turbulence models, is presented. This study showed that both versions of the k-ϵ; (RNG, RKE) and RSM models yielded essentially the same results with slight deviations. In contrast, the two versions of k-ω (SKW, SST) underpredict the flow field in comparison with the other three models, and overpredict the temperature field. In terms of the film cooling effectiveness, the predicted film effectiveness is in a better agreement with the analytical models for the cases of one cooling slot, also, the conjugate heat transfer model produces significant differences in comparison with the adiabatic models and analytical models.

3. The conjugate heat transfer models for the 3D endwalls were considered at more representative engine conditions, where the coolant-to-mainflow temperature ratio was 0.54. For the cases of single cylindrical cooling hole, the blowing ratio was 2.0, and the predictions of the two-equation turbulence models were compared to experimental data in terms of local centerline film cooling effectiveness. We found that it is very important to ascertain the grid dependence of the solutions, and to have a high quality hexahedral gird for accurate results. It is shown that in the region for $(x/D \leq 6)$, the predicted centerline effectiveness by the realizable k-ϵ turbulence model exhibited the best agreement with experimental data, and the other two-equation models under predicted the film cooling effectiveness. Whereas, in the region for $(x/D > 6)$, all models over predicted the centerline film cooling effectiveness, and the best agreement was predicted by

standard k-ϵ turbulence model. Also, results show the effect of the conjugate heat transfer on the temperature field in the film cooling hole region, and the additional heating up of the cooling jet itself.

4. Better film cooling characteristics can be achieved by considering the idea of shaping the cooling holes, for this reason a fan-shaped cooling hole was considered. From a modeling point of view, an important issue raised here is the grid topology, since it is a fan-shaped hole, a big effort is required to generate a high quality hexahedral mesh. For this reason, the effect of grid topology; i.e. hexahedral-, hybrid-, and tetrahedral-topology meshes on the predicted film cooling effectiveness was studied in more details. The turbulence closure was modeled using three turbulence models; RKE, SST, and V2F. We found that the predicted results using a hybrid mesh are identical to those predicted using a hexahedral mesh; this reduces the time required to generate a mesh especially for fan-shaped holes, and at the same time end up with accurate results. Surprisingly, the realizable k-ϵ model performs better than the $v^2 - f$ turbulence model in predicting the surface temperature distribution and hence, the film cooling effectiveness.

5. A novel inverse approach based on boundary elements and the genetic algorithm as means of determining heat flux distributions along the edges of cooling slots has been developed. The heat flux distributions are determined in an iterative manner by solving an inverse problem whose objective is to adjust the film cooling slot wall temperatures and heat fluxes until the temperature and heat flux at the measurement surfaces are matched in an overall heat conduction solution. The heat conduction problem is solved using boundary element methods (BEM), and the inverse problem is solved using genetic algorithm (GA). It can be noted that the genetic algorithm reconstructed heat flux distribution is robust, yielding very accurate results to both cases: exact input data, and error-laden inputs.

6. A hybrid singularity superposition boundary element-based inverse approach for the reconstruction of multi-dimensional heat flux distributions has been developed with application to film cooling slots and film cooling holes. Cauchy conditions are imposed at exposed surfaces

137

that are readily reached for measurements while convective boundary conditions are unknown at surfaces that are not amenable to measurements such as the walls of cooling slots/holes. The purpose of the inverse analysis is to determine the heat flux distribution along edges/walls of the cooling slots/holes. This is accomplished in an iterative process by distributing a set of singularities at the vicinity of the cooling slot surface inside a fictitious extension of the physical domain or along the cooling hole centerline with a given initial strength distribution. A forward steady-state heat conduction problem is solved using the boundary element method (BEM), and an objective function is defined to measure the difference between the heat flux measured at the exposed surfaces and the heat flux predicted by the BEM under the current strength distribution of the singularities. A genetic algorithm iteratively alters the strength distribution of the singularities until the measuring surfaces heat fluxes are matched, thus satisfying Cauchy conditions. Subsequent to the solution of the inverse problem, the heat flux at the inaccessible surface is computed using the BEM. The hybrid singularity superposition/BEM approach thus eliminates the need to mesh the surface of the film cooling slot and the need to parametrize the heat flux over that surface. Rather, the heat flux is determined in a post-processing stage after the inverse problem is solved. The results provided validate the approach and reveal good agreement between the BEM/GA predicted heat fluxes and the CHT simulated heat fluxes along the inaccessible walls of the cooling slots/holes for the one- and two- cooling slots and square and circular cooling holes.

7. After the heat flux distributions were determined, the results had been reported by defining the local film coefficient (h_x) as the local heat flux normalized with respect to an appropriate reference temperature. The resulting film coefficient distributions were fit to correlations reflecting dependency on position, the Prandtl and Reynolds numbers, blowing ratios, as well as coolant-to-mainflow temperature ratio. The correlations showed that the Nusselt number or heat transfer coefficients exhibited a highly non-linear behavior as a function of the considered parameters.

The following areas are suggested for future research:

1. In this study, the turbulence closure was modeled by applying the two-equations approach, which is considered a "standard" approach due to ease of implementation and computational economy. Also, the two-equations approach is based on the assumption that the eddy viscosity is the same for all Reynolds stresses, i.e. isotropic eddy viscosity. A natural extension will be the application of a higher order and a more accurate turbulence model to account for the flow anisotropy such as Reynolds Stress Model (RSM) for the cases of 3D cylindrical and fan-shaping cooling holes.

2. Conjugate heat transfer models were simulated for the cases of one- and two-cooling slots in addition to single cylindrical and fan-shaped cooling holes. An extension can be considered is developing a conjugate heat transfer model to investigate the local and laterally averaged film cooling effectiveness with multiple cooling holes or one or more rows of cooling holes.

3. In developing the inverse problem approach to reconstruct the heat flux distributions, all computations were carried out using a discontinuous quadratic isoparametric boundary elements in 2D cooling slots and constant boundary elements in 3D cooling holes. A higher accuracy results can be obtained by considering higher order boundary elements, i.e. linear, quadratic, and cubic elements.

4. The boundary integral equations (BIEs) were developed based on a linear model for the thermal conductivity; i.e. the thermal conductivity was assumed to be constant. Whereas, at gas turbine engine conditions, the metal thermal conductivity is a non-linear function of operating temperature. An extension that can be considered in developing the boundary integral equation is the introduction of the classical Kirchhoff transform which will remove the non-linearity effect in the steady state heat conduction equation, and account for the variation of the thermal conductivity.

5. In this study, the inverse problem approaches were developed to reconstruct the heat flux distributions for one slot, two slots, square holes, and cylindrical holes. Another extension will be to consider more complicated geometries such as shaped slots and shaped holes; i.e. fan-shaped holes.

APPENDIX A

LIST OF PUBLICATIONS GENERATED FROM THIS DISSERTATION

A.1 Journal Papers

1. Silieti, M., Divo, E., and Kassab, A.J., "An Inverse Boundary Element Method/Genetic Algorithm Based Approach for Retrieval of Multi-dimensional Heat Transfer Coefficients within Film Cooling Holes/Slots," *J. Inverse Problems in Science and Engineering* (in press).

2. Silieti, M., Divo, E., Kassab, A.J., 2005, "Singular Superposition/BEM Inverse Technique for Reconstruction of Multi-dimensional Heat Flux Distributions with Application to Film Cooling Holes," *Engineering Analysis - with Boundary Elements and other Mesh Reduction Methods* (under review).

A.2 Conference Papers

1. Silieti, M., Divo, E., and Kassab, A.J., 2005, "Film Cooling Effectiveness From a Single Scaled-up Fan-Shaped Hole: A CFD Simulation of Adiabatic and Conjugate Heat Transfer Models," *ASME Paper No. GT2005-68431*, June 6-9, Reno-Tahoe, Nevada.

2. Silieti, M., Divo, E., Kassab, A.J., 2005, "Singular Superposition/BEM Inverse Technique for Reconstruction of Multi-dimensional Heat Flux Distributions with Application to Film Cooling Holes," *27th World Conference on Boundary Elements and other Mesh Reduction Methods*, Kassab, A.J., Brebbia, C.A., and Divo E.A. (eds.), WIT Press, Southampton, (in press).

3. Silieti, M., Divo, E., and Kassab, A.J., 2004, "Numerical Investigation of Adiabatic and Conjugate Film Cooling Effectiveness on a Single Cylindrical Film Cooling Hole," *ASME Paper No. IMECE 2004-62196*, November 13-20, Anaheim, California, USA.

4. Silieti, M., Divo, E., Kassab, A.J., 2004, "Singular Superposition/BEM Inverse Technique for Reconstruction of Multi-dimensional Heat Flux Distributions with

Application to Film Cooling Slots," *ASME Paper No. IMECE 2004-62208*, November 13-20, Anaheim, California, USA.

5.   Silieti, M., Divo, E., and Kassab, A.J., 2004, "The Effect of Conjugate Heat Transfer on Film Cooling Effectiveness," *ASME Paper No. 2004-HT-FED-56234*, July 11-15, Charlotte, North Carolina, USA.

6.   Silieti, M., Divo, E., and Kassab, A.J., 2004, "An Inverse BEM/GA Based Approach For Retrieval of Multi-Dimensional Heat Transfer Coefficients within Film Cooling Holes/Slots," *BEM XXVI, Proc. of the 26th World Conf. on Boundary Elements and Other Mesh Reduction Methods*, C.A. Brebbia (ed.), Wessex Institute of Technology, Southampton, UK, pp. 217-227.

APPENDIX B

LIST OF PRESENTATIONS GENERATED FROM THIS DISSERTATION

1. "The Effect of Conjugate Heat Transfer on Film Cooling Effectiveness," 2004 ASME Heat Transfer/Fluids Engineering Summer Conference, July 11-15, Charlotte, North Carolina, USA.

2. "The Effect of Conjugate Heat Transfer on Film Cooling Effectiveness Using Multiple Turbulence Models," Fluent Users' Group Meeting 2004 CFD Summit, June 8-10, Dearborn, Michigan.

3. "An Inverse Boundary Element Method/Genetic Algorithm Based Approach for Retrieval of Multi-dimensional Heat Transfer Coefficients within Film Cooling Holes/Slots," IABEM 2004, May 24-26, Minneapolis, Minnesota.

4. "An Inverse BEM/GA Approach to determining Heat Transfer Coefficient Distributions within Film Cooling Holes/Slots", Inverse Problems in Engineering IPE 2003, June 8-9, Tuscaloosa, Alabama.

LIST OF REFERENCES

1. Goldstein, R.J., 1971, "Film Cooling," *Advances in Heat Transfer*, Vol. 7, pp. 321-379.

2. Hartnett, J.P., Birkebak, R.C., and Eckert, E.R.G., 1961, "Velocity Distributions, Temperature Distributions, Effectiveness and Heat Transfer for Air Injected Through a Tangential Slot Into a Turbulent Boundary Layer," *ASME J. Heat Transfer*, Vol. 83, pp. 293-306.

3. Chin, J.H., Skirvin, S.C., Hayes, L.E., and Burggaf, F., 1961, "Film Cooling With Multiple Slots and Louvers," *ASME J. Heat Transfer*, Vol. 83, pp. 281-292.

4. Blair, M.F., 1974, "An Experimental Study of Heat Transfer and Film Cooling on Large Scale Turbine Endwalls," *ASME J. Heat Transfer*, pp. 524-529.

5. Roy, R.P., Squires, K.D., Gerendas, M., Song, S., Howe, W.J. and Ansari, A., 2000, "Flow and Heat Transfer at the Hub Endwall of Inlet Vane Passages-Experiments and Simulations," *ASME Paper No. 2000-GT-198*.

6. Boyle, R.J., and Russell, L.M., 1990, "Experimental Determination of Stator Endwall Heat Transfer," *ASME J. Turbomachinery*, Vol. 112, pp. 547-558.

7. York, R.E., Hylton, L.D., and Mihelc, M.S., 1984, "An Experimental Investigation of Endwall Heat Transfer and Aerodynamics in a Linear Vane Cascade," *ASME J. Eng. Gas Turbines Power*, Vol. 106, pp. 159-167.

8. Kost, F. and Nicklas, M., 2001, "Film Cooled Turbine Endwall in a Transonic Flow FieldPart I- Aerodynamic Measurements," *ASME J. Turbomachinery*, Vol. 123, pp. 709-719.

9. Nicklas, M., 2001, "Film Cooled Turbine Endwall in a Transonic Flow Field: Part II-Heat Transfer and Film Cooling Effectiveness Measurements," *ASME J. Turbomachinery*, Vol. 123, pp. 720-729.

10.   Knost, D.G. and Thole, K.A., 2003, "Computational Predictions of Endwall Film Cooling for a First Stage Vane", *ASME Paper No. 2003-GT-38252*, Georgia, USA.

11.   O' Malley, K., 1984, " Theoretical Aspects of Film Cooling", *Ph.D. Thesis*, University of Oxford.

12.   Fitt, A.D., Ockendon, J.R., and Jones, T.V., 1985, "Aerodynamics of slot-film cooling: theory and experiment", *J. Fluid Mech.*, Vol. 160, pp. 15-30.

13.   Sarkar, S., Bose, T.K., 1995, "Comparizon of Different Turbulence Models for Prediction of Slot-Film Cooling - Flow and Temperature - Field," *Numer. Heat Transfer: Part B*, Vol. 28(2), pp. 217-238.

14.   Teekaram, A.J.H., Forth, C.J.P., and Jones, T.V., 1991, "Film Cooling in the presence of Mainstream Pressure Gradients," *ASME J. Turbomachinery*, Vol. 113(3), pp. 484-492.

15.   Kassimatis, P.G., Bergeles, G.C., Jones, T.V., and Chew, J.W., 2000, "Numerical Investigation of the Aerdynamics of the Near Slot Film Cooling," *Int. J. Numer. Methods in Fluids*, Vol. 32(1), pp. 85-104.

16.   Jia, R., Sunden, B., Miron, P., and Leger, B., 2003, "Numerical and Experimental Study of the Slot Film Cooling Jet with Various Angles," *ASME Paper No. 2003-HT-47372*, Las Vegas, Nevada, USA

17.   Goldstein, R.J., Eckert, E.R.G., and Ramsey, J.W., 1968a, "Film Cooling With Injection Through Holes: Adiabatic Wall Temperatures Downstream of a Circular Hole," *ASME J. Engng. Pwr. Trans. Part A*, Vol. 90, pp. 384-395.

18.   Goldstein, R.J., Eckert, E.R.G., and Ramsey, J.W., 1968b, "Film Cooling With Injection Through a Circular Hole," *NASA CR 56404*, (also University of Minnesota Heat Transfer Laboratory TR No. 82).

19.   Goldstein, R.J., Eckert, E.R.G., Eriksen, V.L., and Ramsey, J.W., 1970, "Film Cooling Following Injection Through Inclined Circular Tubes," *Israel J. Technology*, Vol. 8, pp. 145-154.

20.   Goldstein, R.J., Eckert, E.R.G., and Burggraf, F., 1974, "Effects of Hole Geometry and Density on Three Dimensional Film Cooling," *Int. J. Heat Mass Transfer*, Vol. 17, pp. 595-607.

21.   Goldstein, R.J., and Yoshida, T., 1982, "Boundary Layer and Laminar Injection on Film Cooling Performance," *ASME J. Heat Transfer*, Vol. 104, pp. 355-362.

22.   Goldstein, R.J., Jin, P., and Olson, R.L., 1998, "Film Cooling Effectiveness and Mass/Heat Transfer Coefficient Downstream of One Row of Discrete Holes," *ASME Paper No. 98-GT-174*.

23.   Pedersen, D.R., Eckert, E.R.G., and Goldstein, R.J., 1977, "Film Cooling With Large Density Differences Between The Mainstream and the Secondary Fluid Measured By The Heat-Mass Transfer Analogy," *ASME J. Heat Transfer*, Vol. 99, pp. 620-627.

24.   Bergeles, G., Gosman, A.D., and Launder, B.E., 1977, "The Near-Field Character of a Jet Discharged Through a Wall at 30° to a Mainstream," *AIAA Journal*, Vol. 14, pp.499-504.

25.   Andreopoulos, J., and Rodi, W., 1984, "Experimental Investigation of Jets in a Crossflow," *J. Fluid Mechanics*, Vol. 138, pp. 92-127.

26.   Pietrzyk, J.R., Bogard, D.G. and Crawford, M.E., 1988, "Hydrodynamic Measurements of Jets in Crossflow for Gas Turbine Film Cooling Applications," *ASME Paper No. 88-GT-194*.

27.   Pietrzyk, J.R., Bogard, D.G. and Crawford, M.E., 1989, "Hydrodynamic Measurements of Jets in Crossflow for Gas Turbine Film Cooling Applications," *ASME J. Turbomachinery*, Vol. 111, pp. 139-145.

28. Pietrzyk, J.R., Bogard, D.G. and Crawford, M.E., 1990, "Effects of Density Ratio on the Hydrodynamics of Film Cooling," *ASME J. Turbomachinery*, Vol. 112, pp. 437-443.

29. Sinha, A.K., Bogard, D.G. and Crawford, M.E., 1991, "Film Cooling Effectiveness Downstream of a Single Row of Holes With Variable Density Ratio," *ASME J. Turbomachinery*, Vol. 113, pp. 442-449.

30. Jubran, B.A., 1989, "Correlation and Prediction of Film Cooling from Two Rows of Holes," *ASME J. Turbomachinery*, Vol. 111, pp. 502-509.

31. Makki, Y., and G. Jakubowski, 1986, "An Experimental Study of Film Cooling From Diffused Trapezoidal Shaped Holes," *AIAA Paper No. 86-1326*.

32. Wittig, S., Schulz, A., Gritsch, M., and Thole, K, 1996, "Transonic Film-Cooling Investigations: Effects of Hole Shape and Orientations," *ASME Paper No. 96-GT- 222*.

33. Thole, K.M., Gritsch, A., Schulz, and Wittg, S., 1997, "Effect of a Crossflow at the Entrance to a Film-Cooling Hole," *ASME J. Fluids Engineering*, Vol. 119, pp. 533-540.

34. Gritsch, M., Schulz, A., and Wittig, S., 1998, "Adiabatic Wall Effectiveness Measurements of Film Cooling Holes With Expanded Exits," *ASME J. Turbomachinery*, Vol. 120, pp. 549-556.

35. Bell, C.M., Hamakawa, H., and Ligrani, P.M., 2000, "Film Cooling From Shaped Holes," *ASME J. Heat Transfer*, Vol. 122, pp. 224-232.

36. Yu, Y., Yen, C.-H., Shih, T.I.-P., Chyu, M.K., and Gogineni, S., 2002, "Film Cooling Effectiveness and Heat Transfer Coefficient Distributions Around Diffusion Shaped Holes," *ASME J. Heat Transfer*, Vol. 124, pp. 820-827.

37. Yuen, C.H.N., and Martinez-Botas, R.F., 2003, "Film Cooling Characteristics of a Single Round Hole at Various Streamwise Angles in a Crossflow: Part I Effectiveness," *Int. J. Heat Mass Transfer*, Vol. 46, pp. 221-235.

38. Friedrichs, S., Hodson, H.P. and Dawes, W.N., 1996, "Distribution of Film Cooling Effectiveness on a Turbine Endwall Measured Using the Ammonia and Diazo Technique," *ASME J. Turbomachinery*, Vol. 118, pp. 613-621.

39. Friedrichs, S., Hodson, H.P. and Dawes, W.N., 1997, "Aerodynamic Aspects of Endwall Film Cooling," *ASME J. Turbomachinery*, Vol. 119, pp. 786-793.

40. Friedrichs, S., Hodson, H.P. and Dawes, W.N., 1999, "The design of an improved Endwall Film Cooling Configuration," *ASME J. Turbomachinery*, Vol. 121, pp. 772-780.

41. Farmer, J.P., Seager, D.J., and Liburdy, J.A., 1997, "The Effect of Shaping Inclined Slots on Film Cooling Effectiveness and Heat Transfer Coefficient", *ASME Paper No. 97-GT-399*, Orlando, Florida, USA.

42. Sargison, J.E., Lock, G.D., Guo, S.M., Oldfield, M.L.G., and Rawlinson, A.J., 2003, "Performance Prediction of A Converging Slot-Hole Film-Cooling Geometry," *ASME Paper No. GT-2003-38144*, Atlanta, Georgia, USA.

43. Walters, D.K., and Leylek, J.H., 1997, "A Detailed Analysis of Film-Cooling Physics Part I: Streamwise Injection with Cylindrical Holes," *ASME Paper No. 97-GT-269*, Orlando, Florida, USA.

44. Hyams, D.G., and Leylek, J.H., 1997, "A Detailed Analysis of Film-Cooling Physics Part II: Streamwise Injection with Shaped Holes," *ASME Paper No. 97-GT-271*, Orlando, Florida, USA.

45. York, D.Y., and Leylek, J.H., 2002, "Leading Edge Film Cooling Physics: Part I - Adiabatic Effectiveness," *ASME Paper No. GT-2002-30166*, Amesterdam, The Netherlands.

46. York, D.Y., and Leylek, J.H., 2002, "Leading Edge Film Cooling Physics: Part II - Heat Transfer Coefficient," *ASME Paper No. GT-2002-30167*, Amesterdam, The Netherlands.

47. Kercher, D.M., 1998, "A Film Cooling CFD Bibliography: 1971-1996," *Int. J. of Rotating Machinery*, Vol. 4, pp. 61-72.

150

48. Bergeles, G., Gosman, A.D., and Launder, B.E., 1978, "The Turbulent Jet in a Cross Stream at Low Injection Rates: A Three Dimensional Numerical Treatment," *Numer. Heat Transfer*, Vol. 1, pp. 217-242.

49. Demoran, A.O., 1982, "Numerical Calculations of Steady Three-Dimensional Turbulent Jets in Cross Flow," *Rep. SFB 80/T/129*. Sonderschungsbereich 80, University of Karlsuhe, Germany.

50. Demuren, A.O., Rodi, W., and Schönung, B., 1986, "Systematic Study of Film Cooling with a Three Dimensional Calculation Procedure," *ASME J. Turbomachinery*, Vol. 108, pp. 121-130.

51. Amer, A.A., Jubran, B.A., and Hamdan, M.A., 1992a, "Comparison of Different Two -Equation Turbulence Models for Prediction of Film Cooling from Two Rows of Holes," *Numer. Heat Transfer*, Vol. 21, pp. 143-162.

52. Leylek, J.H., and Zerkle, R.D., 1994, "Discrete Jet-Film Cooling: A Comparison of Computational Results with Experiments," *ASME J. Turbomachinery*, Vol. 113, pp. 358-368.

53. Walters, D.K., and Leylek, J.H., 1997, "A systimatic Computational Mathodology Applied to a Three-Dimensional Film-Cooling Flowfield," *ASME J. Turbomachinery*, Vol. 119, pp. 777-785.

54. Walters, D.K., and Leylek, J.H., 2000, "A Detailed Analysis of Film Cooling Physics: Part I - Streamwise Injection With Cylindrical Holes," *ASME J. Turbomachinery*, Vol. 122, pp. 102-112.

55. McGovern, K.T., and Leylek, J.H., 2000, "A Detailed Analysis of Film Cooling Physics: Part II -Compound Angle Injection With Cylindrical Holes," *ASME J. Turbomachinery*, Vol. 122, pp. 113-121.

56. Hyams, D.G., and Leylek, J.H., 2000, "A Detailed Analysis of Film Cooling Physics: Part III - Streamwise Injection With Shaped Holes," *ASME J. Turbomachinery*, Vol. 122, pp. 122-132.

57. Brittingham, R.A., and Leylek, J.H., 2000, "A Detailed Analysis of Film Cooling Physics: Part IV - Compound Angle Injection With Shaped Holes," *ASME J. Turbomachinery*, Vol. 122, pp. 133-145.

58. Heidmann, J.D., and Hunter, S.D., 2001, "Coarse Grid Modeling of Turbine Film Cooling Flows Using Volumetric Source Terms," *ASME Paper No. 2001-GT-0138*.

59. Ligrani, P.M., Wigle, J., M., Ciriello, S., and Jackson, S.M., 1994, "Film Cooling From Holes With Compound Angle Orientations: Part 1- Results Downstream of Two Staggared Rows of Holes with 3d Spanwise Spacing," *ASME J. Heat Transfer*, Vol. 116, pp. 341-352.

60. Ligrani, P.M., Wigle, J., and Jackson, S.M., 1994, "Film Cooling From Holes With Compound Angle Orientations: Part 2- Results Downstream of a Single Row of Holes with 6d Spanwise Spacing," *ASME J. Heat Transfer*, Vol. 116, pp. 353-362.

61. Schmidt, D., Sen, B., and Bogard, D., 1996, "Film Cooling With Compound Angle Holes: Adiabatic Effectiveness," *ASME J. Turbomachinery*, Vol. 118, pp. 807-813.

62. Sen, B., Schmidt, D., and Bogard, D., 1996, "Film Cooling With Compound Angle Holes: Heat Transfer," *ASME J. Turbomachinery*, Vol. 118, pp. 800-806.

63. Ligrani, P.M., and Ramsey, A.E., 1997, "Film Cooling From a Single Row of Holes Oriented in Spanwise/Normal Planes," *ASME J. Turbomachinery*, Vol. 119, pp. 770-776.

64. Haven, B.A., Yamagata, D.K., Kurosaka, M., Yamawaki, S., and Maya, T., 1997, "Anti -Kidney Pair of Vortices in Shaped Holes and Their Influence on Film Cooling Effectiveness," *ASME Paper No. 97-GT-45*, Orlando, Florida, USA.

65. Chen, P-H., Ai, D., and Lee, S.-H., 1998, "Effects of Compund Angle Injection on Flat -Plate Film Cooling Through a Row of Conical Holes," *ASME Paper No. 99-GT-459*.

66. Kelkar, K.M., Choudhury, D., and Ambrosi, M., 1991, "Numerical Method for the Computation of Conjugate Heat Transfer in Nonorthogonal Boundary-Fitted Coordinates," *Numer. Heat Transfer: Part B*, Vol. 20, pp. 25-40.

67. Heselhaus, A., and Vogel, D.T., 1995, "Numerical Simulation of Turbine Blade Cooling with Respect to blade heat conduction and inlet temperature profiles," *AIAA Paper No. 95-3041, 31st AIAA/ASME/SAE/ASEE Joint Propulsion*, Conference and Exhibit, San Diego, CA.

68. Papanicolaou, E., Giebert, D., Koch, R., and Schulz, A, 2001, "A Conservation-Based Discretization Approach for Conjugate Heat Transfer Calculations in Hot-Gas Ducting Turbomachinery Components," *Int. J. Heat Mass Transfer*, Vol. 44, pp. 3413-3429.

69. Bohn, D., Bonhoff, B., Schonenborn, H., and Wilhelmi, H., 1995, "Prediction of the Film Cooling Effectiveness of Gas Turbine Blades Using a Numerical Model for the Coupled Simulation of Fluid Flow and Diabatic Walls", *AIAA Paper No. 95-7105*.

70. Bohn, D., Bonhoff, B., Schonenborn, H., and Wilhelmi, H., 1995, "Validation of a Numerical Model for the Coupled Simulation of Fluid Flow and Diabatic Walls with Application to Film-cooled Turbine Blades," *VDI-Bericht 1186, pp. 295-272*, Germany.

71. Bohn, D., Kruger, U., and Kusterer, K., 2001, "Conjugate Heat Transfer: An Advanced Computational Method for the Coupling Design of Modern Gas Turbine Blades and Vanes, In: Heat Transfer in Gas Turbines," *Heat Transfer in Gas Turbines, B*. Sunden and M. Faghri, ed., WIT Press, Southampton, U.K., pp. 55-108.

72. Li, H. J. and Kassab, A.J., 1994, "Numerical Prediction of Fluid Flow and Heat Transfer in Turbine Blades with Internal Cooling," *AIAA/ASME Paper No. 94-1981*.

73. Li, H. J. and Kassab, A.J., 1994, "A coupled FVM/BEM Solution to Conjugate Heat Transfer in Turbine blades," AIAA/ASME Paper No. 94-1981.

74. Heidmann, J.D., Kassab, A.J., Divo, E., Rodriguez, F., and Steinthorsson, E., 2003, "Conjugate Heat Transfer Effects on a Realistic Film Cooled Turbine Vane," *ASME Paper No. GT2003-38369*, ASME Turbo Expo 2003, June 16-19, Georgia, USA.

75. Kassab, A.J., Divo, E., Heidmann, J.D., Steinthorsson, E., and Rodriguez, F., 2003, "BEM/FVM Conjugate Heat Transfer Analysis of a Three-Dimensional Film Cooled Turbine Blade," *Inter. J. Numerical Methods in Heat Transfer and Fluid Flow*, Vol. 13(5), pp. 581-610.

76. York, W.D., and Leylek, J.H., 2003, "Three-Dimensional Conjugate Heat Transfer Simulation of an Internally-Cooled Gas Turbine Vane", *ASME Paper No. 2003-GT -38551*, Georgia, USA.

77. Bohn, D., Ren, J.,and Kusterer, K., 2003, "Conjugate Heat Transfer Analysis for Film Cooling Configurations with Different Hole Geometries," *ASME Paper No. 2003-GT - 38369*, Georgia, USA.

78. Rigby, D.L., and Lepicovsky, J., 2001, "Conjugate Heat Transfer Analysis of Internally Cooled Configurations," *ASME Paper No. 2001-GT-0405*, June 4-7, New Orleans, LA.

79. Silieti, M., Divo, E., and Kassab, A.J., 2004, "The Effect of Conjugate Heat Transfer on Film Cooling Effectiveness," *ASME Paper No. 2004-HT-FED-56234*, July 11-15, Charlotte, North Carolina, USA.

80. Silieti, M., Divo, E., and Kassab, A.J., 2004, "Numerical Investigation of Adiabatic and Conjugate Film Cooling Effectiveness on a Single Cylindrical Film Cooling Hole," *ASME Paper No. IMECE 2004-62196*, November 13-20, Anaheim, California, USA.

81.   Silieti, M., Divo, E., and Kassab, A.J., 2005, "Film Cooling Effectiveness From a Single Scaled-up Fan-Shaped Hole: A CFD Simulation of Adiabatic and Conjugate Heat Transfer Models", *ASME Paper No. GT2005-68431*, June 6-9, Reno-Tahoe, Nevada.

82.   Thikonov, A.N. and Arsenin, 1994, *Solution of Ill-Posed Problems*, John Wiley and Sons, New York.

83.   Beck, J.V., Blackwell, B., and St. Clair, C.R., 1985, *Inverse Heat Conduction: Ill-Posed Problems*, John Wiley and Sons, New York.

84.   Kurpisz, K. and Nowak, A.J., 1992, "BEM Approach to Inverse Heat Conduction Problems," *Eng. Analysis*, Vol. 10, pp. 291-297.

85.   Alifanov, O.M., 1994, *Inverse Heat Transfer Problems*, Springer Verlag, New York.

86.   Bui, H.D., 1994, *Inverse Problems in Mechanics of Materials: An Introduction*, CRC Press, Boca Raton.

87.   Bonnet, M., Bui, H.D., Maigre, H., and Planchard, J., 1992, "Identification of Heat Conduction Coefficient: Application to Non-destructive Testing," *IUTAM Symposium on Inverse Problems in Engineering Mechanics,* Bui, H.D. and Tanaka, M.(eds.), SpringerVerlag, New York.

88.   Divo, E., Kassab, A.J., and Rodriguez, F., 2000, "Characterization of Space Dependent Thermal Conductivity with a BEM-Based Genetic Algorithm," *Numer. Heat Transfer: Part A*, Vol. 37(8), pp. 845-877.

89   Taler, J., 1992, "Non-Linear Steady-State Inverse Heat Conduction Problem with Space Variable Boundary Conditions," *ASME J. Heat Transfer*, Vol. 114(4), pp. 108-1051.

90.   Chen, M.M., Pederson, C.O., and Chato, J.C., 1977, "On the Feasibility of Obtaining Three Dimensional Information form Thermographic Measurements," *J. Biomedical Engineering*, Vol. 99(2), pp. 58-64.

91.   Cannon,J.R. and Esteva, S.P., 1986, "An Inverse Problem for the Heat Equation," *Inverse Problems*, Vol. 2, pp. 395-403.

92.   Meric, A., 1988, "Shape Design Sensitivity Analysis for Non-Linear Anisotropic Heat Conducting Solids and Shape Optimization by the BEM," *Inter. J. for Numerical Methods in Engineering*, Vol. 26, pp. 109-120.

93   Dulikravich, G. and Martin, T.J., 1995, "Geometrical Inverse Problems in Three Dimensional Non-Linear Steady Heat Conduction," *Engineering Analysis*, Vol. 15, pp. 161-169.

94.   Meric, A. and Kul, 1993, "Differential and BIE Formulations of Optimal Heating of Solids," *BEMXV, Proceedings of the 15th International Conference on Boundary Elements*, Brebbia, C.A. and Rencis. J.J. (eds.), pp. 486-501.

95.   Kane, J.H. and Wang, H., 1992, "Boundary Formulations for Shape Sensitivity of Temperature Dependent Conductivity Problems," *Inter. J. Numerical Methods in Engineering*, Vol. 33, pp. 667-693.

96.   Divo, E., Kassab, A.J., and Ingber, M.S., 2003, "Shape Optimization of Acoustic Scattering Bodies," *Engineering Analysis with Boundary Elements*, Vol. 27(7), pp. 695-704 .

97.   Divo, E., Kassab, A.J., and Rodriguez, F., "A Hybrid Singularity Superposition/BEM Method for the Solution of the Inverse Geometric Problem," *Numerical Heat Transfer*, (in press).

98.   Kassab, A.J., Hsieh, C.K., and Pollard, J., 1997, "Solution of the Inverse Geometric Problem for the Detection of Subsurface Cavities by the IR CAT Method," Chapter 2, *Boundary Integral Formulations in Inverse Analysis*, L.C. Wrobel and D.B. Ingham, (eds.), Computational Mechanics, Boston, pp. 33-65.

99.   Kassab, A.J. and Pollard, J., 1995, "An Inverse Heat Conduction Algorithm for the Thermal Detection of Arbitrarily Shaped Cavities," *Inverse Problems in Engineering*, Vol. 1(3), pp. 231-245.

100. Kassab, A.J. and Pollard, J., 1994, "Automated Cubic Spline Anchored Grid Pattern Algorithm for the High Resolution Detection of Subsurface Cavities by the IR-CAT Method," *Numer. Heat Transfer: Part B*, Vol. 26(1), pp. 63-78.

101. Kassab, A.J., Moslehy, F.A., and Daryapurkar, A., 1994, "Nondestructive Detection of Cavities By An Inverse Elastostatics Method," *Engineering Analysis with Boundary Elements*, Vol. 13(1), pp. 45-56.

102. Kassab, A.J. and Pollard, J. 1993, "Automated Algorithm for the Nondestructive Detection of Subsurface Cavities by the IR-CAT Method," *J. Nondestructive Evaluation*, Vol.12(3), pp. 175-187.

103. Kassab, A.J. and Hsieh, C.K., 1987, "Application of Infrared Scanners and Inverse Heat Conduction Problems to Infrared Computerized Axial Tomography," *Review of Scientific Instruments*, Vol. 58(1), pp. 89-95.

104. Hsieh, C.K. and Kassab, A.J., 1985, "A General Method for the Solution of Inverse Heat Conduction Problems with Partially Unknown System Geometries," *Inter. J. Heat and Mass Transfer*, Vol.29(1), 1985, pp. 47-58.

105. Maillet, D, Degiovanni, A., and Pasquetti, R., 1991, "Inverse Heat Conduction Applied to Measurements of Heat Transfer Coefficient on a Cylinder: Comparison Between an Analytical and a Boundary Element Technique," *ASME J. Heat Transfer*, Vol. 113, pp. 549-557.

106. Farid, M.S. and Hsieh, C.K., 1992, "Measurement of Free Convection Heat Transfer Coefficient for a Rough Horizontal Nonisothermal Cylinder in Ambient Air by Infrared Scanning," *ASME J. Heat Transfer*, Vol. 114, pp. 1054-1056.

107. Martin, T.J. and Dulikravich, G.S., 1998, "Inverse Determination of Steady Heat Convection Coefficient Distributions," *ASME J. Heat Transfer*, Vol. 120, pp. 328-334.

108. Kassab, A.J., Divo, E., and Chyu, M., 1999, "A BEM-Based Inverse Algorithm to Retrieve Multi-Dimensional Heat Transfer Coefficients from Transient

Temperature Measurements", *BETECH99, Proceedings of the 13th International Boundary Element Technology Conference*, Las Vegas, June 8-10, Chen, C. S., Brebbia, C.A., and Pepper, D. (eds.), Computational Mechanics, Boston, Ma., pp. 65-74.

109. Divo, E., Kassab, A.J., Kapat, J.S., and Chyu, M.K., 1999, "Retrieval of multidimensional Heat Transfer Coefficient Distributions Using an Inverse BEM-Based Regularized Algorithm: numerical and Experimental Results", *ASME Paper No. HTD-Vol. 364-1*, pp. 235-244, Proceedings of the ASME, Heat Transfer Division, Witte, L. C.(ed.).

110. Kassab, A.J., Divo, E. and Kapat, J.S., 2001, "Multi-Dimensional Heat Flux Reconstruction Using Narrow-Band Thermochromic Liquid Crystal Thermography", *Inverse Problems in Engineering*, Vol. 9, pp. 537-559.

111. Bialecki, R.A., Divo, E., and Kassab, A.J., 2002, "Unknown Time Dependent Heat Flux Boundary Condition Reconstruction Using a BEM-Based Inverse Algorithm," Electronic *J. Boundary Elements*, Vol. BETEQ(1), pp. 104-114. URL: http://tabula.rutgers.edu/EJBE/proceedings/2001/.

112. Bialecki, R., Divo, E., Kassab, A.J., and Ait Maalem Lahcen, R., 2003, "Explicit Calculation of Smoothed Sensitivity Coefficients for Linear Problems," *Inter. J. Numerical Methods in Engineering*, Vol. 57(2), pp. 143-167.

113. Silieti, M., Divo, E., and Kassab, A.J., 2004, "An Inverse BEM/GA Based Approach For Retrieval of Multi-Dimensional Heat Transfer Coefficients within Film Cooling Holes/Slots," *BEM XXVI, Proc. of the 26th World Conf. on Boundary Elements and Other Mesh Reduction Methods*, C.A. Brebbia (ed.), Wessex Institute of Technology, Southampton, UK, pp. 217-227.

114. Silieti, M., Divo, E., and Kassab, A.J., "An Inverse Boundary Element Method/Genetic Algorithm Based Approach for Retrieval of Multi-dimensional Heat Transfer

Coefficients within Film Cooling Holes/Slots", *J. Inverse Problems in Science and Engineering* (in press).

115. Divo, E., Kassab, A.J., and Rodrigues, F., 2003, "An Efficient Singular Superposition Technique For Cavity Detection and Shape Optimization," *Inverse Problems in Engineering Mechanics IV*: international symposium on inverse problems in engineering mechanics, (ISIP 2003), Masataka Tanaka, (Ed.), Elsevier Press, pp. 241-250.

116. Divo, E., Kassab, A.J., and Rodrigues, F., "An Efficient Singular Superposition Technique For Cavity Detection and Shape Optimization," *Numerical Heat Transfer Journal* (in press).

117. Silieti, M., Divo, E., Kassab, A.J., 2004, "Singular Superposition/BEM Inverse Technique for Reconstruction of Multi-dimensional Heat Flux Distributions with Application to Film Cooling Slots", *ASME Paper No. IMECE 2004-62208*, November 13-20, Anaheim, California, USA.

118. Silieti, M., Divo, E., Kassab, A.J., 2005, "Singular Superposition/BEM Inverse Technique for Reconstruction of Multi-dimensional Heat Flux Distributions with Application to Film Cooling Holes", *27th World Conference on Boundary Elements and other Mesh Reduction Methods*, March 15-17, 2005, Orlando, Florida, USA.

119. Yakhot, V., and Orszag, S.A., 1986, "Renormalization Group Analysis of Turbulence: I. Basic Theory." *J. Scientific Computing*, Vol. 1(1), pp. 1-51.

120. Choudhury, D., 1993, "Introduction to the Renormalization Group Method and Turbulence Modeling," *Fluent Inc. Technical Memorandom TM-107*.

121. Shih, T.-H., Liou, W.W, Shabbir, A., Yang, Z., and Zhu, J., 1995, "A New k-ϵ Eddy -Viscosity Model for High Reynolds Number Turbulent Flows-Model Development and Validation," *Computers Fluids*, Vol. 24(3), pp. 227-238.

122. Wilcox, D.C., 2002, *Turbulence Modeling for CFD*, DCW Industries, Second Edition, La Cañada, California.

123. Menter, R., 1994, "Two-Equation Eddy-Viscosity Turbulence Models for Engineering Applications," *AIAA Journal*, Vol.32(8), pp. 1598-1605.

124. Gibson, M.M., and Launder, B.E., 1978, "Ground Effects on Pressure Fluctuations in the Atmospheric Boundary Layer," *J. Fluid Mech.*, Vol. 86, pp. 491-511.

125. Launder, B.E., 1989, "Second Moment Closure: Present... and Future?," *J. Fluid Mech.*, Vol. 10(4), pp. 282-300.

126. Launder, B.E., Reece, G.J., and Rodi, W., 1975, "Progress in the Development of a Reynolds-Stress Turbulence Closure," *J. Fluid Mech.*, Vol. 68(3), pp. 537-566.

127. Goldstein, R.J., Eckert, E.R.G., and Wilson, D.J., 1968, *J. Eng. Ind.*, Vol. 90, pp. 584.

128. Launder, B., and Spalding, D., 1974, " The Numerical Computation of Turbulent Flows," *Comput. Methods Appl. Mech. Eng.*, Vol. 3, pp. 269-289.

129. Durbin, P.A., 1995, "Separated Flow Computations with k-$\epsilon - v^2$ Model," *AIAA Journal*, Vol. 33(4), pp. 659-664.

130. Parneix, S., Durbin, P.A., and Behnia, M., 1998, "Computation of a 3D Turbulent Boundary Layer Using the V2F Model," *Flow Turbulence and Combustion*, Vol. 10, pp. 19-46.

131. Behnia, M., Parneix, S., Shabany, Y., and Behnia, M., 1999, "Numerical Study of Turbulent Heat Transfer in Confined and Unconfined Impingings Jets," *Inter. J. of Heat and Fluid Flow*, Vol. 20, pp. 1-9.

132. Powell, M.J.D., 1992, "The Theory of Radial Basis Function Approximation," *Advances in Numerical Analysis*, Vol. II, Light, W. (ed.), Oxford Science Publications.

133. Jichun Li and Chen, C.S., 2001, "A Simple Efficient Algorithm for Interpolation Between Different Grids in Both 2D and 3D," *Mathematics and Computers in Simulation*, Vol. 58(2), pp. 125-132.

134. Hansen, P.C., 1992, "Analysis of Discrete Ill-posed Problems by Means of the L-Curve," *SIAM Rev.*, Vol 34, pp. 561-580.

135. Hansen, P.C, and O'leary, D.P., 1993, "The Use of the *L*-Curve in the Regularization of Discrete Ill-posed Problems," *SIAM J. Sci. Comput.*, Vol. 14, pp. 1487-1503.

136. Morozov, V.A., 1984, *Methods for Solving Incorrectly Posed Problems*, Springer Verlag.

137. Morozov, V.A., 1992, *Regularization Methods for Ill-Posed Problems*, CRC Press.

138. Goldberg, D.E., 1989, *Genetic Algorithms in Search*, Optimization and Machine Learning, Addison-Wesley, Reading, MA.

139. Brebbia, C.A., and Dominguez, J., 1992, *Boundary Elements: An Introductory Course*, McGraw-Hill Incorporated, New York.

140. Divo, E.A., and Kassab, A.J., 2003, *Boundary Element Method for Anisotropic Hetrogeneous Heat Conduction*, Wessex Institute of Technology (WIT) Press, Southampton, UK, and Boston, USA.

141. Kassab, A.J. and Wrobel, L.C., 2000, *Boundary Element Methods in Heat Conduction*, Chapter 5 in Recent Advances in Numerical Heat Transfer, W.J. Mincowycz and E.M. Sparrow, (eds.), Vol. 2, Taylor and Francis, New York, pp. 143-188.

142. Divo, E. and Kassab, A.J., 2003, *Boundary Element Method for Heat Conduction with Applications in NonHomogeneous Media*, Wessex Institute of Technology (WIT) Press, Southampton, UK, and Boston, USA.

143. Kassab, A.J., Wrobel, L.C., Bialecki, R., and Divo, E., 2004, *Boundary Elements in Heat Transfer*, Chapter 6 in Handbook Of Numerical Heat Transfer, 2nd Edition, Minkowycz, W., Sparrow, E.M., and Murthy, J. Y. (eds.), John Wiley and Sons.

144. Incropera, F.P., and DeWitt, D.P., 2002, *Introduction to Heat Transfer*, 4th edition, John Wiley and Sons, Inc, New York.

145. Kays, W.M., and Crawford, M.E., 1993, *Convective Heat and Mass Transfer*, McGraw-Hill Incorporated, New York.